

Université du Québec
Institut national de la recherche scientifique
Centre Énergie Matériaux Télécommunications

Studies on Resonant High-order Harmonic Generation from Laser-ablated Plume: Some New Perspectives

par
Mangaljit Singh

Thèse présentée pour l'obtention du grade de Philosophiae Doctor (Ph.D.) en
Sciences de l'Énergie et des Matériaux

Jury d'évaluation

Président du jury et examinateur interne

Patrizio Antici
INRS-EMT

Examinateur externe

Joseph Sanderson
Department of Physics & Astronomy
University of Waterloo

Examinateur interne

Michael Zürch
Department of Chemistry
University of California, Berkeley

Directeur de recherche

Tsuneyuki Ozaki
INRS-EMT

Acknowledgements

I present humble gratitude to my research supervisor, Professor Tsuneyuki Ozaki, for supporting me in every phase of my research work, as well as for providing me the freedom to work independently on the choice of my subject. I thank the current director of **ALLS** (Advanced Laser Light Source) laboratory, Professor François Légaré, for welcoming me to the ALLS lab. I would also like to appreciate all the conceptual and technical help I got from the former post-doc Muhammad Ashiq Fareed, which really helped me quickly acquire all the skills needed to successfully perform my experiments in the lab. I would also like to present my gratitude to the thesis jury, composed of Professor Joseph Sanderson, Professor Michael Zürch, and Professor Patrizio Antici, for agreeing to evaluate this work. A big thanks also goes to the entire scientific and technical team of the ALLS laboratory for providing me with technical support during the long weeks of experiments. In particular, I would like to thank Antoine Laramée and Philippe Lassonde, who, through their great knowledge on the techniques of femtosecond laser systems, taught me a lot, and strongly contributed to the realization of the experiments. I would also like to take this opportunity to acknowledge the contributions of our collaborator, Professor Vasily Strelkov from Prokhorov General Physics Institute of the Russian Academy of Sciences, for his continuous inputs, and for providing all the theoretical analysis that led to the better understanding of the underlying phenomena in my experiments. Finally, I am grateful to my friends and family, who gave me the moral support essential for the completion of this work.

Table of Contents

<i>Acknowledgements</i>	<i>iii</i>
<i>Résumé</i>	<i>ix</i>
<i>Abstract</i>	<i>xiii</i>
<i>Abbreviations</i>	<i>xvii</i>
<i>Chapter 1 Introduction</i>	<i>1</i>
1.1 Motivation	1
1.2 HHG from LAP	2
1.3 Laser-ablated Plume.....	3
1.4 HHG Mechanism	4
1.4.a Three-step Model	6
1.4.b Four-step Model.....	8
1.5 References.....	9
<i>Chapter 2 Laser Source and High-order Harmonic Generation Setup</i>	<i>11</i>
2.1 Advance Laser light Source laboratory.....	11
2.1.a Chirped Pulse Amplification.....	11
2.1.b Ti:sapphire Laser Source	11
2.1.c Optical Parametric Amplifier Laser Source	12
2.2 Hollow-core Fiber Setup for Few-cycle Laser Pulses	14
2.3 HHG Setup.....	14
2.4 Laser-ablation Optimization	16
2.5 References.....	17
<i>Chapter 3 Resonant High-order Harmonic Generation in Multiphoton-Ionization Regime</i> ... <i>19</i>	<i>19</i>
3.1 Introduction	19
3.2 Experimental Results	21
3.2.a RH Generation with Near-Infrared Laser Wavelengths from Ga ⁺	21
3.2.b HHG at Higher Keldysh Parameter	22
3.2.c HHG Intensity Comparison from Different LAPs	23
3.3 Coherence	24
3.4 RH Generation Mechanism in the MPI Regime	25
3.5 Calculations of Resonance Transition Parameters.....	25
3.5.a Line Identification	25
3.5.b Spectroscopic Characteristics of the AIS	26
3.6 Calculation of the RH Generation.....	27
3.7 Spatial Distribution of the Electron Wave-packet in the TI and MPI Regime	29
3.8 Summary of the Chapter	30
3.9 References.....	31

Chapter 4 Intense Below-threshold Resonant-harmonic Generation from Laser-ablated Plume	33
4.1 Introduction.....	33
4.2 HHG from In ⁺ with Two-color 800+400 nm Laser Wavelength.....	34
4.3 HHG from In ⁺ with Tunable Mid-infrared Laser Wavelengths.....	35
4.4 HHG from In ⁺ with Tunable Near-infrared Laser Wavelengths	35
4.5 HHG from Ga ⁺ , Sn ⁺ and Cr ⁺ with Tunable Near-infrared Laser Wavelengths	39
4.6 Proposed Coupling Scheme of In ⁺	40
4.7 TDSE Calculations with a Model Two-electron Atom.....	42
4.8 TDSE Calculations with Single-active Electron Model	45
4.9 Energy Levels of In ⁺ and Ga ⁺	47
4.10 Summary of the Chapter	49
4.11 References.....	49
Chapter 5 Resonant High-order Harmonic Generation from Neutral Manganese Atoms	51
5.1 Introduction.....	51
5.2 Resonant Harmonic Generation from Giant Autoionizing Resonance	51
5.3 Significance of Laser Pulse Duration	53
5.4 Experimental Results and Discussion	54
5.5 Numerical Methods.....	57
5.6 Summary of the Chapter	59
5.7 References.....	60
Chapter 6 Resonant High-order Harmonic Generation from Sn III States.....	63
6.1 Introduction.....	63
6.2 HHG from tin LAP using 800 nm Laser Wavelength	64
6.3 Various Sn III Transitions in the Range 26-30 eV	65
6.4 HHG from Tin LAP using Longer 1750 nm and 1780 nm Laser Wavelengths	66
6.5 Energy Level Diagram of Sn II and Sn III.....	68
6.6 Summary of the Chapter	70
6.7 References.....	70
Chapter 7 Conclusions of the Thesis.....	73
Chapter 8 Résumé en Français	75
Publications.....	97

List of figures

Figure 1-1 A typical HHG spectrum.....	2
Figure 1-2 HHG spectra from indium and tin LAP showing RH	3
Figure 1-3 The timescale at which various processes take place during the LAP formation	4
Figure 1-4 Illustration of the MPI and the TI process.....	5
Figure 1-5 The schematic diagram of the three-step model for the HHG mechanism.	8
Figure 1-6 Schematic diagram of the four-step model.....	9
Figure 2-1 Schematic diagram of the concept of Chirped pulse amplification	12
Figure 2-2 The schematic diagram of the laser source in ALLS based on the Ti:sapphire laser oscillator technology.....	13
Figure 2-3 The schematic diagram of the OPA based laser source	13
Figure 2-4 The experimental setup for the generation of intense few-cycle mid-infrared pulses	14
Figure 2-5 Schematic diagram of the experimental setup for the HHG from LAP.	15
Figure 2-6 Schematic diagram of the two-color HHG setup.	16
Figure 2-7 The HHG spectrum generated from graphite LAP accompanied by the incoherent spontaneous emission from various atomic and ionic species	17
Figure 3-1 HHG spectra generated from Ga^+ using 860 nm, 870 nm and 880 nm laser	22
Figure 3-2 HHG spectra generated from Ga^+ using 400 nm and 860 nm laser wavelength.....	23
Figure 3-3 The comparison of RH intensity from Ga^+ with other LAPs known to generate intense harmonics.....	24
Figure 3-4 Fitting curve of calculated PICS to the experimental absorption data	28
Figure 3-5 Calculated spatial distribution of the electron with the energy of the AIS for the MPI and TI regime	29
Figure 4-1 HHG spectrum generated from In^+ with two-color 800+400 nm laser.	35
Figure 4-2 High-order harmonic spectrum generated from In^+ using driving laser pulses centered at 1780 nm, and the change in the 27H intensity when the driving laser wavelength is tuned away from the resonant	36
Figure 4-3 High-order harmonic spectrum generated from In^+ using driving laser pulses with a central wavelength of 860 nm and 940 nm	37

Figure 4-4 The various high-order harmonic spectra generated from In ⁺ using different driving laser wavelengths between 860nm and 940 nm.....	38
Figure 4-5 The high-order harmonic spectrum generated from Ga ⁺ at 800 nm driving laser wavelength, and from Sn ⁺ at 900 nm and 940 nm driving laser wavelength	40
Figure 4-6 The high-order harmonic spectrum generated from Cr ⁺ at 855 nm and 832 nm driving laser wavelength.....	40
Figure 4-7 The proposed coupling scheme of In ⁺ explaining the generation of an intense single-BTH.....	41
Figure 4-8 Calculated 2-photon ionization cross-section and spectra of (a) H9 and H11 in the vicinity 10-photon resonance, (b) H13 and H15 in the vicinity of 14-photon resonance with the even-parity AIS of a model two-electron atom.....	43
Figure 4-9 Calculated 2-photon ionization cross-section and intensities of harmonics H27, H41-45 near the resonances with dressed even-parity AI states in the vicinity of 43-45 eV	44
Figure 4-10 Calculated HHG spectrum from TDSE calculations with a model potential of In ⁺ . 45	
Figure 4-11 The calculated harmonic intensity and the harmonic divergence using the TDSE calculations with a model potential of In ⁺	46
Figure 5-1 Photoabsorption spectra of neutral Mn and Mn ⁺ showing the photoabsorption cross-section	52
Figure 5-2 The ionization yield in hydrogen atom vs peak electric field strength	54
Figure 5-3 Harmonic spectra observed from laser-ablated manganese plume using driving lasers a wavelength of 1.82 μm	55
Figure 5-4 High-order harmonics spectrum with wavelengths 0.8 μm and 1.71 μm	56
Figure 5-5 The high-order harmonic spectrum recorded with a few-cycle driving laser field at 1.8 μm laser wavelength	57
Figure 5-6 Calculated high-order harmonic spectra from manganese with wavelengths 1.71 μm , 1.82 μm and 1.82 μm respectively	59
Figure 6-1 The HHG spectrum generated from tin LAP with 800 nm driving laser wavelength	65
Figure 6-2 HHG spectrum tin LAP using 1780 nm and 1750 nm driving laser wavelength.....	66
Figure 6-3 The expanded view of the HHG spectra generated from tin LAP in the energy range between 24 eV and 33 eV using 1780 nm and 1750 nm driving laser wavelength..	67
Figure 6-4 Energy level diagram of Sn II and Sn III	69

Résumé

La génération d'harmoniques d'ordre élevé (HHG) est un processus non linéaire qui se produit lorsqu'une impulsion laser ultracourte à de haute intensité, généralement d'une durée de femtoseconde (fs), interagit avec un milieu non linéaire. Un spectre du HHG présente une large bande contenant de multiples ordres harmoniques avec des énergies de photons qui sont des multiples impairs de l'énergie photonique du laser. Le HHG constitue d'une source cohérente d'impulsions dans l'ultraviolette extrême (XUV) avec une durée d'impulsion de temporelle de fs et d'attosecondes. HHG permet une méthode puissante pour étudier la dynamique électronique et structurelle des atomes et des molécules avec une résolution temporelle de fs, notamment la spectroscopie pompe-sonde XUV et les techniques de spectroscopie de photoémission résolues temporelles en temps telles que la spectroscopie de photoémission résolue en angle (ARPES) et la microscopie électronique de photoémission (PEEM). Cependant, la faible efficacité de conversion (CE) de HHG par des gaz nobles largement utilisés est un problème crucial (généralement 10^{-6} - 10^{-7}), générant des harmoniques avec une énergie d'impulsion de l'ordre à du nano-joule. La génération d'harmoniques résonnantes (RH) à partir du HHG par panache créée par l'ablation laser (LAP) est une autre source fournissant un flux de photons XUV élevé est la génération d'harmoniques résonnantes (RH) à partir du LAP, avec un CE élevé de 10^{-4} , générant des RH au niveau μJ avec un taux d'amélioration de l'intensité (ER) élevé par rapport aux harmoniques voisines. Le mécanisme de génération des RH est expliqué par le modèle à quatre-étapes. Selon ce modèle, lorsqu'une impulsion laser ultrarapide interagit avec l'atome ou l'ion ablaté par le laser, un électron subit une ionisation par effet tunnel (TI) à partir de la coquille de valence, puis accélère en s'éloignant de l'atome ou de l'ion parent vers le continuum, ce qui constitue les deux premières étapes. Dans la troisième étape, l'électron dans le continuum est dispersé dans l'état d'auto-ionisation (AIS), qui subit ensuite une désintégration radiative dans l'état fondamental initial pour émettre une RH. Par conséquent, les recherches sur le phénomène RH sont importantes non seulement pour le développement des sources de XUV cohérent intense à l'échelle d'un laboratoire (table-top sources), mais ces études ont également la possibilité d'étendre notre compréhension de la dynamique de l'AIS à l'échelle de temps fs.

Dans le cadre de la thèse, nous avons utilisé plusieurs cibles solides (gallium, étain, indium, manganèse, *etc.*) afin d'explorer davantage le phénomène de génération de RH à partir de LAP.

Dans un premier temps, nous avons étudié la génération de RH dans le régime d'ionisation multiphotonique (MPI) précédemment inexploré, où l'ionisation de l'électron de la couche de valence a lieu par l'absorption multiphotonique directe du laser. Ceci est en contraste avec toutes les expériences précédentes générant du RH, où l'électron de la coquille de valence subit une ionisation par le phénomène de tunnel. En utilisant le LAP obtenu à partir d'une cible solide de Gallium, nous observons que dans le régime MPI, des RH intenses peuvent être obtenues avec un ER plus élevé. On constate que cette augmentation de l'ER peut être attribuée à la faible diffusion du paquet d'onde de l'électron dans le régime MPI. Nos recherches dans le régime MPI révèlent une nouvelle méthode pour augmenter l'intensité et le ER d'une lumière XUV intense avec une énergie multi- μ J de durée de fs, ce qui ouvre la voie à la compréhension de l'implication des résonances auto-ionisantes dans la génération de RH dans le régime MPI.

Nous poursuivons nos recherches sur le phénomène RH en étudiant la réponse d'ordre harmonique juste en dessous du seuil d'ionisation (I_p) d'une série de cibles solides, notamment l'indium, le gallium, l'étain et le chrome. Nos études démontrent une nouvelle méthode pour générer une harmonique RH intense à une énergie juste en dessous de I_p dans In^+ et Ga^+ . Cependant, nous n'avons pas observé une telle RH dans Sn^+ et Cr^+ . Il s'avère que cette RH est observée en raison du chevauchement de l'AIS habillé avec le nuage de Rydberg. Cette condition n'est satisfaite que dans In^+ et Ga^+ , mais pas dans Sn^+ et Cr^+ . Cette nouvelle méthode est utile pour générer une lumière XUV intense et cohérente à partir d'états électroniques qui ne participent généralement pas à l'émission d'harmoniques intenses, tels que les états de Rydberg situés juste en dessous de I_p . Cette méthode fournit également un nouveau mécanisme pour approfondir notre compréhension actuelle du phénomène RH et permettre d'étudier la dynamique de l'AIS à l'échelle de temps fs.

Nous nous concentrons en outre sur l'étude de la réponse de la résonance auto-ionisante géante (GAR) à large bande présente dans le manganèse centrée autour de ~50 eV, peut potentiellement générer une impulsion XUV intense à large bande. Dans toutes les expériences précédentes de HHG avec le manganèse, les harmoniques d'ordre élevé étaient générées par les espèces ioniques. Tant le Mn que le Mn^+ présentent un GAR centré à ~50 eV. Dans nos expériences avec des impulsions laser infrarouge moyen à quelques cycles, nous démontrons que les harmoniques d'ordre supérieur sont principalement générées par des atomes neutres. Nos résultats ouvrent la possibilité de faire progresser la technique d'ablation laser pour étudier la dynamique des atomes neutres. La résonance GAR à large bande dans HHG ouvre la possibilité de générer des

attosecondes intenses à large bande. Nos résultats ouvrent également la possibilité de générer des harmoniques à partir de particules neutres ablatées au laser et d'explorer la dynamique du GAR aux échelles de temps ultrarapides.

Enfin, nous étudions le HHG de l'étain LAP en illuminant par un laser aux longueurs d'onde l'infrarouge proche et moyen. Nous avons observé d'une amélioration multiple RH dans la région XUV dus à l'implication des transitions du Sn III. Les renforcements harmoniques multiples sont observés dans la gamme d'énergie dans laquelle plusieurs transitions fortes de Sn III sont identifiées. Ces résultats témoignent du potentiel de la HHG comme technique pratique pour la spectroscopie à haute harmonique du Sn III doublement chargé.

Mots-clés : lasers ultrarapides; génération d'harmoniques d'ordre élevé; harmoniques résonantes; génération d'ultraviolets extrêmes; panache d'ablation laser; ionisation par effet tunnel; ionisation multiphotonique; harmoniques sous le seuil.

Abstract

High-order harmonic generation (**HHG**) is a highly nonlinear process that takes place when a high-intensity ultrashort laser pulse, typically of femtosecond (**fs**) temporal duration, interacts with a nonlinear media. A typical HHG spectrum is broadband containing multiple harmonic orders with photon energies that are odd multiples of the laser photon energy. HHG provides a table-top coherent source of extreme ultraviolet (**XUV**) pulses with fs and attosecond temporal pulse duration, and is a powerful method to study the electronic and structural dynamics of atoms and molecules with fs temporal resolution, for example with XUV pump-probe spectroscopy and the time-resolved photoemission spectroscopic techniques such as the angle-resolved photoemission spectroscopy (**ARPES**) and photoemission electron microscopy (**PEEM**). However, the low HHG conversion efficiency (**CE**) from the widely used noble gases is a critical issue (typically 10^{-6} - 10^{-7}), generating harmonic energy per pulse at the nJ scale. An alternate nonlinear source for HHG providing high XUV photon flux is resonant harmonic (**RH**) generation from the laser-ablated plume (**LAP**), with a high CE of 10^{-4} , generating μJ -level single RH with a high intensity-enhancement ratio (**ER**) relative to the neighboring harmonics. The mechanism of the RH generation can be explained by the four-step model. According to this model, when an ultrafast laser pulse interacts with the laser-ablated atom or ion, an electron undergoes tunnel-ionization (**TI**) from the valence shell and then accelerates away from the parent atom or ion towards the continuum, constituting the first two steps. In the third step, the electron in the continuum is scattered into the autoionizing state (**AIS**) of an atom or ion embedded in the continuum, which then experiences radiative decay into the initial ground state to emit RH. Therefore, the investigations on the RH phenomenon are important not only for the development of intense tabletop ultrafast sources of coherent XUV, but such studies also have the scope to extend our understanding of the dynamics of AIS at the fs timescale.

In this thesis, we use several solid targets (gallium, tin, indium, manganese etc.) to explore further the RH generation phenomenon from LAP. To begin with, we study the RH generation in the previously unexplored multiphoton-ionization (**MPI**) regime, where the ionization of the valence shell electron takes place due to the direct multiphoton absorption from the driving laser. This is in contrast to all the previous experiments generating RH, where the valence shell electron undergoes ionizing through the tunneling phenomenon. Using LAP obtained from Gallium solid

target, we observe that in the MPI regime, one could obtain an intense RH with a superior ER. It is revealed that this increase in the ER can be attributed to the low electron wave-packet spreading in the MPI regime. Our investigations in the MPI regime reveal a new method to increase the intensity and ER of intense multi- μ J fs XUV light, as well as pave the way towards the understanding of the involvement of autoionizing resonances in generating RH in the MPI regime.

We continue our investigations on the RH phenomenon by studying the response of the harmonic order just below the ionization threshold (I_p) from a range of solid targets, including indium, gallium, tin and chromium. Our studies demonstrate a new method to generate intense RH harmonic at an energy just below the I_p in In^+ and Ga^+ . However, we did not observe such an RH in Sn^+ and Cr^+ . It is revealed that such RH is observed because of the overlap of the dressed-AIS with the Rydberg cloud. This condition is only satisfied in In^+ and Ga^+ , but not in Sn^+ and Cr^+ . This new method is useful to generate bright coherent XUV light from electronic states that usually do not participate in intense harmonic emission, such as Rydberg states located just below the I_p . It also provides a new mechanism to expand our current understanding of the RH phenomenon and study the dynamics of AIS at the fs timescale.

In addition, we focus on investigating the response of broadband giant autoionizing resonance (**GAR**) present in manganese centered at \sim 50 eV, which has the potential to generate broadband intense XUV pulse. In all the previous HHG experiments with manganese, the high-order harmonics were generated from the ionic species. Both Mn as well as Mn^+ exhibit GAR centered at \sim 50 eV. In our experiments with few-cycle mid-infrared laser pulses, we demonstrate that the high-order harmonics are predominantly generated from neutral atoms. Our results open the possibility to advance the laser-ablation technique to study the dynamics of neutral atoms. The broadband GAR resonance in HHG opens the opportunity to generate intense broadband attosecond. Our results also open the possibility to generate harmonics from laser-ablated neutral particles and explore the dynamics of the GAR on ultrafast timescales.

Finally, we study the HHG from tin LAP using near and mid-infrared laser wavelengths. We observed multiple RH enhancements in the XUV region due to the involvement of Sn III transitions. The multiple harmonic enhancements are found to be in the energy range where several strong transitions of Sn III are identified. These results demonstrate the potential of HHG as a convenient technique for high-harmonic spectroscopy of the doubly charged Sn III.

Keywords: ultrafast lasers; high-order harmonic generation; resonant harmonic; extreme ultraviolet generation; laser-ablated plume; tunnel-ionization; multiphoton ionization; below-threshold harmonic.

Abbreviations

- **ARPES:** Angle-resolved photoemission spectroscopy
- **AIS:** Autoionizing state
- **ALLS:** Advanced Laser Light Source
- **BBO:** Beta barium borate
- **BTH:** Below-threshold Harmonic
- **CE:** Conversion Efficiency
- **ER:** Enhancement Ratio
- **FEL:** Free-electron Laser
- **fs:** Femtosecond
- **GAR:** Giant Autoionizing Resonance
- **HF:** Hartree-Fock
- **HHG:** High-order Harmonic Generation
- **LAP:** Laser-ablated Plume
- **MPI:** Multiphoton Ionization
- **OPA:** Optical Parametric Amplifier
- **PEEM:** Photoemission electron microscopy
- **PICS:** Photoionization Cross-Section
- **QM:** Quasi-monochromatic
- **RH:** Resonant Harmonic
- **TDSE:** Time-dependent Schrödinger equation
- **TI:** Tunnel-ionization
- **XUV:** Extreme Ultraviolet

Chapter 1

Introduction

1.1 Motivation

The invention of the laser is considered to be one of the most important scientific breakthroughs of the 20th century. Lasers have unique characteristics, such as spatial and temporal coherence, directionality, monochromaticity and high intensity. Applications of such laser light have resulted in groundbreaking developments in numerous fields, such as medicine, quantum physics and spectroscopy, communication, laser printing and the entertainment industry in the form of CDs-DVDs [2]. More recently, breakthroughs have occurred with the development of pulsed lasers with durations as short as a few fs, resulting in light wave-packets containing only a few oscillations of the electromagnetic field [3]. By focusing such laser pulses, these light fields confined to such short temporal duration can create intensities as high as 10^{15} W cm⁻² using only a mJ of pulse energy. Such high intensities are strong enough to suppress the Coulomb forces that bind atoms and molecules together and hence enable the study of the physics behind the phenomenon of atomic and molecular ionizations. [4] The ultrashort laser pulse durations also enabled researchers to perform temporally resolved studies of the ultrafast dynamics of many atomic and molecular phenomenon. [5]

Due to several limitations imposed by the fundamental physics of lasers, most commercially available lasers operate only in the visible or longer wavelength region of the electromagnetic spectrum. Such limitations include reduced stimulated emission cross-section, a decrease in the lifetime of the energy levels of a given laser active medium and an increased energy level broadening effects at shorter wavelengths [6]. As a result, the population inversion, which is an essential requirement for the laser to operate, decreases rapidly with decreasing laser wavelength λ , scaling as λ^{-4} to λ^{-6} [6]. This results in a drastically inefficient laser system for shorter wavelengths, which has discouraged efforts to commercialize such systems.

Nevertheless, inspiration for the development of sources emitting laser-like radiation in the short wavelength regions, especially in the XUV and soft X-ray radiation, comes from a multitude of potential applications, such as XUV pump-probe spectroscopy [7], intense attosecond pulses [8],

XUV lithography [9], coherent nanoscale imaging [10], time-resolved photoemission spectroscopy [11][12][13] and X-ray microscopy [14][15].

In recent times, HHG from noble gases has proven to be an excellent source of coherent XUV and soft X-ray radiation. HHG is an extremely nonlinear and non-perturbative process that occurs due to ultrahigh intensity laser-matter interaction between a nonlinear medium and a high-intensity ultrafast laser pulse [15]. The HHG process has successfully demonstrated XUV and soft X-ray radiation with excellent coherence and spatial profiles. As shown in Figure 1-1, a typical HHG spectrum generated by a driving laser photon with an energy E_p contains spikes/harmonics with energy $n \times E_p$, where n is an odd integer, called the harmonic order. However, since HHG is a highly nonlinear and non-perturbative process, its CE is extremely low, typically in the range of 10^{-6} to 10^{-8} for various noble gases, generating only nJ values of XUV pulse energies [16]. Such low efficiency results in the limited applicability of such a source for potential applications.

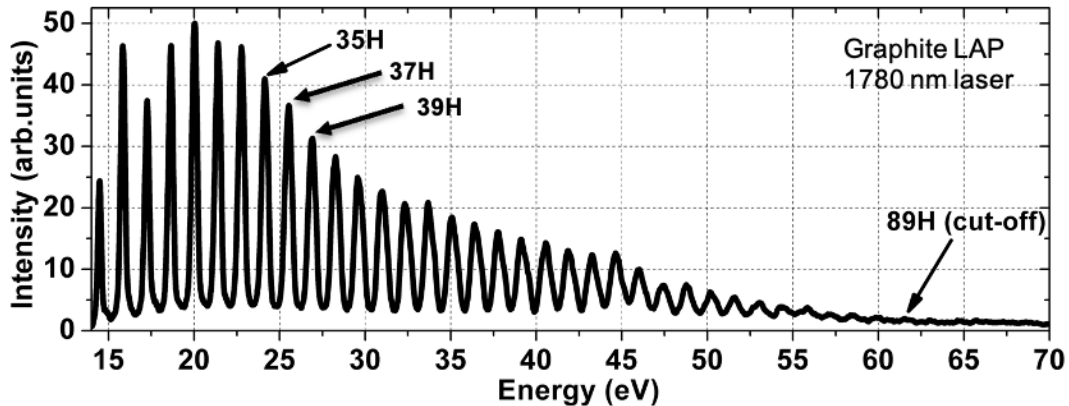


Figure 1-1 A typical HHG spectrum. 35H denotes the 35th harmonic order, *i.e.*, photon energy of $35 \times E_p$. The maximum harmonic order, which in this case is 89H, is called the harmonic cut-off.

1.2 HHG from LAP

HHG from LAP has proven to be an efficient source of coherent XUV and soft X-ray radiation. In many LAPs, it was observed that the intensity of one harmonic order was abnormally larger than the neighboring harmonics [17]. This phenomenon is known as resonant HHG, and the corresponding harmonic is called RH. For example, as shown in Figure 1-2, in indium LAP, the RH is observed at 61.2 nm (19.92 eV), corresponding to 13H with 800 nm driving laser wavelength, with harmonic intensity two orders of magnitude higher than the neighboring harmonics.

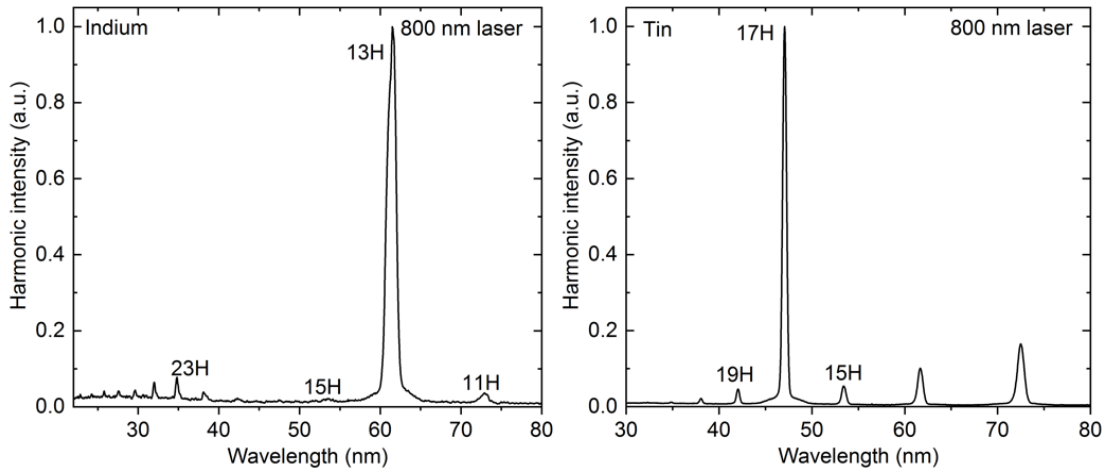


Figure 1-2 HHG spectra from indium and tin LAP showing RH.

A similar enhancement is seen in tin LAP at 47 nm (26.3 eV), which corresponds to 17H with 800 nm driving laser wavelength (see Figure 1-2) [29]. Careful investigations revealed that the singly charged species of both tin as well as indium exhibit a strong electronic transition with a high oscillator strength close to the RH wavelength. For example, the Sn^+ ion possesses a transition $4\text{d}^{10} 5\text{s}^2 5\text{p } ^2\text{P}_{3/2} \rightarrow 4\text{d}^9 5\text{s}^2 5\text{p } (^1\text{D}) ^2\text{D}_{5/2}$ at 26.27 eV (47.2 nm) with a high oscillator strength of 1.52 [18]. Similarly, In^+ ion also possesses a transition $4\text{d}^{10} 5\text{s}^2 ^1\text{S}_0 \rightarrow 4\text{d}^9 5\text{s}^2 5\text{p } (^2\text{D}) ^1\text{P}_{1/2}$ at 19.92 eV (\sim 62.24 nm) with a high oscillator strength of 1.11 [19]. RH of tin and indium are capable of generating bright harmonics having μJ values of harmonic energies [20,21]. Apart from indium and tin, chromium, manganese, and antimony are some of the other materials that also show the phenomenon of RH [17].

1.3 Laser-ablated Plume

In our experiments, to generate the high-order harmonics, we use an LAP as the nonlinear media. To create the LAP, we focus on to a solid target, the laser pulses of 210 picosecond temporal duration with the central wavelength of 800 nm. The choice of the solid target varies depending on the aim of a particular experiment. The LAP formation starts with the absorption of incident laser photons, which is followed by the heating and the photoionization of the solid surface undergoing interaction with the laser pulses. Subsequently, the material ablated due to the thermal vaporization expands in the form of a plasma plume containing neutral, single as well as highly charged states of the atomic species. For example, in the case of a solid manganese target, the

expanding LAP can contain neutral Mn, Mn^+ as well as Mn^{2+} species [22,23]. Figure 1-3 shows the approximate time scale at which various processes are occurring during the laser ablation. The exact timescale will be different for the different choices of the solid target. This is due to the difference in the atomic weights of different materials, and hence the LAP formed from different materials needs a different timescale (typically a few tens of nanoseconds) for the plume expansion. Therefore, in the HHG experiments from LAPs, it is important to optimize the timing between the picosecond pre-pulse forming the LAP, and the fs main-pulse generating the high-order harmonics. The details of the experimental setup are given in Chapter 2 of this thesis.

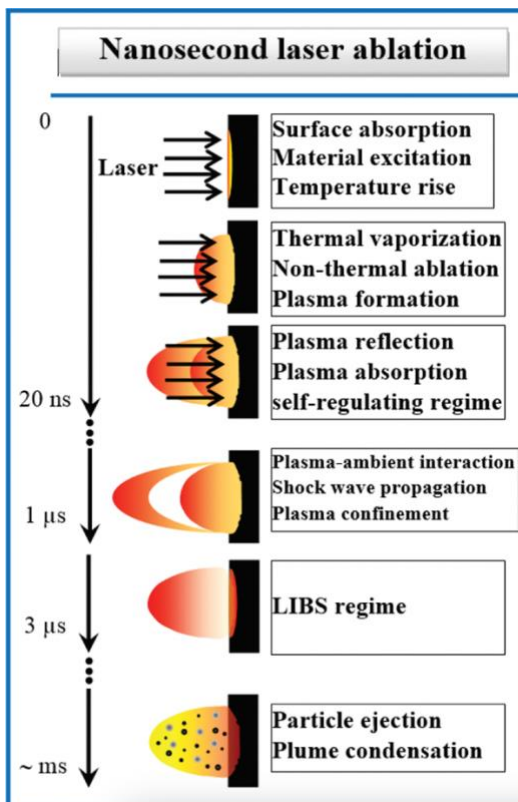


Figure 1-3 The approximate timescale at which various processes take place during the LAP formation by the picosecond laser pulses. Image courtesy: Intechopen (<https://www.intechopen.com/chapters/50866>, link accessed on Nov 25, 2021)

1.4 HHG Mechanism

The basic generation mechanism of the HHG can be explained by considering the semi-classical motion of the valence shell electron of an atom or ion under the influence of the field of an intense ultrashort laser pulse. For an electron interacting with the laser electric field strength E_o and having

the laser frequency ω_o , the quiver energy, also known as the ponderomotive energy, which is defined as the cycle average kinetic energy of the electron, is given by:

$$U_p = \frac{e^2 E_o^2}{4m_e \omega_o^2}$$

where e is the electronic charge and m_e is the mass of the electron. Substituting all the constant values, the expression for U_p can be simplified to

$$U_p = 9.34 I \lambda^2$$

where I is the laser intensity in units of 10^{14} W/cm^2 , and λ is the laser wavelength in μm , providing U_p in eV.

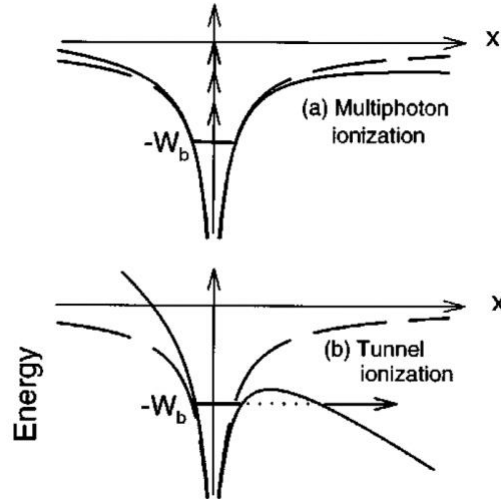


Figure 1-4 Illustration of the MPI and the TI process. W_b represents the suppressed binding potential [24].

The ponderomotive energy is a crucial parameter in determining the nature of the HHG mechanism responsible at the given laser parameters. For example, as will be explained in the following sections, the ionization of the valence shell electron is an important event in the HHG mechanism. However, the nature/mechanism of the ionization process can be different at different laser parameters. For example, the laser field can be sufficiently intense to suppress the Coulomb barrier holding the valence shell electron, and the ponderomotive energy gained by the electron can be sufficient to allow the electron to escape the potential barrier. This kind of ionization is known as TI. On the other hand, if the ponderomotive energy is not sufficient, the electron can alternatively escape the potential barrier by direct MPI, *i.e.*, by absorbing multiple laser photons simultaneously

to gain enough energy to escape the potential barrier. See Figure 1-4 for the illustration of these two processes.

The important parameter that can be used to identify what process will be dominating at given laser parameters is known as the Keldysh parameter [24,25], which is defined as:

$$\gamma = \sqrt{I_p/2U_p} = 0.231 \sqrt{I_p/I\lambda^2}$$

where I_p is in eV, I is the laser intensity in units of 10^{14} W/cm 2 , λ is the laser wavelength in μm , and U_p is the ponderomotive energy in eV). The MPI process will be dominating if $\gamma > 1$, while the TI process will be dominating for $\gamma < 1$.

1.4.a Three-step Model

Most HHG experiments performed using fs Ti:sapphire and mid-infrared laser pulses satisfy the conditions for the TI regime, *i.e.*, with the Keldysh parameter $\gamma < 1$. Hence, the TI process is the dominating ionization process. In such a case, the HHG mechanism can be explained by the semi-classical three-step model [26]. In this model, the first step is the TI of the valence shell electron or ion participating in the HHG process. The motion of the tunnel-ionized electron is considered to be influenced only by the driving laser electric field without any influence of the Coulomb interaction from the parent ion. The electric field of the driving laser field of the frequency ω_o and the peak electric field E_o can be written as:

$$E(t) = E_o \cos(\omega_o t)$$

In the second step of the three-step model, the tunnel-ionized electron gets accelerated toward the continuum under the driving laser field. The influence of the driving laser field $E(t)$ on the tunnel-ionized electron can be represented by the equation of motion:

$$\frac{d^2x(t)}{dt^2} = \frac{-e}{m_e} E(t) = \frac{-e}{m_e} E_o \cos(\omega_o t)$$

where $x(t)$ is the location of the electron at time t , e is the electronic charge, and m_e is the mass of the electron. The parameter $\frac{d^2x(t)}{dt^2}$ represents the instantaneous acceleration of the electron. The instantaneous velocity of the electron ionized at the time t' can be obtained by integrating the above equation.

$$v(t) = \int_{t_i}^t \frac{-e}{m_e} E(t) dt = \frac{-eE_o}{m_e} \int_{t'}^t \cos(\omega_o t) dt$$

$$= \frac{-eE_o}{m_e\omega_o} [\sin(\omega_o t) - \sin(\omega_o t')]$$

Integrating the above equation provides the expression for the instantaneous location $x(t)$ of the electron.

$$\begin{aligned} x(t) &= \frac{-eE_o}{m_e\omega_o} \int_{t'}^t [\sin(\omega_o t) - \sin(\omega_o t')] dt \\ &= \frac{eE_o}{m_e\omega_o^2} \{[\cos(\omega_o t) - \cos(\omega_o t')] + \omega_o \sin(\omega_o t') (t - t')\} \end{aligned}$$

Defining the parameter $X_o = 2eE_o/m_e\omega_o^2$, the above equation becomes:

$$x(t) = \frac{X_o}{2} \{[\cos(\omega_o t) - \cos(\omega_o t')] + \omega_o \sin(\omega_o t') (t - t')\}$$

In the third step, when the driving laser field reverses its direction, the tunnel-ionized electron can return back to the parent ion to recombine into the initial ground state to emit the high-order harmonics. Both at the time of TI and at the time of recombination, the parameter $x(t)$ is zero. From the above equation, an electron tunnel-ionized at the peak of the electric field $E(t) = E_o \cos(\omega_o t)$ i.e., at $\omega_o t' = 0$ will result in the electron returning to the parent ion at $\omega_o t' = 2\pi$. This implies that the electron returns back exactly after one laser cycle.

$$x(t) = \frac{X_o}{2} \{[\cos(2\pi) - \cos 0] + \omega_o \sin(0) \left(\frac{2\pi}{\omega_o} - 0 \right)\} = 0$$

For the electron tunnel-ionized at $t'=0$, the electron distance $x(t)$ will be maximum at half-cycle, i.e., at $\omega_o t = \pm\pi$, with the maximum value of $\pm X_o$.

Upon recombination of the electron into the ground state, the photon energy emitted by the atom or ion will be the sum of the I_p and the electron kinetic energy at the time of recombination.

$$\begin{aligned} \hbar\Omega &= I_p + \frac{1}{2} m_e v^2(t) \\ &= I_p + 2U_p [\sin(\omega_o t) - \sin(\omega_o t')]^2 \end{aligned}$$

It is important to note that for the electron ionized at $\omega_o t' = 0$ and recombining one cycle later at time $\omega_o t = 2\pi$, the kinetic energy of the electron at the recombination will be zero, and hence emitting photon energy equal to I_p . Another significant point to be noted is that not every electron ionized by the laser field at different ionization times will return to the initial location for the recombination. It can be shown that only the electron ionization between $0 < \omega_o t' < \pi/2$ can return to the initial location for the recombination, while the electron ionized between

$\pi/2 < \omega_0 t' < \pi$ will not return, and hence will escape the parent ion. Similarly, because of the symmetry associated with the oscillating driving laser field, the electron ionized between $\pi < \omega_0 t' < 3\pi/2$ can return to the initial location, while the electron ionized between $3\pi/2 < \omega_0 t' < 2\pi$ will not return. It can be shown that the maximum kinetic energy at the recombination time is achieved for $\omega_0 t' = 0.05 \times 2\pi$ and $\omega_0 t = 0.7 \times 2\pi$, providing the maximum photon energy $\hbar\Omega_{max}$ emitted during the HHG, which is also known as the harmonic cut-off.

$$\hbar\Omega_{max} = I_p + 3.17U_p$$

$$\hbar\Omega_{max}[eV] = I_p[eV] + 29.61 \times I_L[10^{14} W/cm^2] \lambda^2[\mu m]$$

To summarize, the semi-classical three-step model constitutes three steps involving the TI of the valence electron, its acceleration within the continuum, followed by a radiative recombination into the initial ground state emitting the XUV. The schematic diagram depicting the three-step model is shown in Figure 1-5.

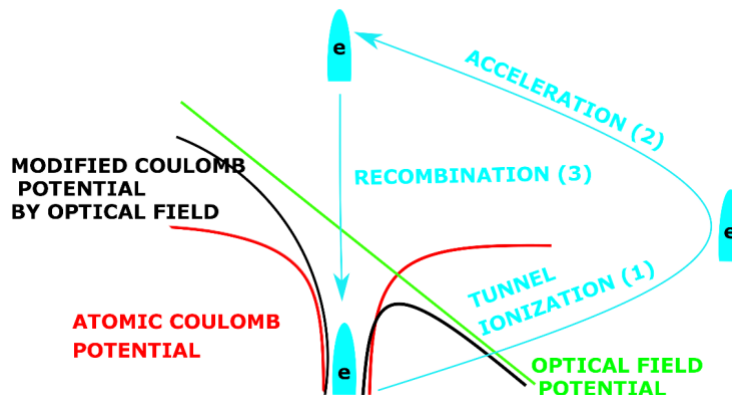


Figure 1-5 The schematic diagram of the three-step model for the HHG mechanism.

1.4.b Four-step Model

As explained in the previous sections, in many LAPs, the intensity of a single harmonic order is seen to be more than an order of magnitude higher as compared to the neighboring harmonics. The three-step model cannot explain this phenomenon because it does not consider the influence of any electronic states that might perturb the motion of tunnel-ionized electrons when accelerating under the influence of the laser electric field. When the energy of a suitable radiative transition with high oscillator strength matches with the harmonic order at a given laser wavelength, the RH

generation takes place with intensity enhancement relative to the neighboring harmonics. For example, as already explained, the Sn^+ ions show RH at 26.3 eV due to the high oscillator strength transition $4\text{d}^{10} \ 5\text{s}^2 \ 5\text{p} \ ^2\text{P}_{3/2} \rightarrow 4\text{d}^9 \ 5\text{s}^2 \ 5\text{p}^2 \ (^1\text{D}) \ ^2\text{D}_{5/2}$ [20]. Similarly, the In^+ also show RH generation at 19.92 eV due to the transition $4\text{d}^{10} \ 5\text{s}^2 \ ^1\text{S}_0 \rightarrow 4\text{d}^9 \ 5\text{s}^2 \ 5\text{p} \ (^2\text{D}) \ ^1\text{P}_{1/2}$ [27]. To explain the RH phenomenon in LAPs, the four-step model was introduced. In this model, the first two steps are the same as the three-step model, *i.e.*, TI of the valence electron and its acceleration within the continuum [28]. The third step, however, involves resonant capture of the tunnel-ionized electron into the AIS, *i.e.*, a discrete state embedded in the continuum, which is followed by the fourth step involving a radiative transition from AIS to the initial ground state emitting RH [28][29][30].

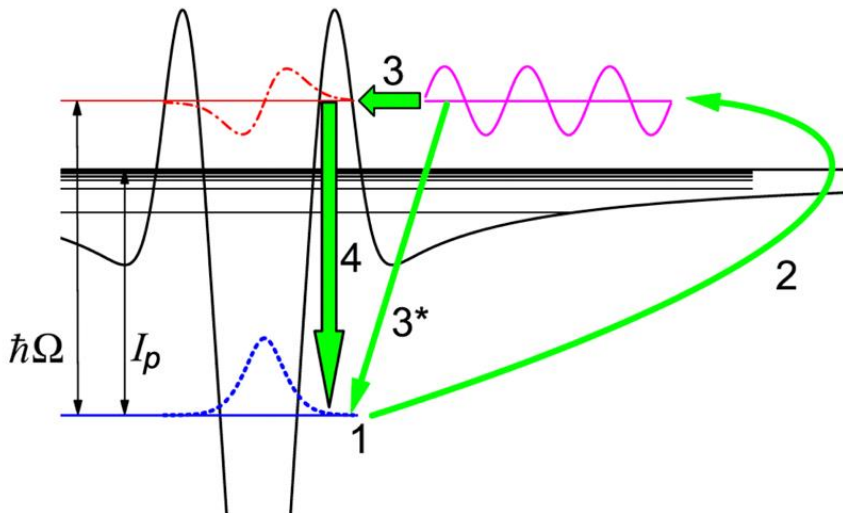


Figure 1-6 Schematic diagram of the four-step model. The label ‘1’ and ‘2’ represents the tunnel-ionization of the valence shell electron and it’s the acceleration within the continuum, respectively. The label ‘ 3^* ’ represents the direct recombination of the electron from the continuum into the ground state, *i.e.*, the final step of the three-step model. However, the label ‘3’ represents the resonant capture of the tunnel-ionized electron into the AIS, and the label ‘4’ represents radiative transition from AIS to the initial ground state emitting RH of frequency Ω [28].

1.5 References

1. G. Mourou, "Nobel Lecture: Extreme light physics and application," *Reviews of Modern Physics* **91**, 030501 (2019).
2. T. Brabec and F. Krausz, "Intense few-cycle laser fields: Frontiers of nonlinear optics," *Reviews of Modern Physics* **72**, 545–591 (2000).
3. M. Lewenstein and A. L’Huillier, "Principles of Single Atom Physics: High-Order Harmonic Generation, Above-Threshold Ionization and Non-Sequential Ionization," in (Springer, New York, NY, 2008), pp. 147–183.
4. H. Ibrahim, B. Wales, S. Beaulieu, B. E. Schmidt, N. Thiré, E. P. Fowe, É. Bisson, C. T. Hebeisen, V. Wanie, M. Giguére, J.-C. Kieffer, M. Spanner, A. D. Bandrauk, J. Sanderson, M. S. Schuurman, and F. Légaré, "Tabletop imaging

- of structural evolutions in chemical reactions demonstrated for the acetylene cation," *Nature Communications* **5**, 4422 (2014).
5. H. C. Kapteyn, L. B. Da Silva, and R. W. Falcone, "Short-wavelength lasers," *Proceedings of the IEEE* **80**, 342–347 (1992).
 6. F. Kelkensberg, C. Lefebvre, W. Siu, O. Ghafur, T. T. Nguyen-Dang, O. Atabek, A. Keller, V. Serov, P. Johnsson, M. Swoboda, T. Remetter, A. L'Huillier, S. Zherebtsov, G. Sansone, E. Benedetti, F. Ferrari, M. Nisoli, F. Lépine, M. F. Kling, and M. J. J. Vrakking, "Molecular Dissociative Ionization and Wave-Packet Dynamics Studied Using Two-Color XUV and IR Pump-Probe Spectroscopy," *Physical Review Letters* **103**, 123005 (2009).
 7. E. Goulielmakis, V. S. Yakovlev, A. L. Cavalieri, M. Uiberacker, V. Pervak, A. Apolonski, R. Kienberger, U. Kleineberg, and F. Krausz, "Attosecond Control and Measurement: Lightwave Electronics," *Science* **317**, (2007).
 8. L. R. Hughey, R. T. Williams, J. C. Rife, D. J. Nagel, and M. C. Peckerar, "Instrumentation for XUV lithography at SURF-II," *Nuclear Instruments and Methods in Physics Research* **195**, 267–271 (1982).
 9. J. Rothhardt, G. K. Tadesse, W. Eschen, and J. Limpert, "Table-top nanoscale coherent imaging with XUV light," *Journal of Optics* **20**, 113001 (2018).
 10. A. Damascelli, "Probing the Electronic Structure of Complex Systems by ARPES," *Physica Scripta* **T109**, 61 (2004).
 11. Y. He, I. M. Vishik, M. Yi, S. Yang, Z. Liu, J. J. Lee, S. Chen, S. N. Rebec, D. Leuenberger, A. Zong, C. M. Jefferson, R. G. Moore, P. S. Kirchmann, A. J. Merriam, and Z.-X. Shen, "Invited Article: High resolution angle resolved photoemission with tabletop 11 eV laser," *Review of Scientific Instruments* **87**, 011301 (2016).
 12. O. Schmidt, M. Bauer, C. Wiemann, R. Porath, M. Scharte, O. Andreyev, G. Schönhense, and M. Aeschlimann, "Time-resolved two photon photoemission electron microscopy," *Applied Physics B* **74**, 223–227 (2002).
 13. J. Miao, T. Ishikawa, B. Johnson, E. H. Anderson, B. Lai, and K. O. Hodgson, "High Resolution 3D X-Ray Diffraction Microscopy," *Physical Review Letters* **89**, 088303 (2002).
 14. P. Thibault, M. Dierolf, A. Menzel, O. Bunk, C. David, and F. Pfeiffer, "High-resolution scanning x-ray diffraction microscopy..," *Science* **321**, 379–82 (2008).
 15. C. Winterfeldt, C. Spielmann, and G. Gerber, "Colloquium : Optimal control of high-harmonic generation," *Reviews of Modern Physics* **80**, 117–140 (2008).
 16. M. Schnürer, Z. Cheng, M. Hentschel, G. Tempea, P. Kálmán, T. Brabec, and F. Krausz, "Absorption-Limited Generation of Coherent Ultrashort Soft-X-Ray Pulses," *Physical Review Letters* **83**, 722–725 (1999).
 17. R. A. Ganeev, "High-order harmonic generation in a laser plasma: a review of recent achievements," *Journal of Physics B* **40**, R213 (2007).
 18. G. Duffy, P. van Kampen, and P. Dunne, "4d→5p transitions in the extreme ultraviolet photoabsorption spectra of Sn II and Sn III," *Journal of Physics B* **34**, 3171–3178 (2001).
 19. G. Duffy and P. Dunne, "The photoabsorption spectrum of an indium laser produced plasma," *Journal of Physics B* **34**, L173–L178 (2001).
 20. M. Suzuki, M. Baba, R. Ganeev, H. Kuroda, and T. Ozaki, "Anomalous enhancement of a single high-order harmonic by using a laser-ablation tin plume at 47 nm," *Optics Letters* **31**, 3306 (2006).
 21. R. A. Ganeev, M. Suzuki, M. Baba, H. Kuroda, and T. Ozaki, "Strong resonance enhancement of a single harmonic generated in the extreme ultraviolet range," *Optics Letters* **31**, 1699 (2006).
 22. R. A. Ganeev, L. B. E. Bom, J.-C. Kieffer, M. Suzuki, H. Kuroda, and T. Ozaki, "Demonstration of the 101st harmonic generated from a laser-produced manganese plasma," *Physical Review A* **76**, 023831 (2007).
 23. M. A. Fareed, V. V. Strelkov, M. Singh, N. Thiré, S. Mondal, B. E. Schmidt, F. Légaré, and T. Ozaki, "Harmonic Generation from Neutral Manganese Atoms in the Vicinity of the Giant Autoionization Resonance," *Physical Review Letters* **121**, 023201 (2018).
 24. S. v Popruzhenko, "Keldysh theory of strong field ionization: History, applications, difficulties and perspectives," *Journal of Physics B* **47**, 204001 (2014).
 25. L.V. Keldysh, "Ionization in the Field of a Strong Electromagnetic Wave," *Sov. Phys. JETP* **20**, 1307 (1965).
 26. P. Corkum, "Plasma perspective on strong field multiphoton ionization," *Physical Review Letters* **71**, 1994–1997 (1993).
 27. R. A. Ganeev, M. Suzuki, M. Baba, H. Kuroda, and T. Ozaki, "Strong resonance enhancement of a single harmonic generated in the extreme ultraviolet range," *Optics Letters* **31**, 1699 (2006).
 28. V. Strelkov, "Role of Autoionizing State in Resonant High-Order Harmonic Generation and Attosecond Pulse Production," *Physical Review Letters* **104**, 123901 (2010).
 29. V. V. Strelkov, M. A. Khokhlova, and N. Y. Shubin, "High-order harmonic generation and Fano resonances," *Physical Review A* **89**, (2014).
 30. M. A. Fareed, V. V. Strelkov, N. Thiré, S. Mondal, B. E. Schmidt, F. Légaré, and T. Ozaki, "High-order harmonic generation from the dressed autoionizing states," *Nature Communications* **8**, 16061 (2017).

Chapter 2

Laser Source and High-order Harmonic Generation Setup

2.1 Advance Laser light Source laboratory

All the experiments reported in this thesis were performed in the ALLS laboratory, which is a unique user facility located at the Varennes campus of the INRS-EMT. This laser laboratory provides a range of laser wavelengths with ultrafast pulse duration going down to a few fs. In the ALLS laboratory, there are laser sources based on Ti:sapphire laser oscillator emitting 4 nJ, 20 fs temporal duration, 75 MHz pulse repetition rate with a central laser wavelength at 795 nm. The pulse repetition rate is reduced to 10 Hz, 100 Hz and 1 kHz depending upon the requirements, and hence the different laser lines for different users. Subsequently, the laser output is amplified through various amplification stages using the chirped pulse amplification technology. The amplified output of this oscillator at 100 Hz is also fed to a laser source based on the optical parametric laser technology, providing tunable laser wavelengths in the range from 1600-2200 nm.

2.1.a Chirped Pulse Amplification

The 4nJ pulse energy of the Ti:sapphire output needs to be amplified before it can be used for the HHG experiments. The schematic diagram showing the concept of chirped pulse amplification process is shown in Figure 2-1 [1]. The fs ultrashort seed pulse that needs to be amplified is first stretched by introducing a temporal chirp using an optical stretcher, which typically constitutes a pair of gratings, as shown in Figure 2-1. The pulse stretcher introduces a positive dispersion, *i.e.*, the long wavelengths (red in this case) cover a shorter path, and hence travel ahead of the shorter wavelengths after exiting the stretcher. The stretched seed pulse, which typically has a pulse duration of a few hundred picoseconds, is sent through a multipass optical amplifier. The amplified picosecond laser pulse is later compressed down to the fs timescale using a grating-based pulse compressor. The compressor introduces the negative dispersion into the amplified stretched laser pulse, *i.e.*, the shorter wavelengths (blue in this case) cover a shorter path than the longer wavelengths, and hence can compensate the positive dispersion carried by the stretched laser pulse.

2.1.b Ti:sapphire Laser Source

The schematic diagram of the laser source based on the Ti:sapphire laser oscillator is shown in Figure 2-2. The mode-locked Ti:sapphire oscillator pumped with a 532 nm continuous wave pump

laser generates laser pulses of 4 nJ pulse energy at 75 MHz pulse repetition rate, with the central laser wavelength of 795 nm. The pulse repetition rate is subsequently reduced, and the laser pulses are amplified using the chirped pulse amplification technology. To achieve this, the stretched laser pulses with a pulse duration of ~200 psec are amplified in two stages of optical amplification. After the laser pulse compression with a dual grating pulse compressor, pulse energies as high as 200 mJ can be obtained. This amplified laser output is split into two user lines, one providing laser pulse energies up to 50 mJ (called the low-energy line) and the other laser line providing pulse energies as high as 150 mJ (called the high-energy line). For our HHG experiments requiring 10 Hz or 100 Hz repetition rate, we used the low-energy line, and the laser pulse energy was further reduced, as per requirements, to the values between 1-10 mJ by using a combination of a half-wave plate and a linear polarizer (not shown in the Figure).

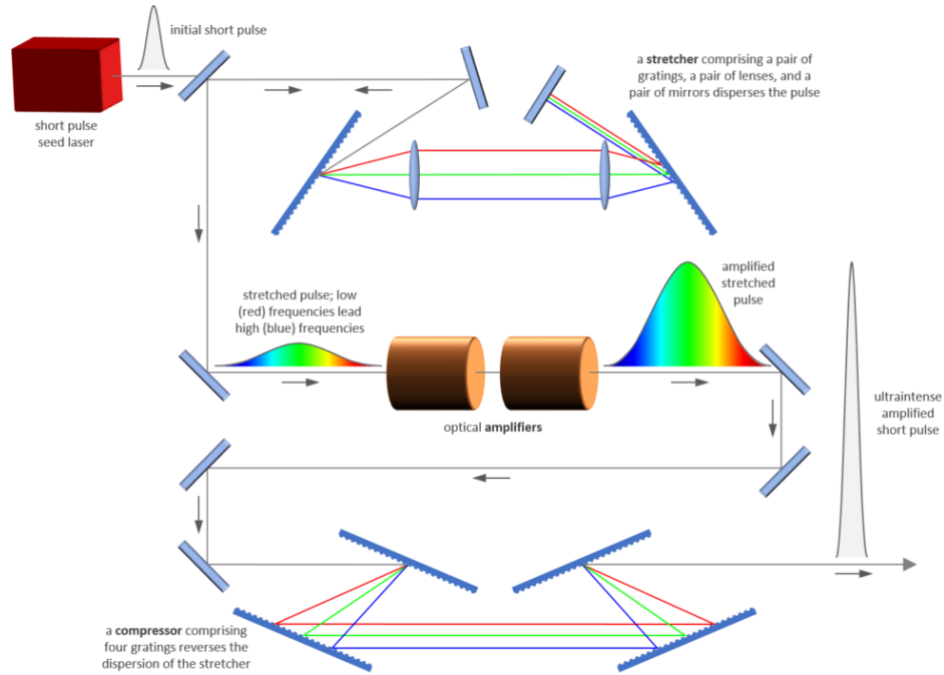


Figure 2-1 Schematic diagram of the concept of Chirped pulse amplification [1].
Image Courtesy: Plymouth Grating Laboratory Inc., Massachusetts (U.S.A)

2.1.c Optical Parametric Amplifier Laser Source

The optical parametric amplifier (**OPA**, TOPAS-800) laser source installed at ALLS provides tunable mid-infrared laser wavelengths (in the range 1600-2200 nm) at a 100 Hz pulse repetition rate. The compressed amplified output of the Ti:sapphire laser source is used to pump the OPA for the frequency conversion. The OPA laser source is based on the nonlinear process of spontaneous

parametric down-conversion in the sapphire crystal, where a laser pump photon is split into one signal and one idler photon, satisfying the energy and momentum conservation as follows:

$$\omega_p = \omega_i + \omega_s \text{ (Energy conservation)}$$

$$\bar{k}_p = \bar{k}_i + \bar{k}_s \text{ (Momentum conservation)}$$

Here, the subscript i denotes the idler, s denotes the signal photon and \bar{k} denotes the wave vector. For example, the 800 nm pump laser photon can be split into one 1440 nm signal photon and one 1800 nm idler photon (as per the energy conservation).

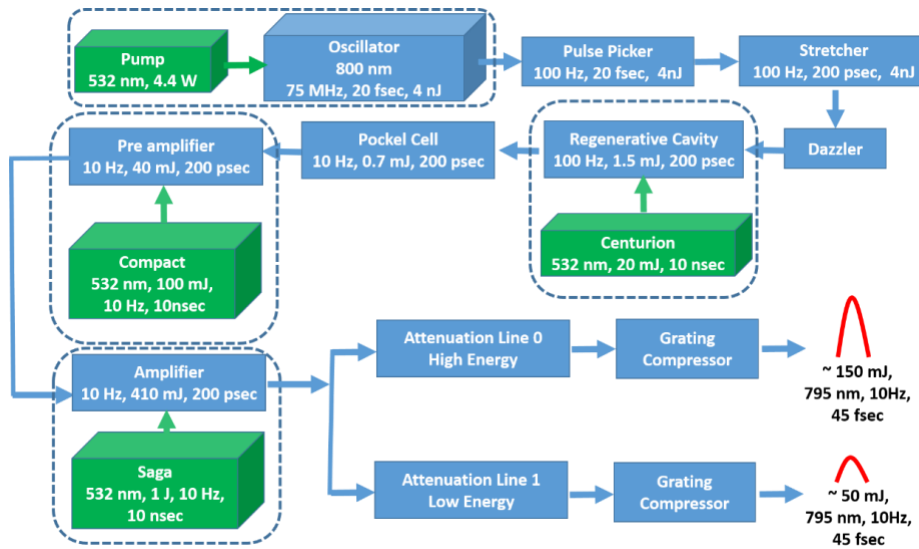


Figure 2-2 The schematic diagram of the laser source in ALLS based on the Ti:sapphire laser oscillator technology.

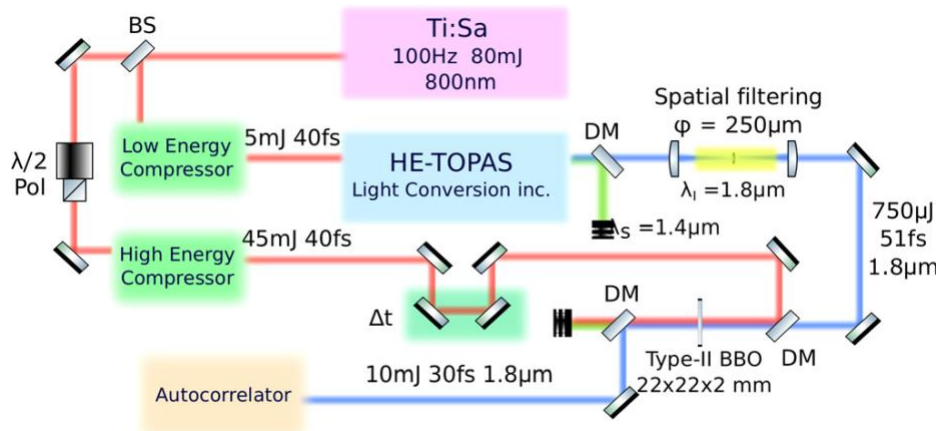


Figure 2-3 The schematic diagram of the OPA based laser source [2].

The sapphire crystal in OPA can be rotated around its optic axis to tune the signal and idler photon. The OPA laser source in ALLS is parametrically amplified using a Beta barium borate (**BBO**)

crystal pumped with the 800 nm pump laser having 45 mJ of pulse energy at 40 fsec pulse duration, achieving up to 10 mJ of amplified OPA pulse energy at 1800 nm laser wavelength. The schematic diagram of the amplified OPA based laser source is shown in Figure 2-3. A maximum of 10 mJ pulse energy at 1800 nm laser wavelength at a pulse duration of 30-50 fs can be obtained. See reference [2] for a detailed description of the laser source.

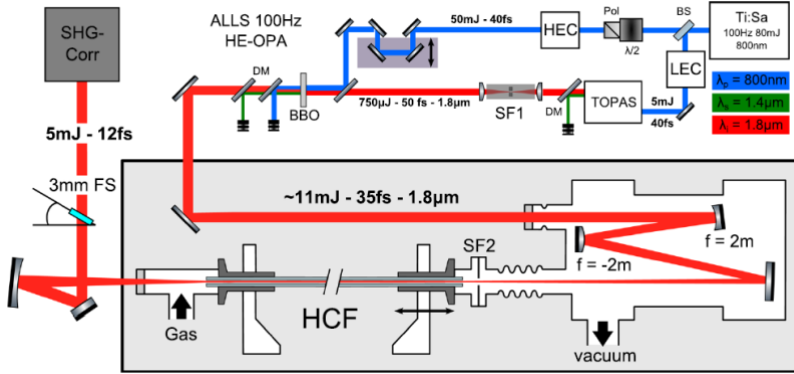


Figure 2-4 The experimental setup for the generation of intense few-cycle mid-infrared pulses [3].

2.2 Hollow-core Fiber Setup for Few-cycle Laser Pulses

The OPA laser pulse duration of 30-50 fs is further compressed by achieving the spectral broadening of the OPA laser pulses through self-phase modulation in a long 3-meter hollow-core fiber filled with the argon gas. A concave mirror with a focal length of 2 meters is used to focus the laser pulses into the hollow-core fiber. The long fiber length along with the long focal length of the concave mirror allows the focused laser power to be distributed over a longer length, and hence avoids gas ionization in the fiber over higher values of laser pulse energies. The spectral broadening achieved in the fiber can support shorter pulse durations. To compensate for the dispersion effects accumulated in the fiber, CaF₂ windows of various thicknesses were used to achieve the minimum possible laser pulse duration. With the mid-infrared central wavelength of 1800 nm, a maximum of 5 mJ of pulse energy with a 12 fsec (two-cycle) laser pulse duration can be achieved with this setup. A detailed description of the setup can be found in reference [3].

2.3 HHG Setup

The schematic diagram of the experimental setup for the HHG from LAP is shown in Figure 2-5. The output of the amplified Ti:sapphire laser system (210 picoseconds, 100 Hz, 800 nm) is split

into two beams using a 30/70 beam splitter. The 30% part of the beam, called the pre-pulse, is focused onto a solid target (mounted on an XYZ translation stage) with pre-pulse energy adjusted to 1.0-2.0 mJ, creating an intensity of $\sim 10^{10} \text{ W cm}^{-2}$ at the solid target surface for the LAP formation.

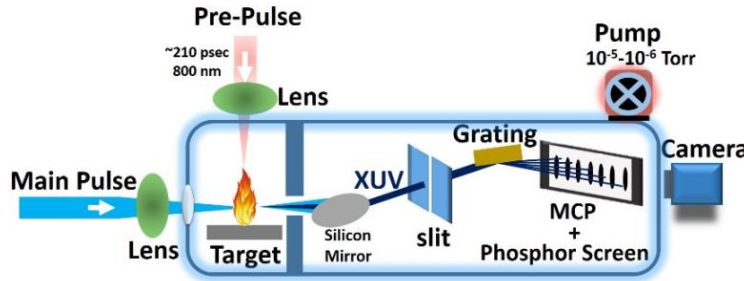


Figure 2-5 Schematic diagram of the experimental setup for the HHG from LAP.

The optical delay between pre-pulse and main pulse at the solid target was chosen to maximize the XUV flux, with a typical value of 25-80 nsec, the exact value being different for the different solid targets used. The 70% beam, called the main pulse, is the compressed fs pulse. This main pulse could be the amplified compressed output from the 10 Hz or 100 Hz laser system based on the Ti:sapphire laser oscillator. The main pulse could also be the amplified output of our OPA laser system operating in the mid-infrared wavelength range or the few-cycle output from our OPA setup coupled with the long hollow-core fiber compression system. The typical main-pulse energy used is 1.0-10 mJ, which is focused onto the LAP at an intensity of $1.0\text{-}7.0\times 10^{14} \text{ W cm}^{-2}$, the exact choice depending upon the type of experiment performed. For the experiment using 400 nm laser pulses, the compressed 800 nm output of the Ti:sapphire laser is frequency-doubled using a BBO crystal and separated from the collinear 800 nm laser wavelength using a dichroic mirror, generating 400 nm laser pulses with a pulse duration of 57 fs. Similarly, for experiments with near-infrared wavelengths (860-940 nm), the parametrically amplified tunable mid-infrared output of the OPA is frequency-doubled using a BBO crystal and filtered using a dichroic mirror. The generated XUV pulse and co-propagating driving laser pulse are split using a silicon mirror placed at a Brewster angle of the main pulse, thereby reflecting only the XUV pulse into the XUV spectrometer. The XUV pulse is frequency dispersed by the XUV spectrometer comprising a fixed vertical slit, a cylindrical flat-field XUV grating (Hitachi, 1200 lines/mm), a microchannel plate, and a phosphor screen. The harmonics are captured using a 16-bit CMOS camera (model PCO-

edge, PCO AG, Germany). The solid target, silicon mirror and XUV spectrometer are kept inside a vacuum of 10^{-5} - 10^{-6} torr.

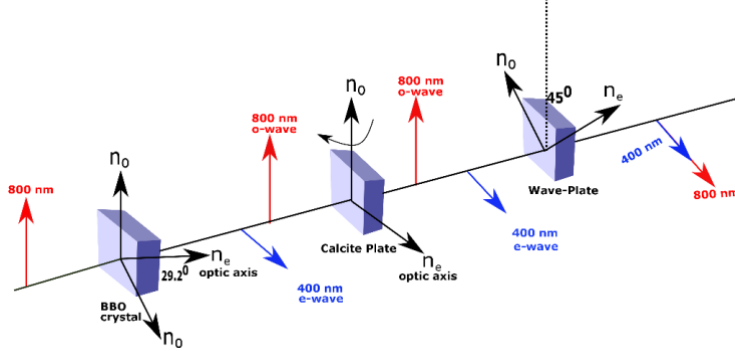


Figure 2-6 Schematic diagram of the two-color HHG setup.

Due to the underlying symmetry in the driving laser electric field (symmetry in the laser electric field in the positive and negative half cycle), and the symmetry associated with the nonlinear media (atomic or ionic), only the odd-order harmonics are generated due to the destructive interference between the different even order harmonics. To generate the even-order harmonics, this symmetry needs to be broken. One method to achieve this symmetry breaking is by adding the second harmonic laser pulse onto the fundamental driving laser pulse, provided the temporal and spatial overlap is achieved between the two pulses (800+400nm, for example). Such a setup is called the two-color HHG setup, and its schematic diagram is shown in Figure 2-6. A type-I BBO crystal of thickness 0.2 mm is used to generate the second harmonic of the 800 nm laser wavelength. The temporal delay between the two pulses is achieved by passing through the birefringent calcite crystal. The polarization of the 800 nm and 400 nm pulses is made parallel by passing the laser beam through the dual-wavelength waveplate (half waveplate for the 400 nm and full waveplate for the 800 nm pulses). The calcite crystal can be rotated to adjust the time delay between the 400 nm and 800 nm laser pulses.

2.4 Laser-ablation Optimization

Due to the photoionization process, the density of the free electrons in the LAP needs to be optimized to achieve the best possible phase-matching at the given experimental conditions. The pre-pulse intensity at the solid target for the LAP formation is crucial to avoid the phase-mismatch introduced by excessive free-electron density in the LAP resulting in the diminished high-order

harmonic flux. Therefore, it is important to find suitable pre-pulse intensity as well as the suitable pre-pulse focal spot for the optimum phase-matching.

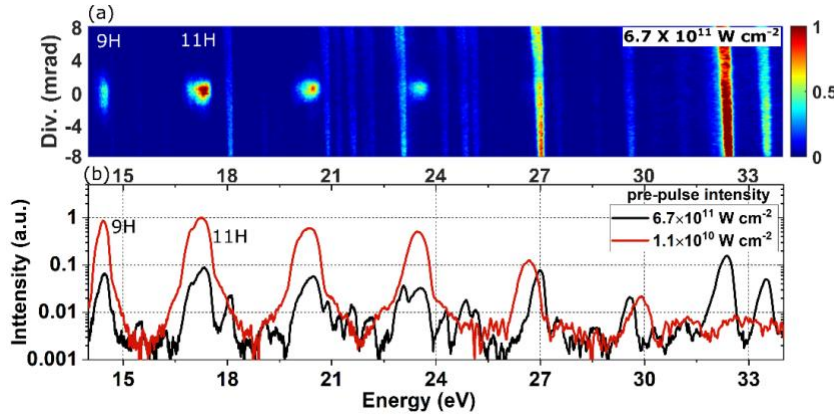


Figure 2-7 (a) The HHG spectrum generated from graphite LAP at a pre-pulse intensity of $6.7 \times 10^{11} \text{ W cm}^{-2}$. At this high pre-pulse intensity, the HHG spectrum is accompanied by the incoherent spontaneous emission from various atomic and ionic species in the LAP seen as the vertical lines. (b) The line plot comparing the HHG flux from graphite when the lower pre-pulse intensity of $1.1 \times 10^{10} \text{ W cm}^{-2}$ at the target surface (achieved by moving the pre-pulse laser spot 7 mm inside the graphite target surface) is used.

For the harmonic spectrum shown in Figure 2-7(a), the focal spot diameter for the pre-pulse is 30 μm , and at 1.0 mJ of pre-pulse energy with a pulse duration of 210 psec, this results in a laser intensity of $6.7 \times 10^{11} \text{ W cm}^{-2}$ at the solid target surface. At this high pre-pulse laser intensity, the generated weak HHG spectrum is typically accompanied by many incoherent spontaneous emission lines. The weak high-order harmonic emission is due to the phase-mismatch introduced by the excessive electron density in the LAP, as seen in Figure 2-7(a). However, when the focal spot of the pre-pulse is moved 7 mm inside the plasma, with the focal spot size at the target surface to be 240 μm , the laser intensity at the solid target surface reduces to $1.1 \times 10^{10} \text{ W cm}^{-2}$. At this lower pre-pulse intensity, no spontaneous emission is observed, and an increase in the high-order harmonic flux by more than an order of magnitude is observed due to better phase-matching, as seen in Figure 2-7(b).

2.5 References

1. D. Strickland and G. Mourou, "Compression of amplified chirped optical pulses," *Optics Communications* **55**, 447–449 (1985).
2. N. Thiré, S. Beaulieu, V. Cardin, A. Laramée, V. Wanier, B. E. Schmidt, and F. Légaré, "10 mJ 5-cycle pulses at 1.8 μm through optical parametric amplification," *Applied Physics Letters* **106**, 091110 (2015).
3. V. Cardin, N. Thiré, S. Beaulieu, V. Wanier, F. Légaré, and B. E. Schmidt, "0.42 TW 2-cycle pulses at 1.8 μm via hollow-core fiber compression," *Applied Physics Letters* **107**, (2015).

Chapter 3

Resonant High-order Harmonic Generation in Multiphoton-Ionization Regime

3.1 Introduction

HHG is an excellent source of coherent fs pulses of XUV and soft X-ray radiation, and is a powerful method to study the electronic and structural dynamics of atoms and molecules with fs temporal resolution [1] [2]. The harmonic spectrum from a typical noble gas is broadband containing high-order harmonic series. However, many applications require intense quasi-monochromatic (**QM**)-XUV pulses, such as XUV pump-probe spectroscopy [3], XUV lithography [4], XUV diffractive imaging [5] and time-resolved photoemission spectroscopy (*e.g.*, ARPES and PEEM) [6][7]. The intense QM-XUV sources are also important because they are central to the scientific domain of XUV nonlinear optics investigating the nonlinear laser-matter interactions in the XUV, such as high charge state production through the multi-XUV-photon absorption in noble gases [8]. The observations of two-photon double ionization, two-photon above-threshold ionization and XUV induced Coulomb explosion are some of the nonlinear optical phenomena that have made significant breakthroughs with their contribution towards the techniques of temporal characterization of attosecond pulses [9]. The international free-electron laser (**FEL**) community would also merit from intense QM-XUV sources, which could be used as a seed to improve FEL brightness and temporal coherence, as well as to reduce their background noise [10].

The traditional QM-XUV sources used by the scientific community are the synchrotron-based XUV sources and the XUV FELs [11]. Synchrotron sources produce XUV pulses typically with a duration of a few tens of picoseconds. This long time-scale renders synchrotron radiation ineffective for studies requiring fs time-scale resolution. Although complex beam manipulation techniques when integrated into a synchrotron facility could generate 100 fs radiation, the added complexity and the financial expenses associated with the construction and maintenance of a synchrotron facility leave many researchers with the lack of access to such an exotic light source [12][13]. FELs, on the other hand, can produce fs XUV pulses with several microjoules of QM-XUV pulse energies, but the access to this giant multimillion-dollar facility (on a scale of a few \$100 million range) is also limited to a few groups of scientists [11].

HHG is an alternative lab-scale tabletop source of coherent fs XUV radiation [14][15]. However, today, the majority of HHG experiments performed using Ti:sapphire 800 nm fs lasers and long mid-infrared fs lasers have laser parameters satisfying the TI regime of the Keldysh theory [15][16], and hence involve laser-matter interaction in the TI regime [14]. The Keldysh parameter is defined as $\gamma = \sqrt{I_p/2U_p} = 0.231\sqrt{I_p/I\lambda^2}$ (where I_p is the ionization energy in eV, I is the laser intensity in units of 10^{14} W/cm 2 , λ is the laser wavelength in μm , and U_p is the ponderomotive energy in eV, and is given by $U_p = 9.34 I\lambda^2$). The Keldysh parameter categorizes the laser-matter interaction broadly into two regimes; MPI regime for $\gamma > 1$ and TI regime for $\gamma < 1$. Therefore, the TI regime implies a large U_p compared to the I_p and vice versa for MPI. One significant feature of HHG in the TI regime is the generation of a long plateau of high-order harmonics, and hence a very broadband XUV emission. This is a critical issue for the HHG based sources that need to be employed for experiments requiring intense fs QM-XUV radiation, and therefore is a hurdle that needs to be solved to advance the field of intense laser-matter interactions based on the intense tabletop lab-scale XUV sources. The traditional approach to tackle this issue is to extract a single harmonic order from the broadband harmonic spectrum using XUV optics, for example, a grazing incidence grating monochromator [17]. This results in the reduction of harmonic flux due to the finite diffraction efficiency of the grating monochromator (typical loss > 70%) [17]. The low HHG CE is another critical issue (typically 10^{-6} - 10^{-7}), generating harmonic energy per pulse at the nJ scale [18]. Attempts are also being made to selectively amplify a single harmonic order by using a plasma-based XUV-amplifier, with studies demonstrating the amplification of an initial 35 nJ harmonic energy up to 0.7 μJ [19]. However, the Joule-level pumping laser source required in these studies limits the XUV repetition rate. Further, the temporal duration of the XUV pulse is elongated due to the bandwidth of the gain medium, which is typically in the picosecond regime. To overcome these obstacles, an alternative and promising XUV source is the QM RH generation from the LAP with a high CE of 10^{-4} [15]. A suitable LAP source can generate an intense μJ -level single XUV RH with an order of magnitude ER relative to the neighboring harmonics [20]. The LAP technique can generate stable harmonics for several minutes at kHz level repetition rates by using rotating cylindrically shaped ablation targets [21][22]. Although μJ -level harmonic energies have also been demonstrated from gases, such experiments are complicated to implement. They either require several meters long loose-focusing geometries to generate a large laser-interaction volume in the gas, or the intricate process of employing

multiple gas jets along with careful optimization of nonlinear media configuration to achieve the higher XUV CE [8] [23].

Since the experiments generating QM-XUV from RH in LAPs using 800 nm Ti:sapphire fs lasers and long mid-infrared lasers also involve laser-matter interaction in the TI regime, the long plateau of harmonics again limits the ER and hence the monochromaticity of the generated XUV. Up to now, there did not exist a method to increase the ER and intensity of the single RH. As a step ahead in finding a solution to this problem, we note that RH in the MPI regime has not been investigated up to now. Although a few past experiments on HHG from LAP were performed with shorter UV laser wavelengths, thereby resulting in conditions for the MPI regime, RHs were not observed [24], and thus they remain unexplored for this regime of interaction. In this chapter, we explore the perspective of RH generation in the MPI regime. We use gallium LAP for the HHG, and obtain the conditions for the MPI regime, *i.e.*, $\gamma > 1$ by choosing suitable driving laser parameters.

3.2 Experimental Results

3.2.a RH Generation with Near-Infrared Laser Wavelengths from Ga^+

We use different near-infrared laser pulses driving the Gallium LAP for HHG, and the generated HHG spectrums are shown in Figure 3-1. The pre-pulse energy used is 1.0 mJ, creating an intensity of $\sim 10^{10} \text{ W cm}^{-2}$ at the solid target surface for LAP formation. The optical delay between pre-pulse and main-pulse at the solid target was kept at 55 nsec providing the maximum XUV flux. The parametrically amplified tunable mid-infrared output of the OPA is frequency-doubled using a BBO crystal. The generated near-infrared laser pulses with a pulse duration of 40 fs and pulse energy of 1.5 mJ are focused onto the LAP at an intensity of $1.7 \times 10^{14} \text{ W cm}^{-2}$. The main-pulse spot diameter at the focus position is imaged and measured to be 100 μm for the 860 nm laser wavelength. The laser focus of the main pulse was kept 12.3 mm after the LAP, which was the optimal position generating maximum XUV flux at given experimental conditions. Ga^+ ($I_p=20.52 \text{ eV}$) exhibits a strong resonance in the photoionization cross-section (**PICS**) with a magnitude of 300 Mbar centered at 21.9 eV, corresponding to the strong radiative transition $3d^{10}4s^2 \text{ }^1S_0 \rightarrow 3d^94s^24p \text{ }^3P_1$ [25]. The Keldysh parameter at 860 nm is 0.935. The state $3d^94s^24p \text{ }^3P_1$ corresponds to the AIS of Ga^+ and the electronic transition from AIS into the ground state $3d^{10}4s^2 \text{ }^1S_0$ is resonant with 15 photons of 860 nm laser field. It is expected that an enhancement or resonance in the PICS can result in an increase in the harmonic intensity at resonant photon energy [26], and we see an intense RH at the 15th harmonic (15H).

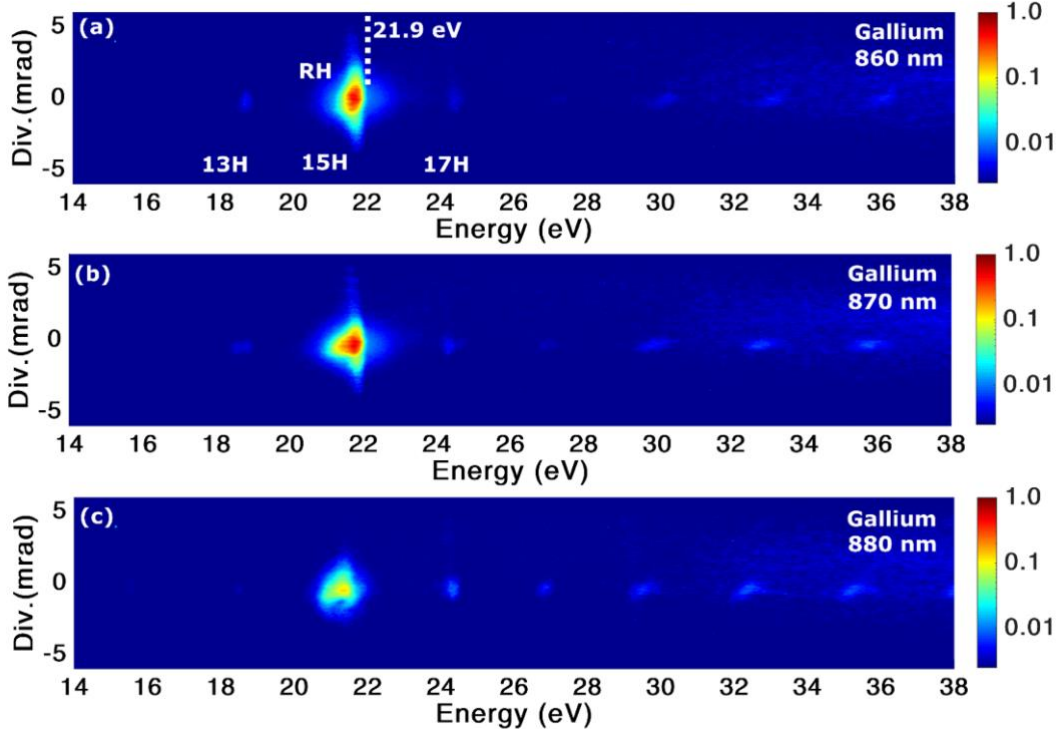


Figure 3-1 HHG spectra generated from Ga^+ , using (a) 860 nm, (b) 870 nm and (c) 880 nm laser wavelength. The $3\text{d}^{10}4\text{s}^2\text{1S}_0 \rightarrow 3\text{d}^94\text{s}^24\text{p}^3\text{P}_1$ resonance of Ga^+ at an energy of 21.9 eV is 15 photons resonant with the 860 nm wavelength, resulting in an intense RH emission at 15H. The RH intensity decreases when the laser wavelength is tuned away from the resonance, as shown in (b) and (c). The laser intensity used to generate each harmonic spectrum is $1.7 \times 10^{14} \text{ W cm}^{-2}$.

We define the experimentally observed ER for the RH with the equation $ER = 2I_q/(I_{q-2} + I_{q+2})$, where I_q is the integrated intensity of RH having order q . At 860 nm laser wavelength, the ER observed is 136. The intensity of 15H decreases as the laser wavelength increases to 870 nm and 880 nm, due to increased off-resonance from the strong radiative transition at 21.9 eV.

3.2.b HHG at Higher Keldysh Parameter

To investigate the response of RH from Ga^+ at higher Keldysh parameters, we used a shorter driving laser wavelength of 400 nm. Figure 3-2 shows the intense RH observed at a laser intensity of $1.6 \times 10^{14} \text{ W cm}^{-2}$ with laser focus kept 10.1 mm after the LAP. The 21.9 eV resonance is 7-photon resonant with the 400 nm driving laser photon, generating an intense 7H. The value of U_p and I_p is 2.39 eV and 20.52 eV, respectively, resulting in a Keldysh parameter of 2.07. The I_p is more than 8 times higher compared to the U_p , and RH is generated in the MPI regime.

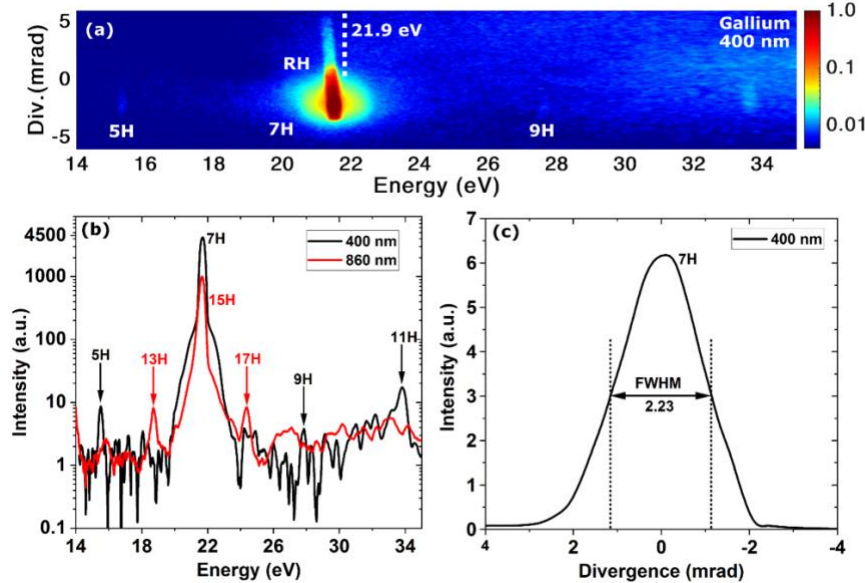


Figure 3-2 HHG spectra generated from Ga^+ , using (a) 400 nm laser wavelength, showing an intense RH near 21.9 eV, and other non-resonant harmonics very weak relative to the RH. (b) The vertically integrated line profile of RH from Ga^+ using 400 nm and 860 nm laser wavelength. The peak intensity of RH of Ga^+ with 400 nm laser wavelength is observed to be 4.5 times stronger than the RH with 860 nm laser wavelength, stronger due to the low number of laser photons required for resonance with the AIS using the former wavelength. (c) The FWHM divergence of RH is 2.23 mrad, indicating the coherent nature of RH emission. The laser intensity used to generate harmonic spectrum at 400 nm and 860 nm wavelength is $1.6 \times 10^{14} \text{ W cm}^{-2}$ and $1.7 \times 10^{14} \text{ W cm}^{-2}$, respectively.

The ER observed using 400 nm laser wavelength is 714. The highest ER value reported before this work was from indium LAP generating an intense RH with an ER of ~ 100 [20]. Therefore, the ER of 714 observed in our experiment under the MPI regime is the highest value reported so far using the LAP technique, making gallium LAP a source of intense RH with unprecedented monochromaticity from a high-order harmonic source.

3.2.c HHG Intensity Comparison from Different LAPs

The harmonic intensity comparison from gallium, graphite and tin LAP is shown in Figure 3-3 with the corresponding laser parameters listed in Table 3.1. The optical delay between the prepulse and the main pulse was kept at 35 nsec, 55 nsec and 70 nsec for graphite, gallium and tin LAP, respectively, providing the maximum harmonic flux. The laser intensity at each LAP is $\sim 1.6 \times 10^{14} \text{ W cm}^{-2}$.

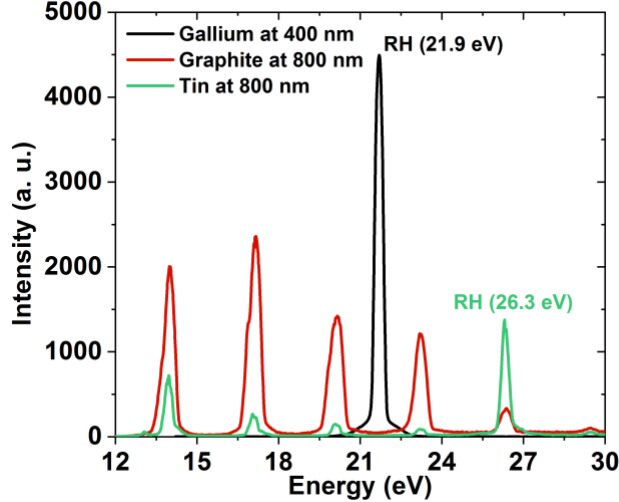


Figure 3-3 The comparison of RH intensity from Ga^+ with other LAPs known to generate intense harmonics.

The RH of Ga^+ at 21.9 eV has a peak intensity 3.3 times higher than the RH of tin, demonstrating the RH of Ga^+ as a potential source of multi- μJ harmonic energy. Since both graphite LAP as well as the RH of tin LAP at 26.3 eV have demonstrated μJ -level harmonic energies at 10^{-4} level CE [27][28], the relative comparison of RH intensity of Ga^+ establishes it as a potential source of intense QM-XUV with multi- μJ pulse energy.

Table 3.1 The laser parameters used for HHG from different LAPs

Target	laser pulse energy (mJ)	laser pulse duration (fs)	focal diameter (μm)	focal spot location behind the target surface (cm)	laser intensity at the LAP (W cm^{-2})
Gallium	1.3	57	40	1.0	1.60×10^{14}
Graphite	1.2	40	90	1.1	1.62×10^{14}
Tin	1.4	40	90	1.2	1.68×10^{14}

3.3 Coherence

HHG is a coherent process, *i.e.*, all the atoms/ions taking part in the HHG constructively add their harmonic signal coherently. Consequently, the harmonic signal builds up that co-propagates with the driving laser beam. This process is distinct from the incoherent spontaneous emission in all directions, *i.e.*, in a solid angle of 4π steradians [29]. Therefore, the coherence of the RH can be confirmed by measuring its divergence, which is shown in Figure 3-2(c). The FWHM divergence of RH is 2.23 mrad, which is significantly smaller than the 20 mrad divergence of the coherent

driving laser beam. The FWHM bandwidth of the generated 21.9 eV RH is 0.28 eV, which is broad enough to support a 6.5 fs pulse duration for a Fourier-transform limited pulse.

3.4 RH Generation Mechanism in the MPI Regime

In the TI regime, the mechanism of RH generation for most materials can be explained by the four-step model [30]. The first two steps of this model are the same as the three-step model, *i.e.*, TI of the valence electron and its acceleration within the continuum [30]. The third step, however, involves resonant capture of the tunnel-ionized electron into the AIS, *i.e.*, a discrete state embedded in the continuum, which is followed by the fourth step involving a radiative transition from AIS to the initial ground state emitting RH [30][31][32]. The RH generation mechanism in the MPI regime can be similar to the four-step model applicable for RH generation in the TI regime, incorporating multiphoton resonant up-transition from the ground state into the AIS, instead of capturing of the tunnel-ionized electron by AIS in the continuum. The radiative one-photon down-transition from AIS into the ground state will emit XUV with intensity proportional to the down-transition amplitude. This will essentially form a two-step model with the inclusion of AIS [33][34][35]. The higher RH intensity and ER in the MPI regime relative to the TI regime could be attributed to the electronic wave-packet spreading after photoionization in the TI regime: the wave packet spreads at the second step of the four-step model, which populates AIS with relatively low probability. This spreading is absent in the MPI regime where AIS is populated directly from the ground state. The temporal coherence of the RH emission can be related to a very short lifetime of AIS $3d^94s^24p\ ^3P_1$ involved, which can be retrieved from the corresponding linewidth. The AIS linewidth is $\Gamma=142$ meV, resulting in a very short lifetime of $\tau \sim 4.6$ fs (\hbar/Γ).

3.5 Calculations of Resonance Transition Parameters

3.5.a Line Identification

We performed extensive calculations for the ground state $3d^{10}4s^2$ and the AIS $3d^94s^24p\ ^{1,3}P_1, ^3D_1$ of Ga^+ in the multiconfiguration Hartree-Fock (**HF**) approximation with the Breit–Pauli corrections [36]. The results showed that the resonance at 21.9 eV, attributed in Ref. [37] to the AIS $3d^94s^24p\ ^3P_1$ consists of two overlapping AISs with the total angular momentum $J=1$ and dominant components $3d^94s^24p\ ^1P_1$ (84%) and 3D_1 (87%), respectively, while the 3P_1 (97%) resonance is located at 0.94 eV lower excitation energy. This is in good agreement with the calculations [37], although their excitation energies are shifted approximately by 0.9 eV probably

because of a small number of configurations taken into account and mostly phenomenological treatment of strong electron correlations within the core. Our results are in accordance with the photoabsorption spectrum [38] with a comparatively weak line at 20.975 eV and a strong double structure at 21.88 eV (Figure 3-4) and with the detailed analysis [39] of the photoabsorption spectrum of the Zn atom with the identical electron configuration.

3.5.b Spectroscopic Characteristics of the AIS

We have extracted the parameter set of the strong radiative transition $3d^{10}4s^2\ ^1S_0 \rightarrow 3d^94s^24p\ ^1P_1$ (in our classification) at the energy of 21.9 eV directly from highly accurate absolute photoabsorption cross-section data [37]. These data in the vicinity of the AIS can be fitted by the Fano [40] curve for a single ionization channel.

$$\sigma(E) = \sigma_0 \frac{(q + \varepsilon)^2}{\varepsilon^2 + 1}, \quad (1)$$

where $\varepsilon=2(E-E_r)/\Gamma$ is the reduced photon energy, E_r and Γ are the position and the width of the AIS, respectively, σ_0 is the direct ionization cross-section, and q is the asymmetry index. However, there is a structure near the line center (see Figure 3-4) caused by interference [41] with the narrow AIS 3D_1 . Instead of Eq. (1), we apply Eq. (7) from Ref. [42] to take this effect into account,

$$\sigma(E) = \sigma_0 \left[1 + \rho_B^2 \frac{q_B^2 - 1 + 2q_B\varepsilon_B}{\varepsilon_B^2 + 1} + \tilde{\rho}_n^2 \frac{\tilde{q}_n^2 - 1 + 2\tilde{q}_n\varepsilon_n}{\varepsilon_n^2 + 1} \right], \quad (2)$$

where ε_B and ε_n are the reduced energies for the broad and the narrow AISs, respectively. The Fano-like parameters $\tilde{\rho}_n$ and \tilde{q}_n for the narrow AIS as well as the parameters of the AIS coupling via continuum states are described in Ref. [42]

To minimize the number of fitting parameters, we express the quantities in Eq. (2) in terms of experimental widths of the 3P_1 and 1P_1 AISs and the HF expansion coefficients of the AIS $J=1$ wave functions. The remaining fitting parameters are σ_0 , q_B , E_B , Γ_B , E_n and Q_{Bn} . The latter defines the relative strength of the Hermitian and non-Hermitian coupling between the resonances [43], which appears sensitive to the fitting procedure (we obtained the value $Q_{Bn}=0.8$). The results of the fit are shown in Figure 3-4. Note that calculations give a stronger narrow dip, which should be partly smoothed by an actual experimental resolution.

Since the experimental curve is nearly symmetric (the direct cross-section is small and the 1P_1 resonance dominates over the 3D_1 one), and its profile is almost Lorentzian.

$$\sigma(E) = \frac{4\pi\alpha}{\Gamma} f_{ga} \frac{1}{\varepsilon^2 + 1}, \quad (3)$$

where α is the fine structure constant, Γ is in atomic units, f_{ga} is the oscillator strength of the transition $g \rightarrow a$. From Eqs. (1) and (3) the oscillator strength in terms of the Fano fitting parameters is

$$f_{ga} = \frac{1}{4\pi\alpha} \Gamma_B \sigma_0 q_B^2, \quad (4)$$

where σ_0 is in atomic units, which gives the value $f_{ga}=0.66$.

3.6 Calculation of the RH Generation

This section describes our numerical approach for the HHG spectrum calculation. It is based on the numerical solution of the 3D time-dependent Schrödinger equation (**TDSE**). The numerical solution of the TDSE for a multielectronic system in an intense laser field is still a challenging task, which is hardly solvable except for helium-like atoms and ions. So, we are using a single-active electron approximation, and the role of the other electrons is reproduced with a modification of the parent ion potential as it was done in references [44] [45] [32]. The used potential supports a quasi-stable state which models the AIS in the actual ion. The potential is (in atomic units):

$$V(\mathbf{r}) = -\frac{2}{\sqrt{a_0^2 + r^2}} + a_1 \exp \left[-\left(\frac{r - a_2}{a_3} \right)^2 \right]. \quad (5)$$

Table 3.2 Parameters of the $3d^94s^24p\ ^1P_1$ AIS in Ga^+ obtained by fitting to the experimental data [38] and from the TDSE calculations with the model potential (5).

	Ga^+	TDSE with model potential
Ionization energy (eV)	20.52*	20.17
Excitation energy E_B (eV)	21.88	21.80
Autoionization width (eV)	0.152	0.142

* From handbooks.

The fitting parameters a_0 , a_1 , a_2 , and a_3 are chosen to reproduce the ionization energy of Ga^+ and the spectroscopic parameters of the $3d^{10}4s^2\ ^1S_0 \rightarrow 3d^94s^24p\ ^1P_1$ transition found in the previous section. The found values are $a_0=0.65$, $a_1=1.1$, $a_2=3.7$, and $a_3=1.5$. In Table 3.2, we compare the

properties found in our model TDSE calculations and the ones of the real Ga^+ . The numerical method for the TDSE solution is described in Ref [46].

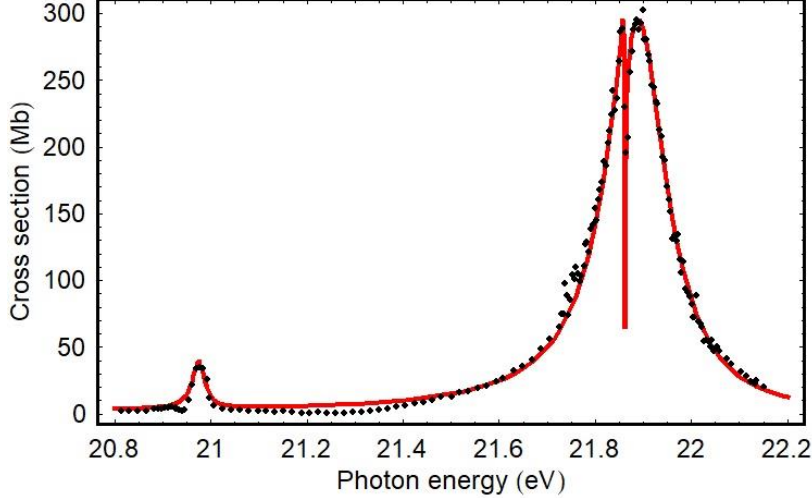


Figure 3-4 . Fitting of the curve (2) (red line) to the experimental absorption data [38] (black points). The parameters of the dominant AIS $3d^94s^24p\ ^1P_1$ are $E_B=21.88$ eV, $\Gamma_B=0.152$ eV, $q_B=-35.5$, $\sigma=2.5\times10^{-19}$ cm 2 and $Q_{Bn}=0.8$.

We summarize in Table 3.3 the ER obtained experimentally using 400 nm and 860 nm laser wavelengths. The ER observed using 400 nm laser wavelength is 714. The highest ER value reported so far is from indium LAP generating an intense RH with an ER of ~ 100 [20]. Therefore, the ER of 714 observed in our experiment under the MPI regime is the highest value reported so far using the LAP technique, making gallium LAP a source of intense RH with unprecedented monochromaticity from a high-order harmonic source.

Table 3.3 The experimentally observed and calculated ER values using 3D-TDSE from Ga^+ .

Experiment			
Laser Wavelength (nm)	Laser Intensity (W cm $^{-2}$)	Keldysh parameter	ER
860	1.7×10^{14}	0.935	136
400	1.6×10^{14}	2.07	714
Calculated			
Laser Wavelength (nm)	Laser Intensity (W cm $^{-2}$)	Keldysh parameter	ER
850	5×10^{14}	0.55	71
400	5×10^{14}	1.17	352
850	3×10^{14}	0.71	103
400	3×10^{14}	1.51	633

3.7 Spatial Distribution of the Electron Wave-packet in the TI and MPI Regime

In the numerical solution of 3D-TDSE, we find the electron wave function $\psi(r, z, t)$ as a function of time and space (z is the laser field direction and r is the radial direction), and then calculate its spectrum $\tilde{\psi}(r, z, \omega)$. In Figure 3-5, we present the spatial distribution $|\tilde{\psi}(r, z, \Omega)|^2$ for the fixed frequency Ω , namely for the frequency equal to the AIS energy, in the logarithmic scale. The calculation is done for the MPI (resonance at H7, in Figure 3-5(a)) and TI (resonance at H15, in Figure 3-5(b)) regime. In both figures, one can see the part of the wave function that is well-localized near the origin, within the size of several atomic units. This part can be attributed to the AIS. However, in the TI regime depicted in Figure 3-5(a) and Figure 3-5(b), there is also a very pronounced part of the wave function localized within a much larger volume; its size in the laser field direction is approximately defined by the free-electron oscillation amplitude R_{osc} . Thus, this distribution agrees with the four-step model for the population of the AIS in the TI regime: the AIS population is necessarily accompanied by the electron free-motion in the continuum, and thus by the delocalization of the electron wave-packet.

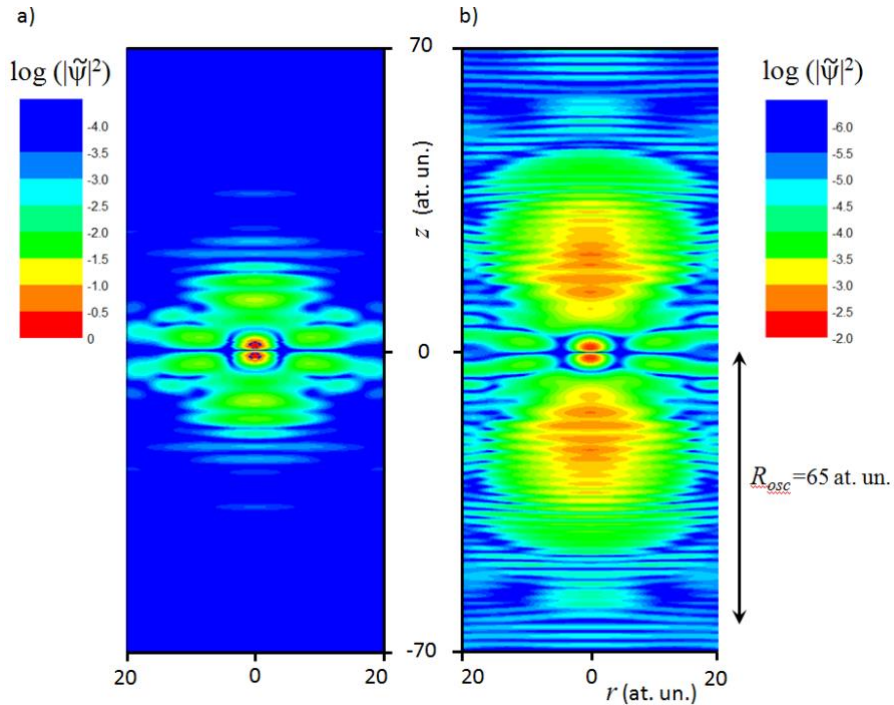


Figure 3-5 Calculated spatial distribution of the electron with the energy of the AIS (see text for more details) for the (a) MPI and (b) TI regime. The laser intensity is $3 \times 10^{14} \text{ W/cm}^2$, the wavelength is (a) 400 nm and (b) 850 nm. One can see that in the former case, the electron is much more localized near the origin.

On the contrary, in Figure 3-5(a), *i.e.*, in the MPI regime, the electron wave-packet is much more compact. Note that the observed density distribution cannot be attributed just to the smaller R_{osc} for the MPI regime. Indeed, in Figure 3-5(b), the density within several atomic units near the origin is comparable to the maximal density of the free wave-packet. The maximal density in Figure 3-5 (a) is much higher than that in Figure 3-5(b). This agrees with the picture of the *direct* AIS population in the MPI regime, as described in our paper. The observed compact electron distribution in the MPI regime leads, in particular, to approximately two orders of magnitude higher population density near the origin (note the difference in the color scale in the two figures), *i.e.*, to a much higher population of the AIS in the MPI regime. This explains the higher RH intensity observed in our experiments in the MPI regime.

3.8 Summary of the Chapter

In summary, we presented the study of resonant HHG in the previously unexplored MPI regime. We observe that one could obtain an intense RH with a superior monochromaticity by operating at higher values of the Keldysh parameter. This in other words implies that for a given laser intensity, by using driving lasers with shorter wavelengths and hence by increasing the Keldysh parameter, one could increase the ER for the RH relative to the neighboring harmonics. This increase in the ER is qualitatively reproduced through numerical simulations based on 3D-TDSE with a model potential. The calculations also reveal that this increase in the ER is due to the low electron wave-packet spreading in the MPI regime. This technique to increase the ER can be applied to any LAP exhibiting RH. We reveal that Ga^+ from the gallium LAP source driven by 400 nm fs laser pulses generates an intense single RH close to 21.9 eV having the potential of multi- μJ energy, with an unprecedented ER of 714. Our compact, intense XUV source can be integrated into any setup requiring QM-XUV radiation without XUV monochromator installation, preventing a substantial loss of XUV flux (typically $> 70\%$) due to the finite diffraction efficiency of the grating monochromator. The present results reveal a new method to increase the intensity and monochromaticity of intense multi- μJ fs XUV light, which will significantly advance the ultrafast XUV science. The intrinsically efficient XUV source would enable one to investigate XUV nonlinear dynamics of elements that were difficult with the conventional HHG sources delivering low photon flux on target element at the end-station. It will also pave the way towards understanding the involvement of AIS in generating RH in the MPI regime.

3.9 References

1. J. Itatani, J. Levesque, D. Zeidler, H. Niikura, H. Pépin, J. C. Kieffer, P. B. Corkum, and D. M. Villeneuve, "Tomographic imaging of molecular orbitals," *Nature* **432**, 867–871 (2004).
2. H. J. Wörner, J. B. Bertrand, D. v. Kartashov, P. B. Corkum, and D. M. Villeneuve, "Following a chemical reaction using high-harmonic interferometry," *Nature* **466**, 604–607 (2010).
3. F. Kelkensberg, C. Lefebvre, W. Siu, O. Ghafur, T. T. Nguyen-Dang, O. Atabek, A. Keller, V. Serov, P. Johnsson, M. Swoboda, T. Remetter, A. L'Huillier, S. Zherebtsov, G. Sansone, E. Benedetti, F. Ferrari, M. Nisoli, F. Lépine, M. F. Kling, and M. J. J. Vrakking, "Molecular Dissociative Ionization and Wave-Packet Dynamics Studied Using Two-Color XUV and IR Pump-Probe Spectroscopy," *Physical Review Letters* **103**, 123005 (2009).
4. L. R. Hughey, R. T. Williams, J. C. Rife, D. J. Nagel, and M. C. Peckerar, "Instrumentation for XUV lithography at SURF-II," *Nuclear Instruments and Methods in Physics Research* **195**, 267–271 (1982).
5. A. Ravasio, D. Gauthier, F. R. N. C. Maia, M. Billon, J.-P. Caumes, D. Garzella, M. Gélécoc, O. Gobert, J.-F. Hergott, A.-M. Pena, H. Perez, B. Carré, E. Bourhis, J. Gierak, A. Madouri, D. Mailly, B. Schiedt, M. Fajardo, J. Gautier, P. Zeitoun, P. H. Bucksbaum, J. Hajdu, and H. Merdji, "Single-Shot Diffractive Imaging with a Table-Top Femtosecond Soft X-Ray Laser-Harmonics Source," *Physical Review Letters* **103**, 028104 (2009).
6. E. J. Sie, T. Rohwer, C. Lee, and N. Gedik, "Time-resolved XUV ARPES with tunable 24–33 eV laser pulses at 30 meV resolution," *Nature Communications* **10**, 1–11 (2019).
7. O. Schmidt, M. Bauer, C. Wiemann, R. Porath, M. Scharte, O. Andreyev, G. Schönhense, and M. Aeschlimann, "Time-resolved two photon photoemission electron microscopy," *Applied Physics B* **74**, 223–227 (2002).
8. A. Nayak, I. Orfanos, I. Makos, M. Dumergue, S. Kühn, E. Skantzakis, B. Bodi, K. Varju, C. Kalpouzos, H. I. B. Banks, A. Emmanouilidou, D. Charalambidis, and P. Tzallas, "Multiple ionization of argon via multi-XUV-photon absorption induced by 20-GW high-order harmonic laser pulses," *Physical Review A* **98**, 023426 (2018).
9. K. Midorikawa, Y. Nabekawa, and A. Suda, "XUV multiphoton processes with intense high-order harmonics," *Progress in Quantum Electronics* **32**, 43–88 (2008).
10. G. Lambert, T. Hara, D. Garzella, T. Tanikawa, M. Labat, B. Carre, H. Kitamura, T. Shintake, M. Bougeard, S. Inoue, Y. Tanaka, P. Salieres, H. Merdji, O. Chubar, O. Gobert, K. Tahara, and M.-E. Couprise, "Injection of harmonics generated in gas in a free-electron laser providing intense and coherent extreme-ultraviolet light," *Nature Physics* **4**, 296–300 (2008).
11. C. Pellegrini, A. Marinelli, and S. Reiche, "The physics of x-ray free-electron lasers," *Reviews of Modern Physics* **88**, 015006 (2016).
12. R. W. Schoenlein, S. Chattopadhyay, H. H. W. Chong, T. E. Glover, P. A. Heimann, C. V. Shank, A. A. Zholents, and M. S. Zolotorev, "Generation of femtosecond pulses of synchrotron radiation," *Science* **287**, 2237–2240 (2000).
13. S. Khan, K. Holldack, T. Kachel, R. Mitzner, and T. Quast, "Femtosecond undulator radiation from sliced electron bunches," *Physical Review Letters* **97**, (2006).
14. C. Winterfeldt, C. Spielmann, and G. Gerber, "*Colloquium* : Optimal control of high-harmonic generation," *Reviews of Modern Physics* **80**, 117–140 (2008).
15. R. A. Ganeev, "High-order harmonic generation in a laser plasma: a review of recent achievements," *Journal of Physics B* **40**, R213 (2007).
16. R. A. Ganeev, L. B. Elouga Bom, and T. Ozaki, "High-order harmonic generation from plasma plume pumped by 400 nm wavelength laser," *Applied Physics Letters* **91**, (2007).
17. L. Poletto, P. Villoresi, E. Benedetti, F. Ferrari, S. Stagira, G. Sansone, and M. Nisoli, "Temporal characterization of a time-compensated monochromator for high-efficiency selection of extreme-ultraviolet pulses generated by high-order harmonics," *Journal of the Optical Society of America B* **25**, B44 (2008).
18. T. Ditmire, J. K. Crane, H. Nguyen, L. B. DaSilva, and M. D. Perry, "Energy-yield and conversion-efficiency measurements of high-order harmonic radiation," *Physical Review A* **51**, R902–R905 (1995).
19. Ph. Zeitoun, G. Faivre, S. Sebban, T. Mocek, A. Hallou, M. Fajardo, D. Aubert, Ph. Balcou, F. Burgy, D. Douillet, S. Kazamias, G. de Lachèze-Murel, T. Lefrou, S. le Pape, P. Mercère, H. Merdji, A. S. Morlens, J. P. Rousseau, and C. Valentin, "A high-intensity highly coherent soft X-ray femtosecond laser seeded by a high harmonic beam," *Nature* **431**, 426–429 (2004).
20. R. A. Ganeev, M. Suzuki, M. Baba, H. Kuroda, and T. Ozaki, "Strong resonance enhancement of a single harmonic generated in the extreme ultraviolet range," *Optics Letters* **31**, 1699 (2006).
21. C. Hutchison, R. A. Ganeev, T. Witting, F. Frank, W. A. Okell, J. W. G. Tisch, and J. P. Marangos, "Stable generation of high-order harmonics of femtosecond laser radiation from laser produced plasma plumes at 1 kHz pulse repetition rate," *Optics Letters* **37**, 2064 (2012).

22. G. S. Boltaev, V. V. Kim, M. Iqbal, N. A. Abbasi, V. S. Yalishev, R. A. Ganeev, and A. S. Alnaser, "Application of 150 kHz Laser for High-Order Harmonic Generation in Different Plasmas," *Photonics* **7**, 66 (2020).
23. J.-F. Hergott, M. Kovacev, H. Merdji, C. Hubert, Y. Mairesse, E. Jean, P. Breger, P. Agostini, B. Carré, and P. Salières, "Extreme-ultraviolet high-order harmonic pulses in the microjoule range," *Physical Review A* **66**, 021801 (2002).
24. Y. Akiyama, K. Midorikawa, Y. Matsunawa, Y. Nagata, M. Obara, H. Tashiro, and K. Toyoda, "Generation of high-order harmonics using laser-produced rare-gas-like ions," *Physical Review Letters* **69**, 2176–2179 (1992).
25. B. Peart, I. C. Lyon, and K. Dolder, "Measurements of absolute photoionisation cross sections of Ga⁺ and Zn⁺ ions," *Journal of Physics B* **20**, 5403–5410 (1987).
26. M. A. Fareed, V. V. Strelkov, M. Singh, N. Thiré, S. Mondal, B. E. Schmidt, F. Légaré, and T. Ozaki, "Harmonic Generation from Neutral Manganese Atoms in the Vicinity of the Giant Autoionization Resonance," *Physical Review Letters* **121**, 023201 (2018).
27. M. Suzuki, M. Baba, R. Ganeev, H. Kuroda, and T. Ozaki, "Anomalous enhancement of a single high-order harmonic by using a laser-ablation tin plume at 47 nm," *Optics Letters* **31**, 3306 (2006).
28. L. B. E. Bom, Y. Pertot, V. R. Bhardwaj, and T. Ozaki, "Multi-μJ coherent extreme ultraviolet source generated from carbon using the plasma harmonic method," *Optics Express* **19**, 3077 (2011).
29. V. V. K. & A. S. A. Mazhar Iqbal, Rashid A. Ganeev, Ganjaboy S. Boltaev, "Incoherent and coherent extreme ultraviolet emission from boron plasma," *The European Physical Journal D* volume **74**, 28 (2020).
30. V. Strelkov, "Role of Autoionizing State in Resonant High-Order Harmonic Generation and Attosecond Pulse Production," *Physical Review Letters* **104**, 123901 (2010).
31. V. V. Strelkov, M. A. Khokhlova, and N. Y. Shubin, "High-order harmonic generation and Fano resonances," *Physical Review A* **89**, (2014).
32. M. A. Fareed, V. V. Strelkov, N. Thiré, S. Mondal, B. E. Schmidt, F. Légaré, and T. Ozaki, "High-order harmonic generation from the dressed autoionizing states," *Nature Communications* **8**, 16061 (2017).
33. J. M. Ngoko Djokap and A. F. Starace, "Resonant enhancement of the harmonic-generation spectrum of beryllium," *Physical Review A* **88**, 053412 (2013).
34. J. M. Ngoko Djokap and A. F. Starace, "Origin of the multiphoton-regime harmonic-generation plateau structure," *Physical Review A* **102**, 013103 (2020).
35. A. I. Magunov and V. V. Strelkov, "Intensity of Resonant Harmonic Generated in the Multiphoton Ionization Regime," *Physics of Wave Phenomena* **28**, 369–374 (2020).
36. P. Froese Fischer, C., Brage, T., Jönsson, *Computational Atomic Structure. An MCHF Approach* (Bristol: Institute of Physics Publishing, 1997).
37. M. S. Pindzola, D. C. Griffin, and C. Bottcher, "Electron-impact excitation autoionization of Ga II," *Physical Review A* **25**, 211–218 (1982).
38. B. Peart, I. C. Lyon, and K. Dolder, "Measurements of absolute photoionisation cross sections of Ga⁺ and Zn⁺ ions," *Journal of Physics B* **20**, 5403–5410 (1987).
39. A. W. Fliflet and H. P. Kelly, "Photoionization cross section for the 4s subshell of Zn I," *Physical Review A* **10**, 508–517 (1974).
40. U. Fano, "Effects of configuration interaction on intensities and phase shifts," *Physical Review* **124**, 1866–1878 (1961).
41. F. H. Mies, "Configuration interaction theory. Effects of overlapping resonances," *Physical Review* **175**, 164–175 (1968).
42. A. I. Magunov, I. Rotter, and S. I. Strakhova, "Overlapping of Rydberg autoionizing states with a broad resonance in argon," *Journal of Physics B* **36**, L401 (2003).
43. I. Rotter, "A non-Hermitian Hamilton operator and the physics of open quantum systems," *Journal of Physics A: Mathematical and Theoretical* **42**, 153001 (2009).
44. V. Strelkov, "Role of autoionizing state in resonant high-order harmonic generation and attosecond pulse production," *Physical Review Letters* **104**, (2010).
45. M. Tudorovskaya and M. Lein, "High-order harmonic generation in the presence of a resonance," *Physical Review A* **84**, 013430 (2011).
46. V. V. Strelkov, A. F. Sterjantov, N. Y. Shubin, and V. T. Platonenko, "XUV generation with several-cycle laser pulse in barrier-suppression regime," *Journal of Physics B* **39**, 577 (2006).

Chapter 4

Intense Below-threshold Resonant-harmonic Generation from Laser-ablated Plume

4.1 Introduction

HHG is an important phenomenon in the field of strong-field laser-matter interaction that provides spatially and temporally coherent light source of single or a train of attosecond pulses in the XUV and the soft X-ray region of the electromagnetic spectrum [1][2][3][4]. HHG occurs when a high-intensity ultrashort driving laser pulse interacts with a nonlinear media, typically a gas or a LAP [5][6][7]. The HHG process generates radiation with photon energies at integral multiples of the driving laser photon energy, whose generation process can be explained by the semi-classical three-step model [8]. Past works have shown that the three-step model for the HHG mechanism may not explain many significant features of HHG. For example, it cannot explain the novel phenomenon of RH generation, which results in the generation of an intense single harmonic order with coherent intensity enhancement relative to the neighboring non-resonant harmonics. The RH enhancement has been reported in HHG from gaseous nonlinear media, such as the RH enhancement in Xenon [9], as well as in a variety of LAPs created from the laser-ablation of solid targets [6][10][11], with the potential of generating microjoule level harmonic energies [12][13]. The three-step model cannot explain the RH phenomenon because it considers the motion of only a single tunnel-ionized valence shell electron while completely ignoring the effect of inner-shell electrons in the parent ion, *i.e.*, the influence of the Coulombic interaction from the parent ion onto the motion of the electron in the continuum. The careful investigations on the RH phenomenon have uncovered the previously unknown physics of HHG processes, for example, the multi-electron dynamics in HHG mechanism [9], the role of AIS located in the continuum, and RH emission from the dressed-AISs perturbing the motion of the tunnel-ionized electron in the continuum [14][15][16].

There have also been considerable interests in HHG in the near-threshold regime, where the semiclassical three-step model results in an inadequate description of the phenomenon. For example, the anomalous ellipticity dependence of near-threshold harmonics, where the harmonic intensity is observed to be maximum for a non-zero driving laser ellipticity, cannot be fully

explained by the semiclassical model alone [17][18]. The step and dip structures [19] in the harmonic yield with a driving laser intensity scan due to quantum path interferences and the observation of negative group velocity dispersion [20] of near-threshold harmonics are some other interesting phenomena that do not strictly follow the three-step model. To better understand the mechanism of the generation of near-threshold harmonics, significant efforts have been made to modify the three-step model considering the Coulomb's potential of the parent atom or ion generating the harmonics [21]. However, more recent studies have revealed that the mechanism of near-threshold harmonics is a complex process, and more investigations need to be performed in this domain [22][23]. We note that studies of single RH enhancement so far have been reported only for harmonic photon energies above the I_p [6]. Search for the RH phenomenon in near-threshold harmonic could uncover new physics that have remained unexplored.

In this chapter, we demonstrate a new method of resonant intensity enhancement of a single harmonic just below the I_p , *i.e.*, the intensity enhancement for the single below-threshold harmonic (**BTH**) in LAPs, using tunable driving laser wavelengths. We show that this intensity enhancement is observed only for species in the LAP with a suitable dressed-AIS that overlaps with the Rydberg states. In our experiments, such conditions are achieved for species where the energy difference between the I_p and a suitable AIS are close to one or two photons of the driving laser, and when there is multiphoton resonance between the driving laser photon and I_p . We demonstrate that for In^+ ($I_p=18.87$ eV, odd-parity AIS (AIS^o) at 19.92 eV and even-parity AIS (AIS^e) at 20.04 eV) and Ga^+ ($I_p=20.52$ eV, AIS^e at 21.88 eV), the above conditions are met. Consequently, these species generate an intense single-BTH order when multiphoton resonance between the driving laser photon and I_p is achieved. On the other hand, for Sn^+ ($I_p=14.6$ eV) and Cr^+ ($I_p=16.5$ eV), we find no suitable AIS in the close vicinity of the I_p , and these species do not generate an intense single-BTH even for a multiphoton resonance between the driving laser photon and their I_p .

4.2 HHG from In^+ with Two-color 800+400 nm Laser Wavelength

Figure 4-1 shows the harmonic spectrum recorded from In^+ using a two-color HHG setup at the 800 nm driving field. This spectrum contains even as well as odd harmonics. In indium LAP, In^+ is the active species responsible for HHG. The I_p of In^+ is 18.87 eV, which is 12-photon resonant with the 800 nm driving laser wavelength. The odd-parity $4d^9 5s^2 5p$ (${}^2\text{D}$) ${}^1\text{P}_1$ AIS o exists at 19.92 eV above the ground state $4d^{10} 5s^2$ of In^+ . This radiative transition is very strong with a high gf value of 1.11, and is 13-photon resonant with an 800 nm driving field. As can be seen clearly in

Figure 4-1, there is an intensity enhancement at 13H as per the well-known four-step model. However, surprisingly, the 12H, which is the single-BTH harmonic order, also has intensity enhancement relative to the neighboring harmonics. The 12H is 24 times more intense than 8H, 10 times more intense than 11H and 7 times more intense than 14H and 15H.

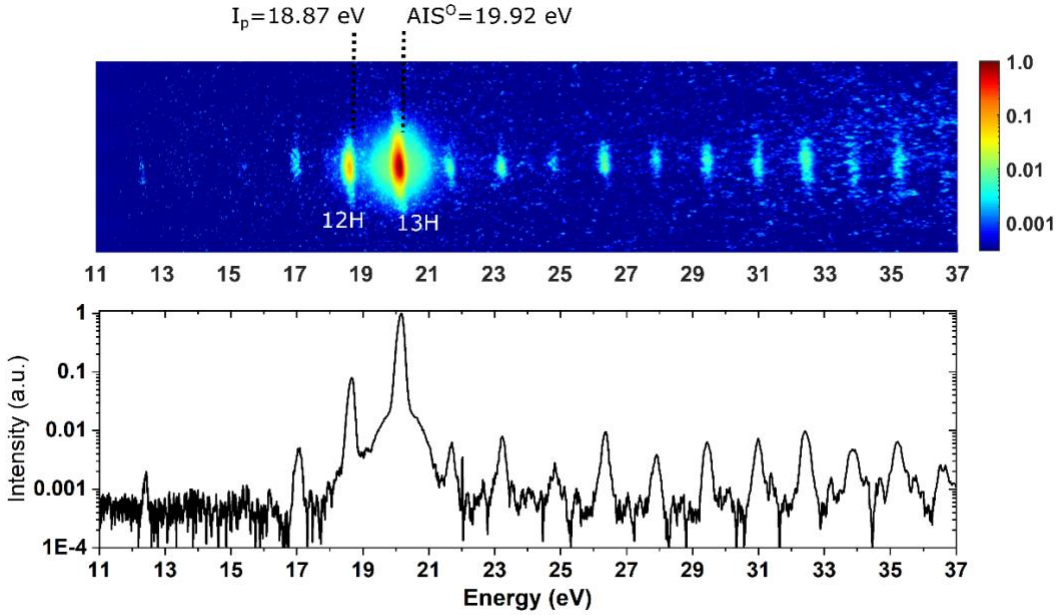


Figure 4-1 HHG spectrum generated from In^+ with two-color 800+400 nm laser.

4.3 HHG from In^+ with Tunable Mid-infrared Laser Wavelengths

In Figure 4-2(a), we show the HHG spectra from In^+ using driving pulses with a central wavelength at 1780 nm. The I_p of In^+ is 18.87 eV, which is 27-photon resonant with the 1780 nm driving laser wavelength. As can be seen, the 27th harmonic (27H), which is the single-BTH order, is generated with intensity enhancement relative to the neighbouring harmonics. With a shift in the driving laser wavelength away from the resonant 1780 nm, the 27H intensity decreases, as shown in Figure 4-2(b), indicating the resonant behavior of 27H.

4.4 HHG from In^+ with Tunable Near-infrared Laser Wavelengths

As RH intensity is known to be sensitive to the number of resonant laser photons [16], we reduced the multiphoton resonant order for I_p to 13-photon using 860 nm driving laser wavelength, further increasing the intensity of single-BTH. The corresponding HHG spectrum is shown in Figure 4-3(a). The 13H of In^+ is again generated with intensity enhancement relative to the neighbouring harmonics. We find that this response of single-BTH in In^+ is different from the resonance-

enhanced structures just below I_p reported in the previous studies with argon gas [24]·[25], where the BTH order has a similar intensity compared to the other neighbouring harmonics, and hence no intensity enhancement was observed. However, in the case of In^+ , the resonant single-BTH has significant intensity enhancement relative to the neighbouring harmonics, indicating a unique resonant enhancement phenomenon playing its role.

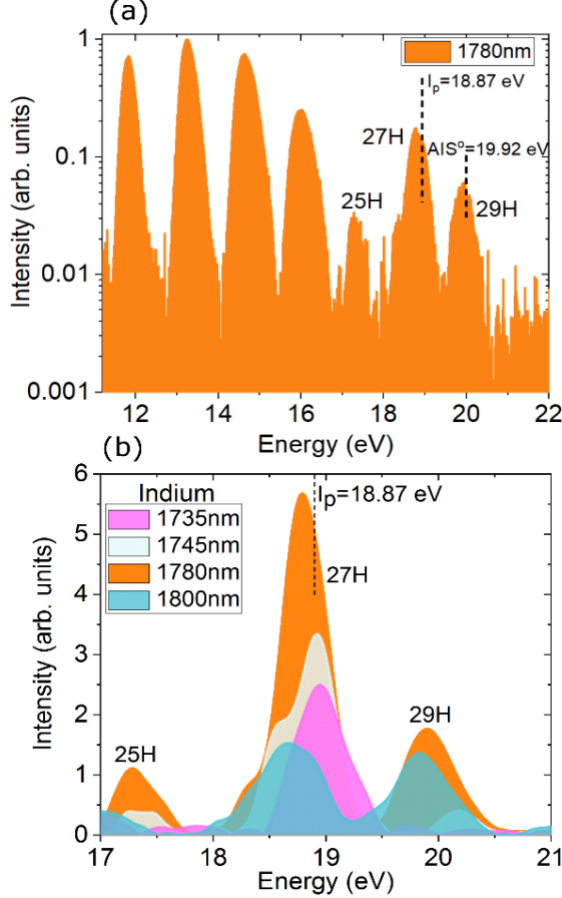


Figure 4-2 **(a)** High-order harmonic spectrum generated from In^+ using driving laser pulses centered at 1780 nm and driving laser intensity of $\sim 4.3 \times 10^{14} \text{ W cm}^{-2}$. The I_p of In^+ is 18.87 eV, which is 27-photon resonant with the 1780 nm driving laser photon, and the $4d^9 5s^2 5p$ (^2D) $^1\text{P}_1$ AIS° of In^+ is located at 19.92 eV. **(b)** The change in the 27H intensity when the driving laser wavelength is tuned away from the resonant 1780 nm laser wavelength.

In Figure 4-3(b), we show the HHG spectrum generated from In^+ using driving pulses with a central wavelength of 940 nm. The $4d^9 5s^2 5p$ (^2D) $^1\text{P}_1$ AIS° of In^+ at 19.92 eV is 15-photon resonant with the 940 nm driving laser wavelength [26]. This AIS° has an odd-parity, which is opposite to the parity of the $4d^{10} 5s^2$ $^1\text{S}_0$ ground state of In^+ , and hence allows a high oscillator strength one-photon radiative transition from the AIS° into the ground state [26]. The resonant 15H is generated

as per the well-known four-step model [14][15]. The first two steps of this model are the same as the three-step model, *i.e.*, TI and the acceleration of the ionized electron. In the third step, this electron is resonantly captured into the AIS (a discrete state embedded in the continuum), followed by the fourth step involving the radiative transition from the AIS into the initial ground state emitting the intense RH [14][15].

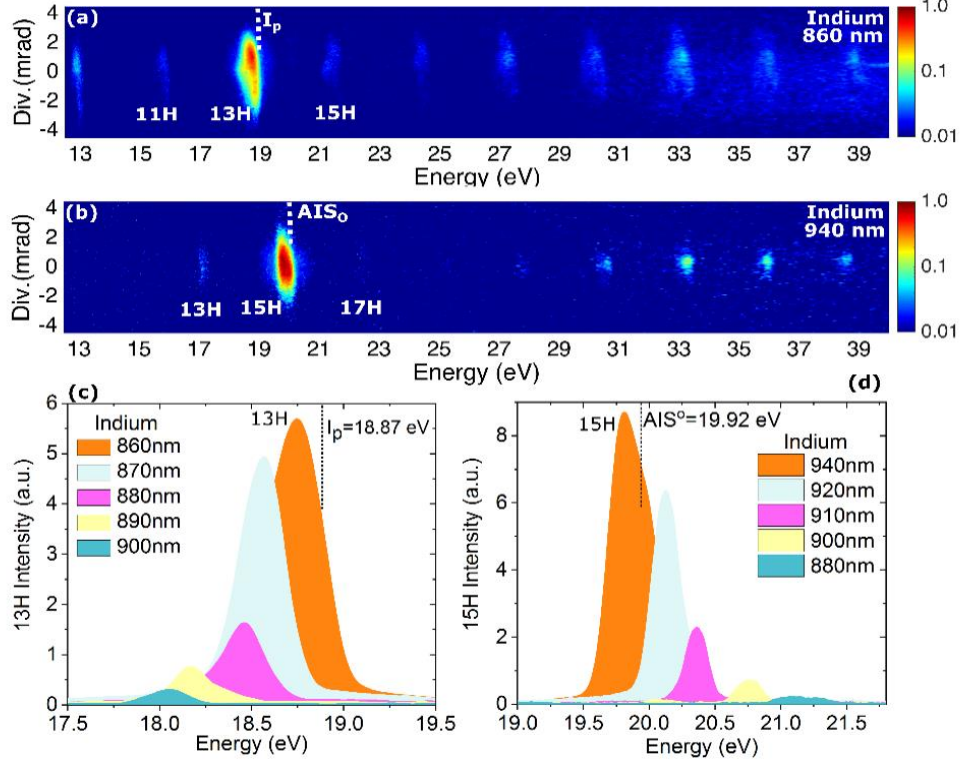


Figure 4-3 High-order harmonic spectrum generated from In⁺ **(a)** using driving laser pulses with a central wavelength of 860 nm and **(b)** using driving laser pulses with a central wavelength of 940 nm, both at a peak intensity of $\sim 1.5 \times 10^{14}$ W cm⁻². The I_p of In⁺ is 18.87 eV, which is 13-photon resonant with the 860 nm driving laser photon, and the 4d⁹5s²5p (²D) ¹P₁ AIS^o of In⁺ at 19.92 eV is 15-photon resonant with the 940 nm driving laser photon. **(c)** The change in the 13H intensity when the driving laser wavelength is tuned away from the resonant 860 nm laser wavelength. The peak intensity ER observed for the 13H is 18. **(d)** The change in the 15H intensity when the driving laser wavelength is tuned away from the resonant 940 nm laser wavelength. The peak intensity ER observed for the 15H is 38.

To better understand the behavior of the harmonic enhancement for the single-BTH, we tuned the driving laser wavelength as shown in Figure 4-3(c). Similar to our observations with 1780 nm driving laser wavelength as shown in Figure 4-3(b), we see that the 13H intensity decreases when

the driving laser wavelength is changed from the resonant 860 nm wavelength towards the non-resonant 900 nm. This decrease in the harmonic intensity is due to the shift in the 13H energy away from the resonance, *i.e.*, shift away from the I_p . With a change in driving laser wavelength towards resonance at 860 nm, the resonant peak intensity ER for the 13H is observed to be 18.

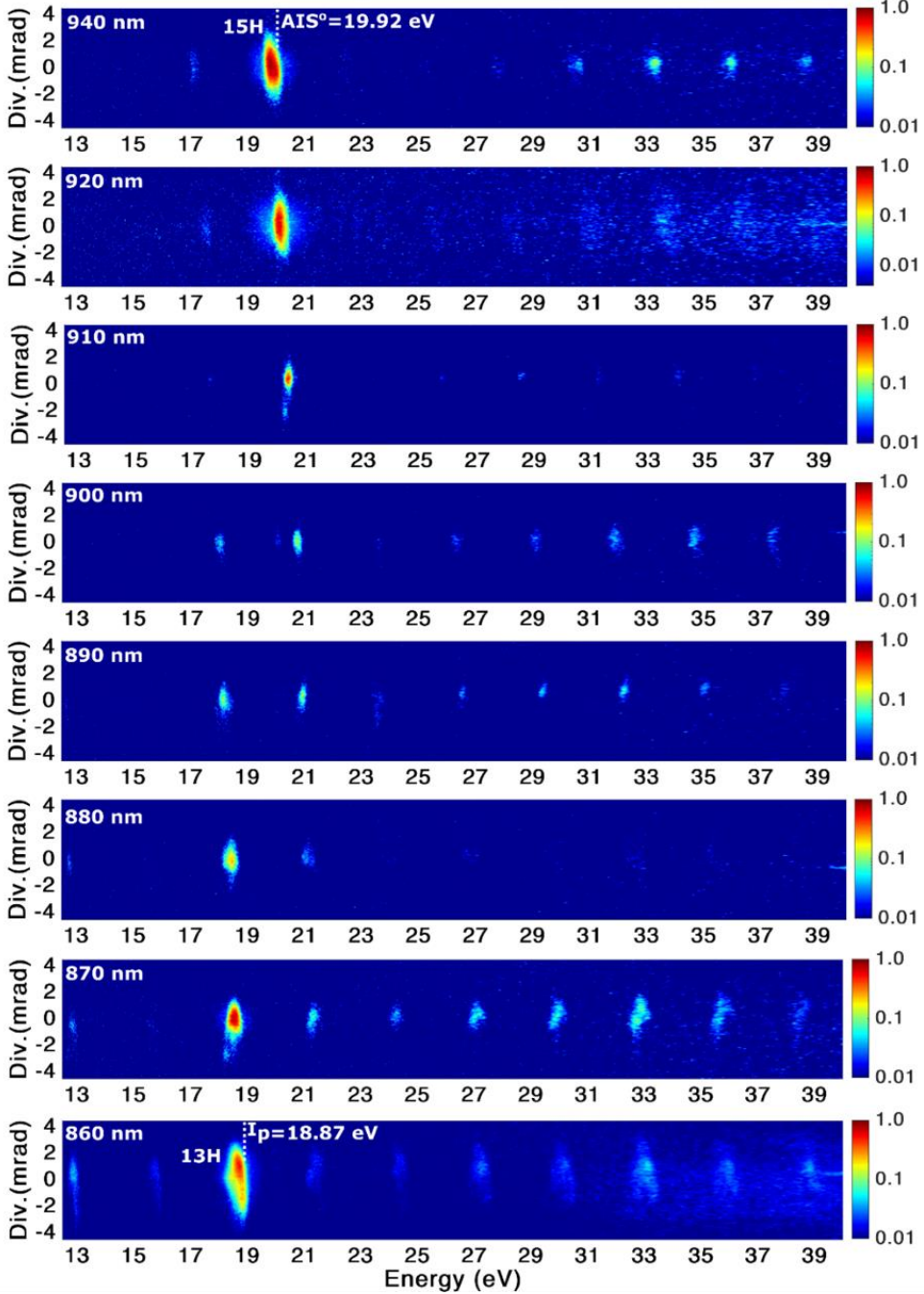


Figure 4-4 The various high-order harmonic spectra generated from In^+ using different driving laser wavelengths. The driving laser intensity used to generate each HHG spectrum is $\sim 1.5 \times 10^{14} \text{ W cm}^{-2}$.

Similarly, in Figure 4-3(d), we observe that when the driving laser wavelength is changed from the non-resonant 880 nm toward resonance at 940 nm wavelength with the $4d^95s^25p$ (2D) 1P_1 AIS^o at 19.92 eV, a resonant peak intensity ER of 38 is observed for the 15H. The reduction of the 15H intensity with a shift in the driving laser wavelength away from the resonance is due to the resonant nature of 15H generation, as per the four-step model [14][15]. This similarity of the behaviour of reduction in intensity between the 13H (which is the single-BTH) and 15H with a change in driving laser wavelength confirms the critical role of some phenomenon related to the multiphoton resonance with the driving laser photons in generating the single-BTH from In⁺, although its generation mechanisms should be different from the 15H.

4.5 HHG from Ga⁺, Sn⁺ and Cr⁺ with Tunable Near-infrared Laser Wavelengths

Apart from In⁺, another species with the I_p and an AIS located in close vicinity is Ga⁺. The I_p of Ga⁺ at 20.52 eV is located in the close vicinity of the $3d^{10}4p5p$ (1S) AIS^e at 21.88 eV. With the 800 nm driving laser photon, the I_p and $3d^{10}4p5p$ (1S) AIS^e of Ga⁺ is 13-photon and 14-photon resonant, respectively, achieving multiphoton resonance with the driving laser photon simultaneously. As shown in Figure 4-5(a), we see resonant intensity enhancement for 13H, which is the single-BTH in Ga⁺. This is similar to the single-BTH harmonic enhancement observed in In⁺, which confirms the importance of the presence of AIS and I_p in the close vicinity of each other in generating intense single-BTH.

To check if the RH enhancement for the single-BTH exists for every LAP when multiphoton resonance with the I_p is achieved, we used tin LAP as the nonlinear media for the HHG because there exists no suitable AIS in the close vicinity of I_p. In tin LAP, Sn⁺ responds as an active species for HHG and has I_p at 14.6 eV, which is 11-photon resonant with the 940 nm laser photon [12]. Figure 4-5(b) shows the harmonic spectrum from Sn⁺ that shows no harmonic enhancement near the I_p. The resonantly enhanced 19H observed using the 900 nm driving laser wavelength in Sn⁺ is generated as per the four-step model [14][15] involving the high oscillator strength 26.27 eV resonant transition from the $4d^95s^25p^2$ (1D) $^2D_{5/2}$ AIS^e into the ground state $4d^{10}5s^25p$ $^2P_{3/2}$ [12]. We also checked the response of single-BTH in Cr⁺ with I_p at 16.5 eV, which also has no suitable AIS in its close vicinity, and no harmonic enhancement was observed again near the I_p, as seen in Figure 4-6.

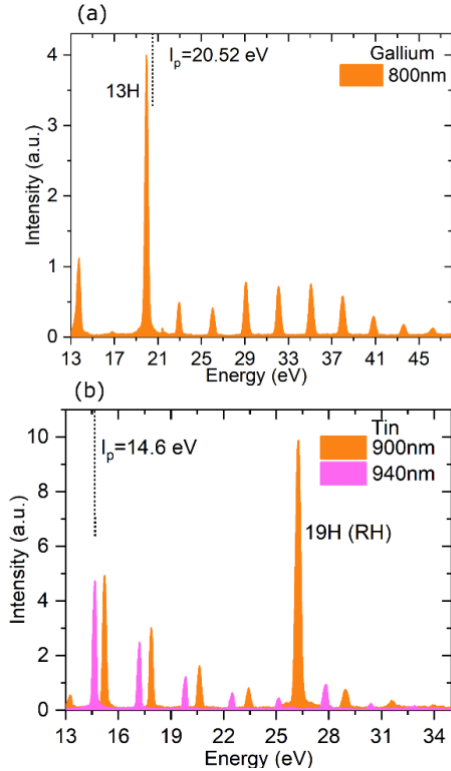


Figure 4-5 (a) The high-order harmonic spectrum generated from Ga^+ at 800 nm driving laser wavelength. (b) The high-order harmonic spectrum generated from Sn^+ at 900 nm and 940 nm driving laser wavelength.

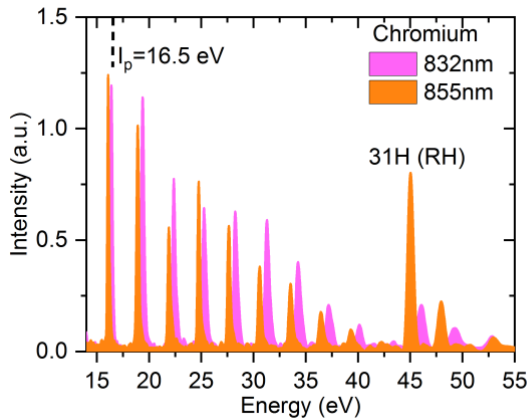


Figure 4-6 The high-order harmonic spectrum generated from Cr^+ at 855 nm and 832 nm driving laser wavelength.

4.6 Proposed Coupling Scheme of In^+

In our recent studies, as per the four-step model, we demonstrated that the path of a tunnel-ionized electron in the continuum could be perturbed by the dressed-AISs located symmetrically around

the AIS at energies $\pm 2\Omega$ (where Ω represents the driving laser photon energy) [16]. This results in coherent satellite harmonic emission near the AIS energy. To explain the mechanism of resonant single-BTH observed, we propose the coupling scheme for In^+ as depicted in Figure 4-7. For In^+ , using the broadband 1780 nm driving laser pulses with a bandwidth of ~ 90 nm FWHM, the multiphoton resonance condition with both the $4d^9 5s^2 5p$ (2D) 1P_1 AIS^o and the I_p is achieved simultaneously. The Rydberg cloud can be sufficiently populated through multiphoton resonant excitation with the driving laser photon [24][25]. The close vicinity of the presence of I_p to the AIS^o makes possible the overlap of two-photon below $| -2\Omega^o_{1780} \rangle$ dressed-AIS having odd-parity with the Rydberg cloud, as shown in Figure 4-7. The radiative one-photon transition from the odd-parity $| -2\Omega^o_{1780} \rangle$ dressed-AIS into the even-parity $4d^{10} 5s^2$ (1S_0) ground state is allowed. Therefore, the $| -2\Omega^o_{1780} \rangle$ dressed-AIS overlapped with the Rydberg cloud provides an efficient path for the population in the Rydberg cloud to undergo a one-photon radiative transition into the ground state emitting an intense single-BTH, which is 27H as shown in Figure 4-7.

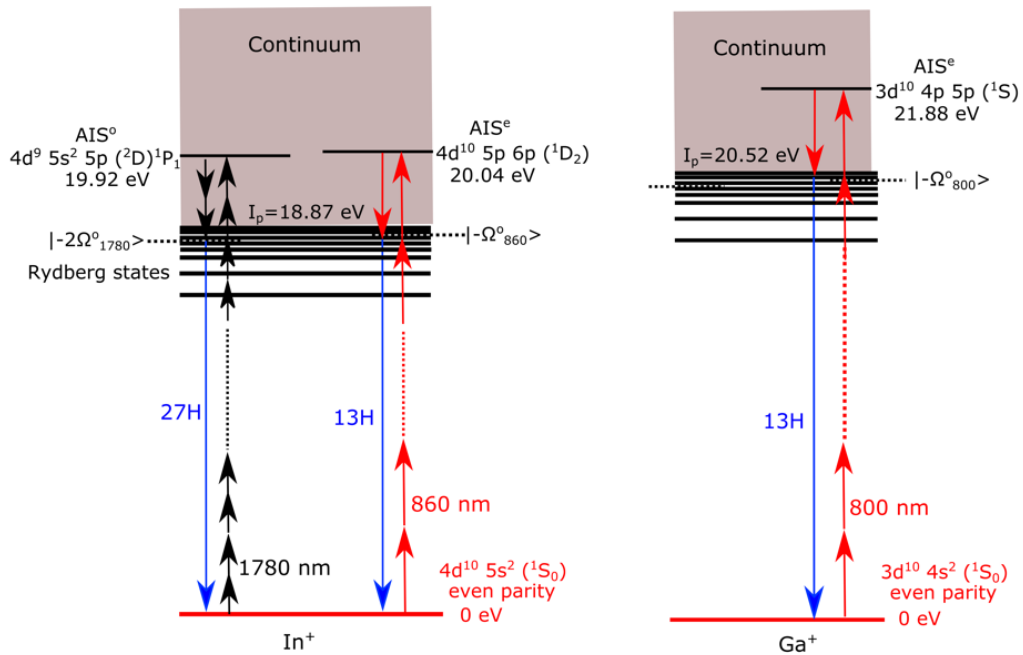


Figure 4-7 The proposed coupling scheme of In^+ (left) and Ga^+ (right) explaining the generation of an intense single-BTH.

Similarly, using the 860 nm driving laser wavelength with In^+ , the multiphoton resonance condition with both the $4d^{10} 5p$ $6p$ 1D_2 AIS^e located at 20.04 eV and the I_p at 18.87 eV is achieved

simultaneously, populating the Rydberg cloud through multiphoton resonant excitation. The one-photon below $|\Omega^0_{860}\rangle$ dressed-AIS overlapped with the Rydberg cloud again provides an efficient path for the electron population in the Rydberg cloud to undergo a one-photon radiative transition into the ground state emitting an intense 13H single-BTH in this case. A similar coupling scheme can explain the single-BTH from Ga^+ . The $3d^{10} 4s^2 \text{ }^1\text{S}_0$ ground state of Ga^+ has even-parity and the $3d^{10}4p5p \text{ }(^1\text{S})$ AIS^e at 21.88 eV is located in the close vicinity of I_p at 20.52 eV. The one-photon below dressed-AIS $|\Omega^0_{800}\rangle$ having an odd-parity is overlapped with the Rydberg cloud, again providing an efficient path for the electron population in the Rydberg cloud for one-photon radiative transition into the ground state to emit an intense single-BTH.

4.7 TDSE Calculations with a Model Two-electron Atom

We perform TDSE calculations with a model two-electron atom in a laser field. The model atom is one-dimensional, the electrons interact with the core and with each other via a soft-Coulomb potential, so the system can be denoted as “1-D helium”. The details of our model will be presented elsewhere [27]. However, similar systems are considered in references [28][29].

The system has AIS of odd and even parity. To find them, we calculate 1- and 2-photon ionization cross-sections: peaks in the 1-photon ionization cross-section show the odd-parity AIS energies, and peaks in the 2-photon ionization cross-section (as a function of the total energy of the two photons) show the energies of the even-parity ones. In particular, right above the ionization threshold (14.8 eV), there is an even-parity AIS with an energy of about 15.3 eV, see the calculated 2-photon ionization cross-section in Figure 4-8(a) and Figure 4-8(b). We also calculated the XUV spectra for 9H and 11H by varying the driving frequency in the vicinity of 10-phonon resonance with the AIS, and for H13 and H15 in the vicinity of 14-photon resonance with the AIS. We see that the even-parity AIS provides HHG enhancement when an even number of laser quanta is equal to the AIS energy or, in other words, the HHG is enhanced by the resonance with the even-parity AIS dressed by one laser photon. Thus, our calculations confirm the picture, suggested in Figure 4-7, where the single-BTH enhancement is attributed to the resonance with the dressed even-parity AIS. However, experimentally, the enhancement for the harmonic below the AIS is much more pronounced than for the harmonic above it, while in the calculations, both are enhanced to a comparable extent. Below we study this in more detail. In Figure 4-8(c) and Figure 4-8(d), we present the HHG intensity varying the driver wavelength in a wider range. We present both 1- and 2-photon ionization cross-sections (in arbitrary units). One can see that the 1-photon ionization

cross-section has several overlapping maxima for the photon frequency above approximately 15.5 eV. These maxima can be attributed to several odd-parity AIS and lead to HHG enhancement in this frequency range.

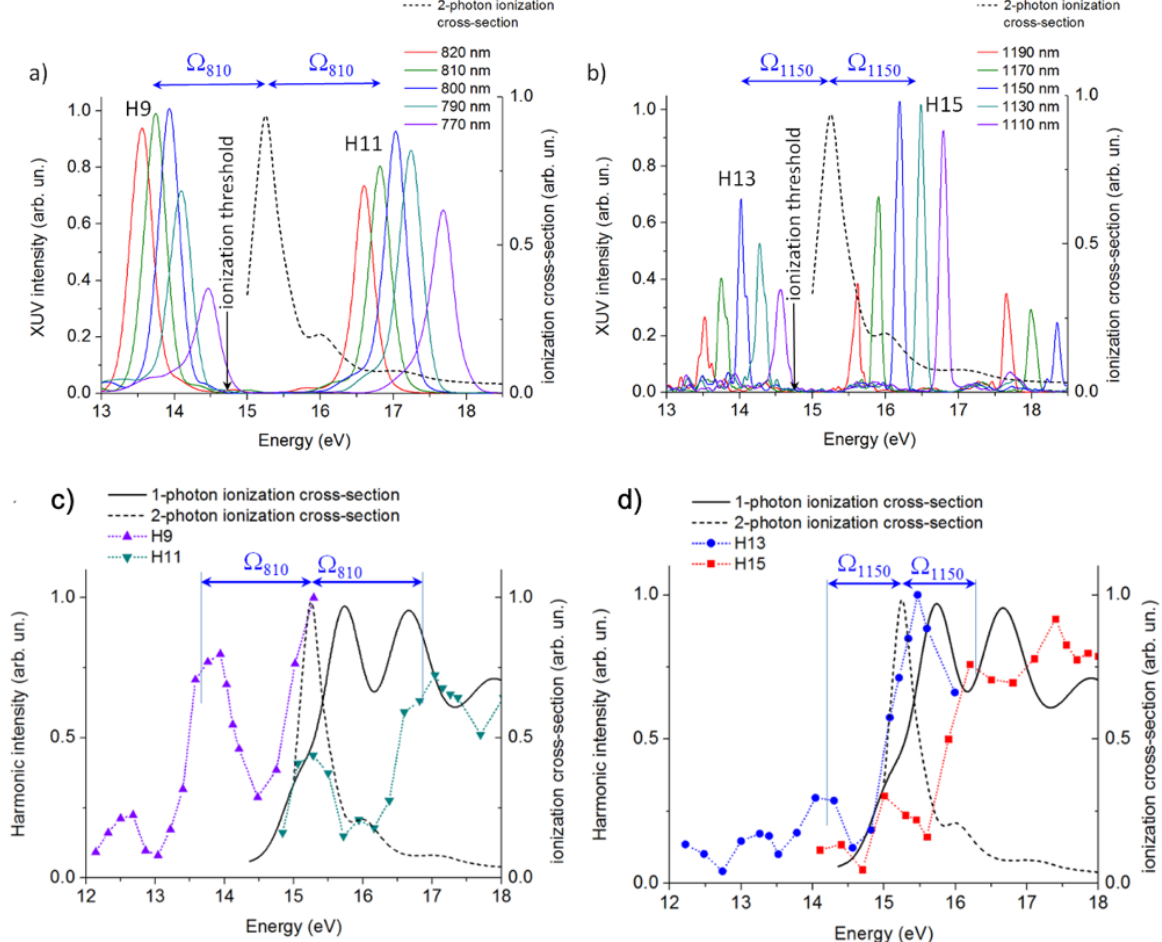


Figure 4-8 Calculated 2-photon ionization cross-section and spectra of (a) H9 and H11 in the vicinity 10-photon resonance, (b) H13 and H15 in the vicinity of 14-photon resonance with the even-parity AIS of a model two-electron atom. Similarly, the calculated 1- and 2-photon ionization cross-sections and intensities of (c) H9 and H11 near the 10-photon resonance (d) H13 and H15 near the 14-photon resonance with the even-parity AIS. The laser pulse duration and peak intensity for 810 nm and 1150 nm wavelength are 20 fs, $2.5 \times 10^{14} \text{ W/cm}^2$ and 50fs, $1 \times 10^{14} \text{ W/cm}^2$, respectively.

Note that the harmonic maxima do not exactly coincide with the maxima in the 1-photon ionization cross-section; the possible reason is the interference of the resonances from the odd-parity AIS and dressed even-parity AIS, as well as other features discussed in reference [30]. In general, in the conditions of Figure 4-8, the lower 9H and 13H orders are enhanced by double-resonance with

Rydberg states and dressed even-parity AIS, while the higher 11H and 15H orders are enhanced by resonances with odd-parity AIS and dressed even-parity AIS. This feature can explain the difference with experimentally observed spectra presented in Figure 4-3, because experimentally, there is no contribution of an odd-parity AIS in the enhancement of the higher harmonic. Moreover, our calculations show that the effect of odd- and even- parity AIS on the HHG enhancement can be comparable, in qualitative agreement with the experimental results (compare Figure 4-3(a) and Figure 4-3(b)).

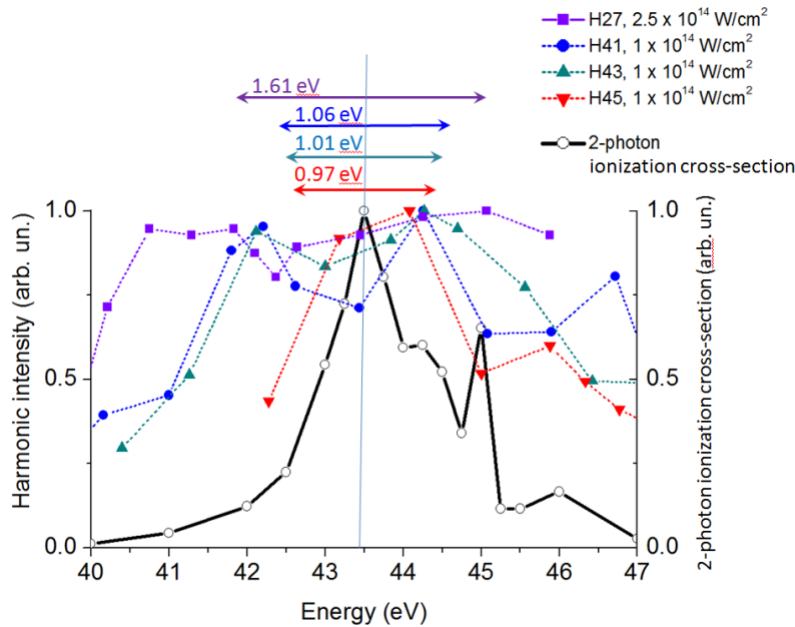


Figure 4-9 Calculated 2-photon ionization cross-section and intensities of harmonics H27, H41-45 near the resonances with dressed even-parity AI states in the vicinity of 43-45 eV. H27 is generated by the laser pulse with intensity $2.5 \times 10^{14} \text{ W/cm}^2$, driving frequency is tuned near 1.55 eV; H41-45 are generated by the laser pulse with intensity $1 \times 10^{14} \text{ W/cm}^2$, driving frequency is tuned near 1.0 eV. The pulse duration is 20 fs in all the calculations.

To also study the HHG enhancement with the dressed even-parity AIS without interference with the contribution from the odd-parity one, we calculated HHG enhancement for much higher XUV frequency, where the enhancement is produced by a group of even-parity AIS in the vicinity of 43.4 eV. We calculate the two-photon ionization cross-section for our model atom and find that the lowest peak in this cross-section is at approximately 43.4 eV; in close vicinity above this energy, there are three more peaks, see Figure 4-9. The overlapping peaks provide a band 43-45 eV where the 2-photon ionization cross-section is relatively high. Note that the one-photon ionization cross-section in this range decreases monotonously with the photon energy and thus has

no maxima. In Figure 4-9, we also show the 2-photon ionization cross-section and the harmonic intensity generated under different driving frequencies so that the harmonic frequency scans the resonance. We see that the HHG is enhanced in the vicinity of the band 43-45 eV. The width of the enhancement region is approximately defined by plus/minus one laser frequency, so it should be attributed to the resonance with the dark AISs dressed by one laser photon. HHG is enhanced in the region defined by the position of the AIS dressed by one laser photon, and that the harmonic intensity decreases both above and below this region.

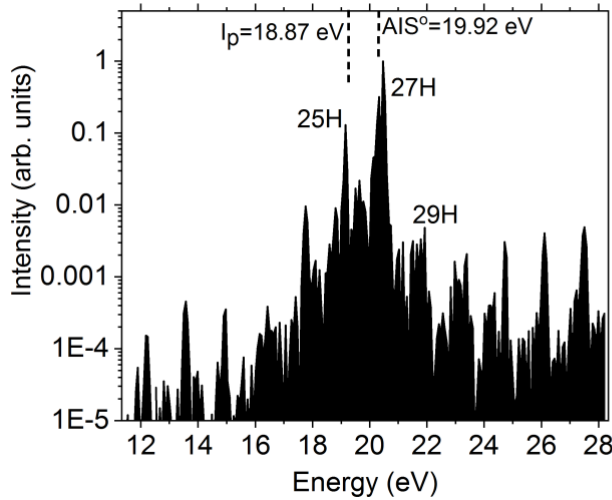


Figure 4-10 Calculated HHG spectrum from TDSE calculations with a model potential of In^+ reproducing the intensity enhancement from the $4d^9 5s^2 5p$ (^2D) $^1\text{P}_1$ AIS o at 19.92 eV with 1780 nm driving laser excitation. Intensity enhancement for the single-BTH (25H) is also observed. The laser intensity is $2 \times 10^{14} \text{ W/cm}^2$ with a pulse duration of 50 fs.

4.8 TDSE Calculations with Single-active Electron Model

To continue our investigations, we also simulated the HHG spectra from In^+ using the numerical TDSE calculations with single-active electron approximation; the role of the other electrons is partly reproduced with a model potential (see details in reference [31][32]). Our In^+ model potential has only one AIS, and the parity of this state is odd. It reproduces the AIS o transition $4d^9 5s^2 5p$ (^2D) $^1\text{P}_1 \rightarrow 4d^{10} 5s^2$ $^1\text{S}_0$ of energy 19.92 eV [26]. Therefore, the corresponding $| -2\Omega^o_{1780} \rangle$ dressed-AIS overlapped with the Rydberg cloud is included in our calculations, and the radiative one-photon transition from the $| -2\Omega^o_{1780} \rangle$ dressed-AIS into the even-parity $4d^{10} 5s^2$ $^1\text{S}_0$ ground state of In^+ is allowed.

As shown in Figure 4-10, the calculations reproduce the intensity enhancement observed near the AIS^o at 19.92 eV as per the four-step model. However, we also see intensity enhancement for the single-BTH, which is 25H with the 1780 nm laser, with an intensity enhancement ratio of one to two orders of magnitude relative to other non-resonant harmonic orders. This supports the observation of resonant intensity enhancement of single-BTH observed in our experimental investigations.

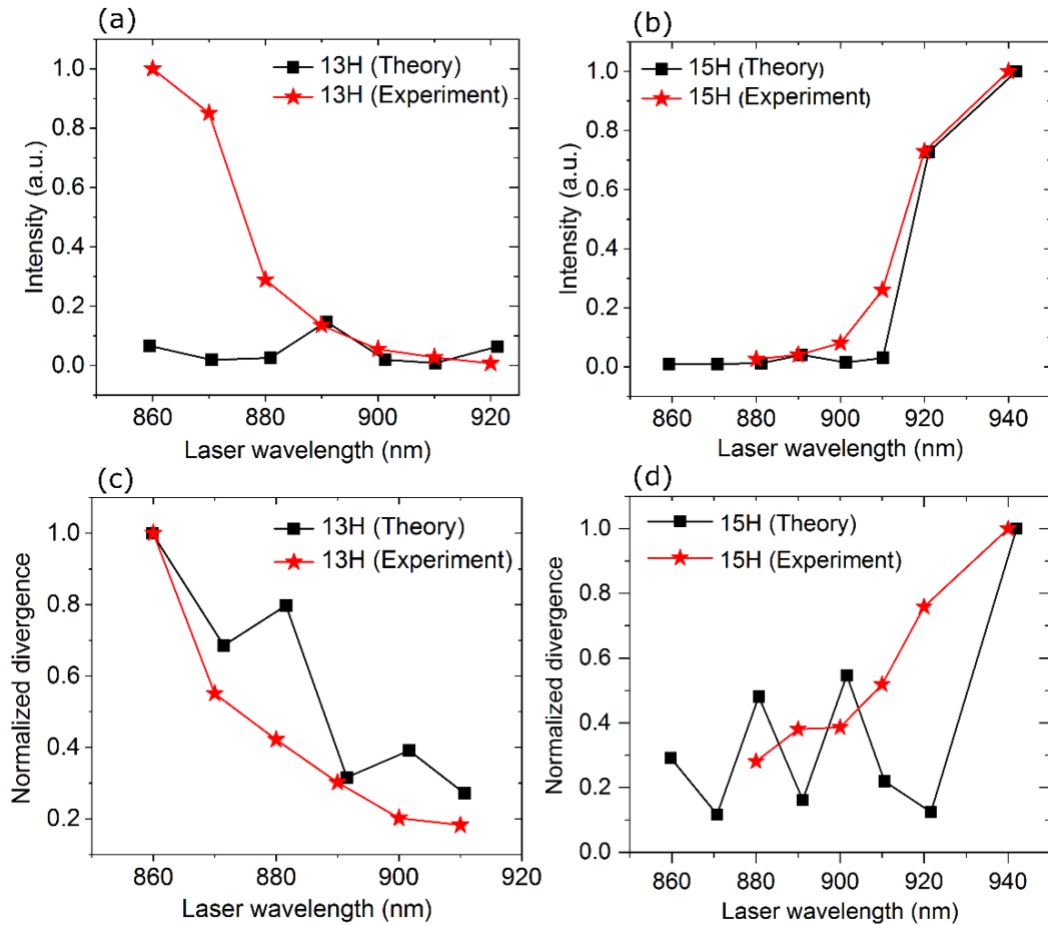


Figure 4-11 The calculated harmonic intensity and the harmonic divergence using the TDSE calculations with a model potential of In⁺ reproducing the 4d⁹5s²5p (²D) ¹P₁ AIS^o at 19.92 eV.

The TDSE calculations with the same model potential of In⁺, reproducing the 4d⁹5s²5p (²D) ¹P₁ AIS^o at 19.92 eV with 860 nm driving laser wavelength. However, in this case, one-photon below dressed-AIS, which overlaps with the Rydberg cloud, has even-parity. Therefore, the one-photon radiative transition from dressed-AIS into the ground state is not allowed. In this case, as shown

in Figure 4-11(a), no harmonic enhancement for the single-BTH (*i.e.*, for the 13H) was reproduced in the calculations. This shows that only by considering the Rydberg cloud present just below I_p without the overlap with a suitable dressed-AIS does not result in the intensity enhancement for the single-BTH. This observation agrees qualitatively with our experimental results of Sn^+ , where no suitable AIS is found to be present in the close vicinity of the I_p , consequently not resulting in an intensity enhancement for the single-BTH. However, the transition $4d^9 5s^2 5p\ (^2D)\ ^1P_1 \rightarrow 4d^{10} 5s^2\ ^1S_0$ at 19.92 eV included in the calculations reproduces very well the harmonic enhancement of 15H with its generation mechanism as per the four-step model, as seen in Figure 4-11(b). The change in the harmonic divergence is very well reproduced, as shown in Figure 4-11(c) and Figure 4-11(d). The experimentally observed $1/e^2$ harmonic divergence of 13H and 15H at 860 nm and 940 nm driving laser wavelength is 5.46 mrad and 5.36 mrad, respectively.

4.9 Energy Levels of In^+ and Ga^+

Table 4-1 Even autoionizing states of In^+ in the excitation energy range from ionization energy 18.87 eV to 20.7 eV. The leading configuration is $4d^{10}5p6p$. The excitation energy presented in the table is the energy difference between the autoionizing state and the ground state.

	<i>LS composition (shown >1%)</i>	<i>Electron energy, eV</i>	<i>Excitation energy, eV</i>	Γ, meV
${}^3D({}^1P)_1$	48.6% 3D + 47.0% 1P + 1.6% 3S	0.24	19.11	27
${}^3D({}^1P)_1$	38.4% 3D + 32.5% 1P + 20.1% 3P + 6.2% 3S	0.45	19.32	17
3D_2	84.9% 3D + 7.2% 3P + 3.7% 1D	0.48	19.35	80
3P_0	94.2% 3P + 3.0% 1S	0.57	19.44	1.9
3P_1	67.0% 3P + 16.5% 1P + 9.5% 3P	0.73	19.60	5.2
3D_3	96.5% 3D	0.75	19.62	49
3P_2	80.8% 3P + 10.0% 3D + 6.0% 1D	0.86	19.73	46
3S_1	84.2% 3S + 10.2% 3P + 2.4% 1P	1.01	19.88	3.6
1D_2	79.6% 1D + 9.3% 3P + 1.4% 3D + 1.3% ${}^5p^2$ 1D + 1.0% ${}^5d6s\ {}^1D$	1.17	20.04	490
1S_0	79.3% 1S + 3.2% 3P + 8.2% ${}^5p7p\ {}^1S$ + 2.6% ${}^5p^2\ {}^1S$ + 1.5% ${}^5p8p\ {}^1S$ + 1.0% ${}^5s6s\ {}^1S$	1.79	20.66	14

Table 4-2 HF calculations for the Ga^+ ion level energies.

Configuration	Term	J	NIST (eV)	HF (eV)
$3d^{10}4s^2$	1S	0	0	0
$4s4p$	$^3P^\circ$	0	5.87283	
		1	5.92819	5.24
		2	6.04421	
$4s4p$	$^1P^\circ$	1	8.76586	9.02
$4s5s$	3S	1	12.7635	11.94
$4s5s$	1S	0	13.2244	11.95
$4p^2$	1D	2	13.3557	14.32
$4s5p$	$^3P^\circ$	0	14.6834	
		1	14.6944	13.66
		2	14.7204	
$4s5p$	$^1P^\circ$	1	14.9463	14.19
$4s6s$	3S	1	16.4912	15.45
$4s6s$	1S	0	16.5818	15.44
$4p^2$	1S	0	16.8171	15.84
Ga III ($3d^{10}4s$)	2S	1/2	20.51514	19.35
$3d^94s^24p$	$^3P^\circ$	1	20.975	20.52
$3d^94s^24p$	$^1P^\circ$	1	21.88	21.48
$3d^{10}4p5p$	1D	2		21.07
$3d^{10}4p5p$	1S	0		21.40
$3d^94s^25p$	$(^5/2, ^3/2)^\circ$	1	30.662	
$3d^94s^25p$	$(^3/2, ^3/2)^\circ$	1	31.058	30.09
$3d^94s^25p$	$(^3/2, ^1/2)^\circ$	1	31.115	30.25

All levels (except shaded grey) and the ionization energy are shifted down with respect to NIST database energies. The calculated even-parity AIS $3d^{10}4p5p\ ^1S$ of Ga^+ (shaded pink) is close to the

line shaded green at 21.88 eV, and can be in 14-photon resonant with the 800 nm central wavelength.

4.10 Summary of the Chapter

To summarize, we studied the response of the harmonic order just below the I_p from a range of solid targets, including indium, gallium, tin and chromium. We demonstrate a new method to generate intense resonant single harmonic at an energy just below the I_p in In^+ and Ga^+ . However, no such harmonic enhancement is observed in Sn^+ and Cr^+ . It is revealed that this kind of RH is observed because of the overlap of the dressed-AIS with the Rydberg cloud. We proposed a coupling scheme showing the possibility of single-BTH enhancement due to the overlap of a suitable dressed-AIS with the Rydberg cloud. The experimental results are partly reproduced with the model two-electron atom, as well as by TDSE calculations with model potential for In^+ . This new method to generate intense single harmonic is useful to generate bright coherent XUV light from atomic and molecular states that usually do not participate in intense harmonic emission, such as Rydberg states. It also provides a new mechanism to expand our current understanding of the RH generation phenomenon and to study the dynamics of AISs at the femtosecond timescale.

4.11 References

1. I. P. Christov, M. M. Murnane, and H. C. Kapteyn, "High-harmonic generation of attosecond pulses in the ‘single-cycle’ regime," *Physical Review Letters* **78**, 1251–1254 (1997).
2. J. Li, X. Ren, Y. Yin, K. Zhao, A. Chew, Y. Cheng, E. Cunningham, Y. Wang, S. Hu, Y. Wu, M. Chini, and Z. Chang, "53-attosecond X-ray pulses reach the carbon K-edge," *Nature Communications* **8**, 186 (2017).
3. P. M. Paul, E. S. Toma, P. Breger, G. Mullot, F. Augé, P. Balcou, H. G. Muller, and P. Agostini, "Observation of a train of attosecond pulses from high harmonic generation," *Science* **292**, 1689–1692 (2001).
4. R. A. Ganeev, T. Witting, C. Hutchison, F. Frank, M. Tudorovskaya, M. Lein, W. A. Okell, A. Zaïr, J. P. Marangos, and J. W. G. Tisch, "Isolated sub-fs XUV pulse generation in Mn plasma ablation," *Optics Express* **20**, 25239 (2012).
5. C. Winterfeldt, C. Spielmann, and G. Gerber, "**Colloquium** : Optimal control of high-harmonic generation," *Reviews of Modern Physics* **80**, 117–140 (2008).
6. R. A. Ganeev, "High-order harmonic generation in a laser plasma: a review of recent achievements," *Journal of Physics B* **40**, R213–R253 (2007).
7. G. S. Boltaev, R. A. Ganeev, V. v. Kim, N. A. Abbasi, M. Iqbal, and A. S. Alnaser, "High-order harmonics generation in the plasmas produced on different rotating targets during ablation using 1 kHz and 100 kHz lasers," *Optics Express* **28**, 18859 (2020).
8. P. B. Corkum, "Plasma perspective on strong field multiphoton ionization," *Physical Review Letters* **71**, 1994–1997 (1993).
9. A. D. Shiner, B. E. Schmidt, C. Trallero-Herrero, H. J. Wörner, S. Patchkovskii, P. B. Corkum, J.-C. Kieffer, F. Légaré, and D. M. Villeneuve, "Probing collective multi-electron dynamics in xenon with high-harmonic spectroscopy," *Nature Physics* **7**, 464–467 (2011).
10. M. A. Fareed, V. V. Strelkov, M. Singh, N. Thiré, S. Mondal, B. E. Schmidt, F. Légaré, and T. Ozaki, "Harmonic Generation from Neutral Manganese Atoms in the Vicinity of the Giant Autoionization Resonance," *Physical Review Letters* **121**, 023201 (2018).
11. M. Singh, M. A. Fareed, A. Laramée, E. Isgandarov, and T. Ozaki, "Intense vortex high-order harmonics generated from laser-ablated plume," *Applied Physics Letters* **115**, 231105 (2019).

12. M. Suzuki, M. Baba, R. Ganeev, H. Kuroda, and T. Ozaki, "Anomalous enhancement of a single high-order harmonic by using a laser-ablation tin plume at 47 nm," *Optics Letters* **31**, 3306 (2006).
13. R. A. Ganeev, M. Suzuki, M. Baba, H. Kuroda, and T. Ozaki, "Strong resonance enhancement of a single harmonic generated in the extreme ultraviolet range," *Optics Letters* **31**, 1699 (2006).
14. V. Strelkov, "Role of autoionizing state in resonant high-order harmonic generation and attosecond pulse production.," *Physical review letters* **104**, 123901 (2010).
15. V. V. Strelkov, M. A. Khokhlova, and N. Y. Shubin, "High-order harmonic generation and Fano resonances," *Physical Review A* **89**, (2014).
16. M. A. Fareed, V. V. Strelkov, N. Thiré, S. Mondal, B. E. Schmidt, F. Légaré, and T. Ozaki, "High-order harmonic generation from the dressed autoionizing states," *Nature Communications* **8**, 16061 (2017).
17. N. H. Burnett, C. Kan, and P. B. Corkum, "Ellipticity and polarization effects in harmonic generation in ionizing neon," *Physical Review A* **51**, R3418–R3421 (1995).
18. M. Kakehata, H. Takada, H. Yumoto, and K. Miyazaki, "Anomalous ellipticity dependence of high-order harmonic generation," *Physical Review A* **55**, R861–R864 (1997).
19. D. C. Yost, T. R. Schibli, J. Ye, J. L. Tate, J. Hostetter, M. B. Gaarde, and K. J. Schafer, "Vacuum-ultraviolet frequency combs from below-threshold harmonics," *Nature Physics* **5**, 815–820 (2009).
20. E. P. Power, A. M. March, F. Catoire, E. Sistrunk, K. Krushelnick, P. Agostini, and L. F. Dimauro, "XFROG phase measurement of threshold harmonics in a Keldysh-scaled system," *Nature Photonics* **4**, 352–356 (2010).
21. M. Y. Ivanov, T. Brabec, and N. Burnett, "Coulomb corrections and polarization effects in high-intensity high-harmonic emission," *Physical Review A* **54**, 742–745 (1996).
22. P. C. Li, Y. L. Sheu, C. Laughlin, and S. I. Chu, "Dynamical origin of near- and below-threshold harmonic generation of Cs in an intense mid-infrared laser field," *Nature Communications* **6**, 1–7 (2015).
23. W.-H. Xiong, L.-Y. Peng, and Q. Gong, "Recent progress of below-threshold harmonic generation," *Journal of Physics B* **50**, 032001 (2017).
24. M. Chini, X. Wang, Y. Cheng, H. Wang, Y. Wu, E. Cunningham, P.-C. Li, J. Heslar, D. A. Telnov, S.-I. Chu, and Z. Chang, "Coherent phase-matched VUV generation by field-controlled bound states," *Nature Photonics* **8**, 437 (2014).
25. S. Beaulieu, S. Camp, D. Descamps, A. Comby, V. Wanier, S. Petit, F. Légaré, K. J. Schafer, M. B. Gaarde, F. Catoire, and Y. Mairesse, "Role of Excited States In High-order Harmonic Generation," *Physical Review Letters* **117**, 203001 (2016).
26. G. Duffy and P. Dunne, "The photoabsorption spectrum of an indium laser produced plasma," *Journal of Physics B* **34**, L173–L178 (2001).
27. V. A. Birulia and V. V. Strelkov, "paper in preparation,"
28. S. Bauch, L. K. Sørensen, and L. B. Madsen, "Time-dependent generalized-active-space configuration-interaction approach to photoionization dynamics of atoms and molecules," *Physical Review A* **90**, 062508 (2014).
29. V. v. Skobelev, "On the Energy of a ‘‘Two-Dimensional’’ Two-Electron Atom," *Journal of Experimental and Theoretical Physics* **2017** 125:6 **125**, 1058–1064 (2018).
30. V. v. Strelkov, M. A. Khokhlova, and N. Y. Shubin, "High-order harmonic generation and Fano resonances," *Physical Review A* **89**, 053833 (2014).
31. R. A. Ganeev, T. Witting, C. Hutchison, V. v. Strelkov, F. Frank, M. Castillejo, I. Lopez-Quintas, Z. Abdelrahman, J. W. G. Tisch, and J. P. Marangos, "Comparative studies of resonance enhancement of harmonic radiation in indium plasma using multicycle and few-cycle pulses," *Physical Review A* **88**, 033838 (2013).
32. Z. Abdelrahman, M. A. Khokhlova, D. J. Walke, T. Witting, A. Zair, V. v. Strelkov, J. P. Marangos, and J. W. G. Tisch, "Chirp-control of resonant high-order harmonic generation in indium ablation plumes driven by intense few-cycle laser pulses," *Optics Express* **26**, 15745 (2018).

Chapter 5

Resonant High-order Harmonic Generation from Neutral Manganese Atoms

5.1 Introduction

In HHG from LAP, and as already explained in chapter 2 of this thesis, the nonlinear media is produced from a solid target [1]. As such, it has the advantage of being able to generate harmonics from any material in solid form, thus widening the choice for studying their ultrafast dynamics through high-order harmonic spectroscopy. Moreover, many laser-ablated media used for harmonic generation contain different types of resonances [2,3], which perturb the harmonic spectra in the vicinity of the resonance involved. Therefore, HHG from LAP also allows studying the dynamics of such resonances via high-order harmonic spectroscopy [4]. However, high-order harmonics from LAP mostly have significant contributions from ionic species [5]. As it will be evident from the discussions in the upcoming sections, the neutral species in the LAP render any significant contribution toward the HHG. This happens because of their complete ionization much before the laser peak intensity, because of their low I_p , as explained later. Although harmonics from ions have the advantage of a large harmonic cut-off, because of their high I_p (as per the equation $\hbar\Omega_{max} = I_p + 3.17U_p$), one disadvantage is that we cannot study the ultrafast dynamics of materials in the stable phase, such as for free neutral atoms or those bound in a molecule or solid. In an attempt to solve this critical issue, we study the HHG from manganese LAP using both multicycle as well as the few-cycle mid-infrared ($\sim 1.8 \mu m$) driving laser pulses. We find that high harmonics are generated from neutral manganese, which has a low ionization potential of 7.4 eV. This is made possible with the use of very short, almost two-cycle laser pulses at $1.8 \mu m$ laser wavelength. See the following sections for a more detailed explanation. Moreover, manganese contains GAR at energies of around 50 eV. We observe intense and broadband high harmonics from the GAR at energies ranging from 49 to 53 eV. Our observation of high harmonics from neutral manganese opens a perspective to advance the laser-ablation technique for the ultrafast and attosecond study of neutral atoms.

5.2 Resonant Harmonic Generation from Giant Autoionizing Resonance

There have been growing interests from the scientific community to study the ultrafast dynamics of transition metal atoms [6]. An important probe to such studies could be the presence of a GAR in the PICS of transition metal atoms due to the inner-shell electron resonances. These resonances

mainly occur due to the 3p-3d transitions that have large PICS. For example, the photoabsorption spectroscopy data shows that manganese contains a strong resonance around \sim 51 eV. Figure 5-1 shows the photoabsorption spectra of Mn and Mn^+ , reported by Dolmatov *et al.* [6]. These spectra indicate that the PICS of both Mn and Mn^+ is high at \sim 51 eV. In the photoabsorption spectrum of Mn^+ , there exist some additional peaks at energies around 50 eV that are due to the 3p-4s transitions of Mn^+ .

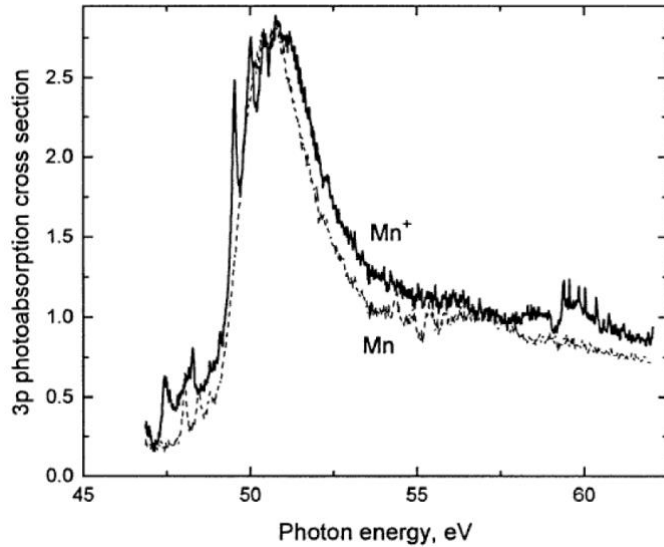


Figure 5-1 Photoabsorption spectra of neutral Mn and Mn^+ showing the photoabsorption cross-section [6].

Giant resonances are broadband in nature, which can be used for multiple studies. These include the generation of intense and broadband high-order harmonics, the study of their multi-electron dynamics, estimate the PICS of elements [7–12], and understand the conduction properties in the solid phase. Studying the ultrafast dynamics of GAR could also reveal new and important phenomena that are rich in physics. For example, in 2011, Shiner *et al.* demonstrated intense RH from the giant resonance of xenon around 100 eV [12], which was earlier predicted by Frolov *et al.* [13]. It was proposed that the RH peak at 100 eV is observable due to the strong Coulomb interaction between the continuum electron (tunnel ionized from the 5p state) and inner-shell 4d electron (lying in orbital $m=0$). Later, Pabst *et al.* [7] showed theoretically that in HHG from the giant resonance of xenon, all electrons from the 4d orbitals ($m=0, \pm 1, \pm 2$) contribute to broadband RH emission. Recently, Faccialà *et al.* [14] studied the dynamics of xenon harmonics with two-color multi-cycle laser fields, and demonstrated that the harmonic cut-off from xenon could be extended up to 85 eV, due to the involvement of multiple electrons in HHG. Contrary to the multi-

electron picture, Zhang and Gao [15] proposed that the enhancement in xenon harmonics around 100 eV can be explained with a single atom response. Since both Mn as well as Mn^+ contain a GAR close to ~ 51 eV, therefore it is of considerable importance to find conditions for harmonic generation from neutral manganese and study the dynamics of its giant autoionization resonance (GAR). The investigations of HHG from GAR of neutral Mn could reveal the unknown physics from such broadband resonance and would also extend the scope of the technique of HHG from LAP.

5.3 Significance of Laser Pulse Duration

When the solid manganese target atom is ablated, the resulting LAP would contain both neutral as well as the ionic species. To understand the underlying laser-matter interaction, it is important to discuss the significance of laser pulse duration. A typical driving laser pulse has a Gaussian temporal profile. This means that the driving laser intensity starts from zero and gradually increases up to the peak intensity, and then decreases to the minimum zero intensity, with the overall intensity profile in the form of a Gaussian function. If we compare the response of neutral atoms with the singly charged ions, the complete ionization for the neutral atoms occurs at lower intensity valued as compared to the single charged species. The laser intensity at which the complete ionization of a given species takes place is known as the saturation laser intensity. This saturation intensity could be much lesser than the peak laser intensity. Since the I_p of ionic species is higher than the neutral atoms, the saturation intensity of the neutral atoms is generally lower than the ionic species. Therefore, once the laser intensity reaches the saturation level within the temporal profile of the laser pulse, and because of the complete ionization of a given species, only the laser intensity up to the saturation intensity will significantly participate in the laser-matter interaction. One important implication of this is on the harmonic cut-off observed in the HHG experiments. As per the three-step model, the harmonic cut-off is given by the equation $E_c = I_p + 9.33 \times 10^4 I \lambda^2$. Therefore, if the saturation intensity for a given species in the LAP is I_s , the laser intensity I in the cut-off equation needs to be replaced with I_s , i.e., $E_c[eV] = I_p[eV] + 29.61 \times I_s[10^{14} W/cm^2] \times \lambda^2[\mu m]$. Therefore, even though the peak laser intensity could be much higher, the low value of I_s limits the maximum cut-off seen in the HHG experiments.

To emphasize the importance of laser pulse duration, the ionization yield in hydrogen atoms as a function of peak electric field of the driving laser pulse for different laser pulse durations is shown in Figure 5-2. The ionization yield with value 1.0 signifies a complete ionization. From the figure,

one can clearly see that with the reduction in the driving laser pulse duration, the atoms can survive up to higher values of laser electric field (and hence the higher laser intensity) before getting completely ionized. In other words, the saturation intensity I_s for a given species in the LAP can be increased by using shorter driving laser pulse durations.

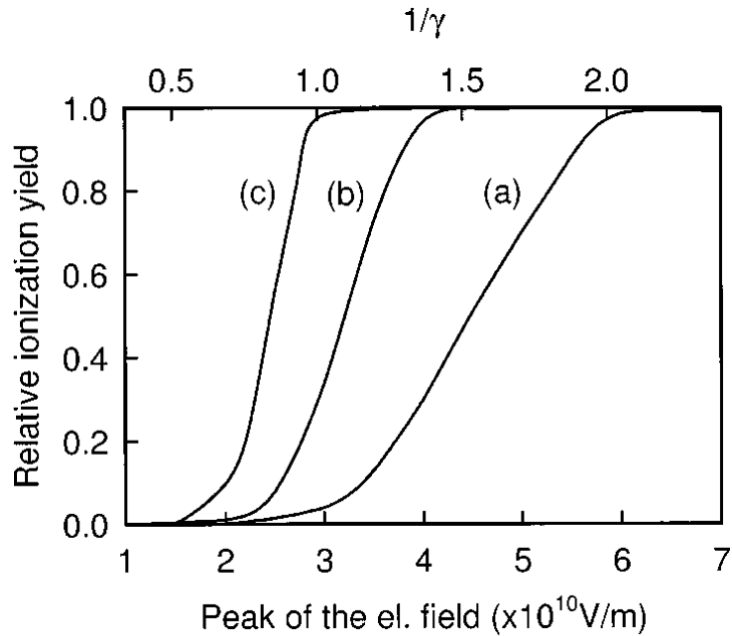


Figure 5-2 The ionization yield in hydrogen atom vs peak electric field strength for laser pulses of durations of (a) 10 fs, (b) 100 fs, and (c) 1000 fs with a laser wavelength of 800 nm [16].

5.4 Experimental Results and Discussion

Both neutral Mn and Mn^+ contain GAR around 50 eV, which is mainly due to the 3p-3d dipole transitions [10]. The role of this GAR in HHG is investigated by varying the pulse duration of the driving field, from 50 fs to 12 fs. Figure 5-3 shows the harmonic spectra recorded using driving fields with pulse durations of 50 fs (black spectrum, driving laser intensity $\sim 5 \times 10^{14} W/cm^2$) and 30 fs (blue spectrum, driving laser intensity $\sim 4.0 \times 10^{14} W/cm^2$). In this spectrum, despite the relatively higher driving laser intensity, high-order harmonics of up to only 36 eV are observed for the 50 fs driving field. This is in sharp contrast to the harmonic spectra recorded with 30 fs and 12 fs driving fields. From the high-order harmonic cut-off, we can find the laser-ablated species responsible for HHG. The high-order harmonic cut-off can be estimated with the semi-classical three-step model $E_{\text{cut-off}} = I_p + 3.17U_p = I_p [eV] + 29.61 \times I_L [10^{14} W/cm^2] \times \lambda^2 [\mu m]$. (where I_p , U_p , I and λ are the ionization potential, ponderomotive energy, driving laser intensity and wavelength, respectively). Calculations for $\lambda = 1.8 \mu m$ show that high-order harmonics with 50 fs

driving field are generated from neutral manganese. However, harmonics from GAR are not generated with the mid-IR multi-cycle driving field (further details are given in the numerical methods).

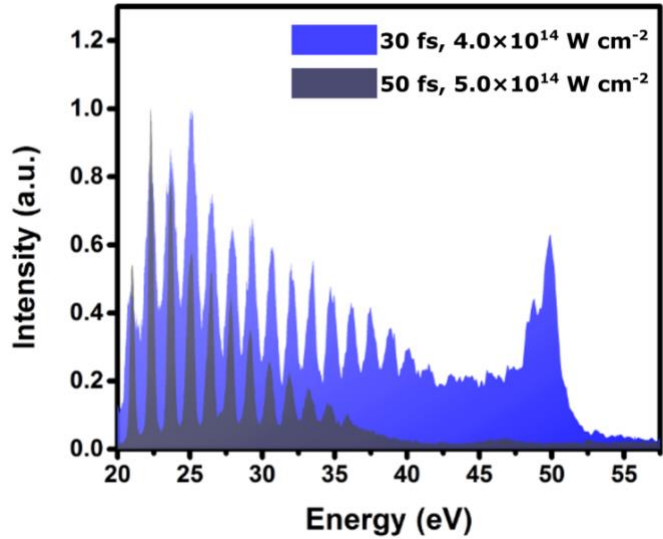


Figure 5-3 Harmonic spectra observed from laser-ablated manganese plume using driving lasers with pulse durations of ~30 fs (blue spectrum) and 50 fs (black spectrum), a wavelength of 1.82 μm , and laser intensities of $\sim 4.0 \times 10^{14} \text{ W cm}^{-2}$ and $\sim 5 \times 10^{14} \text{ W cm}^{-2}$, respectively. It has been revealed that with the 50 fs driving field, high-order harmonics are generated from neutral manganese. However, harmonics from the GAR of neutral manganese are not observed with the 50 fs driving field. The harmonics from GAR appear for the driving field with a pulse duration of 30 fs.

For high-order harmonics from laser-ablated manganese plume, we find a difference in the cut-off when multi-cycle near-IR ($0.8 \mu\text{m}$; energy ~ 8 to 25 mJ) [3] and mid-IR ($1.8 \mu\text{m}$; energy ~ 1 to 5 mJ) driving fields are used. With a near-IR driving field, high-order harmonics up to 156 eV have been observed [3,17], whereas with the mid-IR laser, even at similar driving field intensities, the harmonic cut-off has been observed to be low (36 eV). This difference can be explained by the fact that with near-IR driving fields, high-order harmonics are mostly generated from ionic species [3]. Alternatively, our observation of HHG from neutral manganese shows that with a longer, mid-IR driving field, we could extend high-order harmonic studies for laser-ablated neutral particles, particularly for elements containing GAR [18].

In Figure 5-3 (blue spectrum), when the pulse duration of the driving field is reduced from 50 fs to 30 fs, the high-order harmonic cut-off is extended from 36 eV to 52 eV. In this spectrum, the

harmonics have peaks at 49.7 eV and 51.1 eV, whose intensities are significantly higher compared with those at energies below 49 eV. The energies of these intense harmonics, which are the 73rd and 75th harmonics of the 1.82 μm driving field, corresponding to the GAR of neutral manganese [19]. The high intensity of the harmonics around 50 eV indicates the involvement of GAR in HHG.

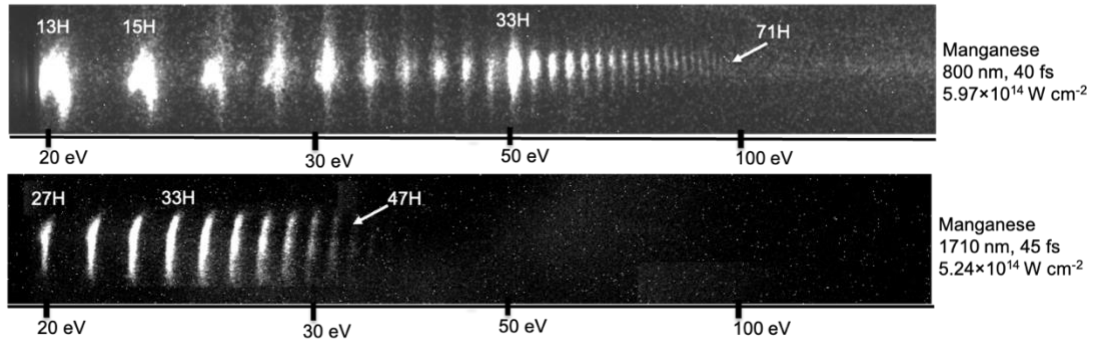


Figure 5-4 High-order harmonics spectrum with wavelengths; (a) 0.8 μm (main pulse energy = 2.5 mJ, pulse duration = ~40 fs, peak intensity = $5.97 \times 10^{14} \text{ W cm}^{-2}$) and (b) 1.71 μm (MP energy = 6mJ, pulse duration = 45 fs, peak intensity = $5.24 \times 10^{14} \text{ W cm}^{-2}$).

Since the GAR of manganese is broadband [20], the harmonic spectrum was recorded with few cycle-driving fields to see the effect of RH over a broad energy range, and the corresponding spectrum is shown in Figure 5-5. In this spectrum, a broadband continuum is observed with a significant intensity enhancement in the energy region from 49 eV to 53 eV, which corresponds to the GAR of neutral manganese [10]. Normally, high-order harmonics are generated from the ground state electron via the normal three-step process. In this case, the intensity of the harmonics close to the cut-off decreases rapidly. However, it has been observed that when resonances constructively contribute to coherent HHG, the harmonic intensity increases dramatically in the vicinity of the resonance involved [2,21,22]. In Figure 5-5, the high intensity of the harmonics around 50 eV, which are within the bandwidth of GAR [10], is clear evidence that these harmonics are generated from the GAR. It should be noted that the GAR of manganese is different for neutrals and ions [23]. In neutral manganese, the GAR appears from the 3p-3d transitions only. However, in the case of manganese ion (Mn^+), the 3p-4s channel also contributes to enhancing the PICS of Mn^+ . The symmetric intensity enhancement observed in Figure 5-5 of RH around 50 eV is also

another proof that high-order harmonics from laser-ablated manganese plume are generated from neutral manganese.

One interesting aspect of studying GAR is that these resonances involve multi-electron interactions [10]. The model proposed by Shiner *et al.* [12] for harmonic emission from xenon shows that such studies might be useful to explore electron-electron correlation via Coulomb interaction between energetic continuum electron and inner-shell 4d electron. However, our observation of harmonic emission from the GAR of neutral manganese at the exact energy of 3p-3d resonance (~50 eV) shows that the harmonic generation process in manganese might be different than the model proposed by Shiner *et al.* Our results will provide roots to investigate the core process involved in harmonic generation from the GAR and investigate their multi-electron interaction. To reduce the numerical complications for multi-electron interaction, we simulate the harmonic spectra from manganese using the model recently proposed by Strelkov [24].

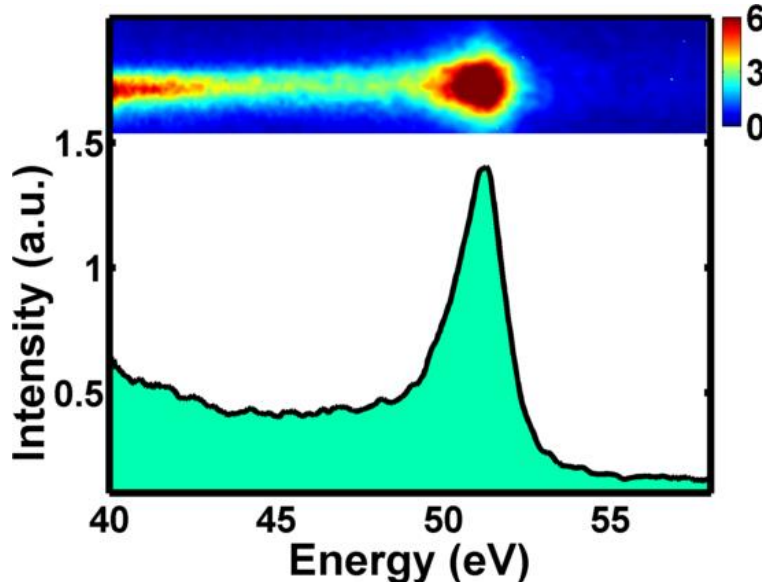


Figure 5-5 The high-order harmonic spectrum recorded with a few-cycle driving laser field at laser intensity $\sim 4.0 \times 10^{14} \text{ W cm}^{-2}$. In this spectrum, a broadband continuum is observed. The harmonic intensity is high at energies from 49 eV to 53 eV. The intensity enhancement in this energy region indicates that these harmonics are generated from the GAR of neutral manganese.

5.5 Numerical Methods

The plasma jet used in experiments is composed of neutral Mn as well as Mn^+ , and both types of particles have ground state to AIS transitions at energies of about 50 eV. Therefore, spectra emitted

by neutral Mn and Mn^+ were simulated. We calculate the spectra solving TDSE numerically for a model atom or ion in the laser field. The numerical method is described in reference [25]. We use the model potentials similar to the ones suggested in reference [21,26], which have an excited quasi-stable state modeling the AIS of the atom or ion. Choosing the parameters of the model potential, we reproduce the ionization energy of the generating particle, frequency of the transition from the ground state to the AIS, and the AIS width. More details of the used potentials are presented in the supplementary.

The calculated spectra presented in Figure 5-6 are averaged over the laser pulse carrier-envelope phase and the peak laser intensity. The latter averaging takes into account the spatial distribution of the fundamental intensity in the transverse section of the laser beam. The intensity averaging is very important, because the low ionization potential of neutral Mn leads to HHG under relatively low laser intensities (about an order of magnitude lower than the peak laser intensity in the focus of the experimentally used beam). The relatively large volume of the target where such intensities take place provides the main contribution to the total HHG signal.

The low fundamental frequency used in experiments leads to the TI regime of ionization, not only for Mn^+ , but also for neutral Mn, despite its low I_p . The I_p of neutral Mn and Mn^+ differ by more than two times (7.4 eV and 15.6 eV), resulting in dramatically different HHG spectra. The cut-off position in the neutral Mn spectrum is defined not by the peak laser intensity, but by the laser intensity providing complete ionization. Depending on the laser pulse duration, this intensity is about $0.3 - 0.5 \times 10^{14} \text{ W cm}^{-2}$, leading to the cut-off in the HHG spectra at 35 – 55 eV. In contrast, Mn^+ is not completely ionized up to the highest laser intensity used in experiments ($5 \times 10^{14} \text{ W cm}^{-2}$). Thus, the cut-off in the HHG spectrum is at about 0.5 keV. However, our TDSE calculations show that in the spectral range under experimental consideration (up to 60 eV with the few-cycle driving field, spectrum not shown) the XUV emitted by neutrals is much more intense than the XUV emitted by ions. Note that experimentally, this difference should be even more pronounced due to worse phase-matching in the highly-ionized medium. That is why below we calculated results only for neutral Mn and use the intensity of $1 \times 10^{14} \text{ W cm}^{-2}$ as the upper limit of the intensity averaging.

The TDSE solution allows one to study the ionization dynamics of Mn with laser pulses of different durations. These studies show that for a longer laser pulse (45 fs), the atoms are ionized at intensities of $0.3 - 0.4 \times 10^{14} \text{ W cm}^{-2}$, corresponding to the HHG cut-off at 35 - 45 eV. Therefore,

very few atoms survive up to higher intensities, which provide the harmonic plateau wide enough to “approach” the resonant frequency. This is why the resonant maximum is not very pronounced in the spectrum. Shortening of the laser pulse leads to the survival of a higher ratio of neutral atoms up to the intensities providing a wider plateau, including the resonant frequency. Therefore, the resonant maximum is better pronounced for the 30 fs pulse and very pronounced for the 12 fs pulse.

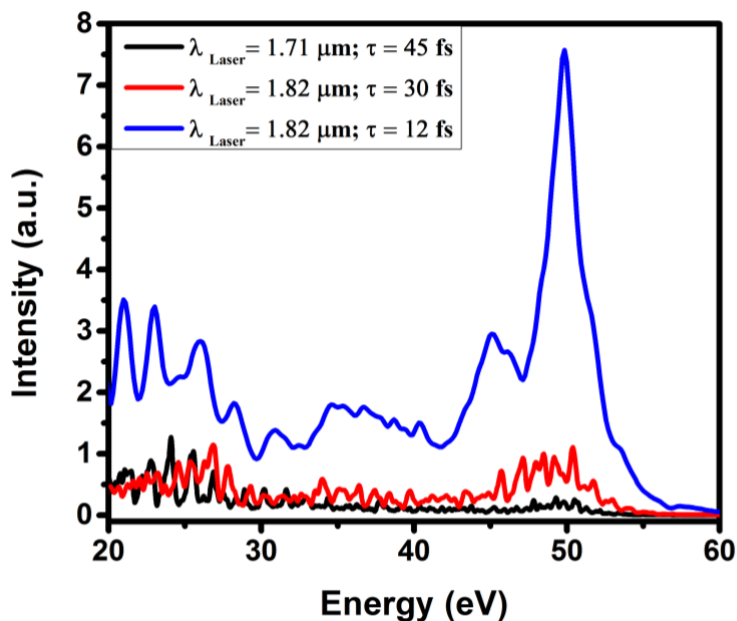


Figure 5-6 Calculated high-order harmonic spectra from manganese with driving fields of pulse durations 45 fs (black spectrum), 30 fs (red spectrum) and 12 fs (blue spectrum), and wavelengths $1.71 \mu\text{m}$, $1.82 \mu\text{m}$ and $1.82 \mu\text{m}$ respectively. These spectra are simulated with a laser intensity of $1 \times 10^{14} \text{ W cm}^{-2}$.

5.6 Summary of the Chapter

In summary, we studied the HHG from the LAP produced from manganese, a transition metal, using multicycle and few-cycle (~ 2 cycles) ultrashort laser pulse with a wavelength of $1.82 \mu\text{m}$. In all the previous HHG experiments using LAP as a nonlinear media, the high-order harmonics are generated from the ionic species. However, in our experiments with manganese LAP, we demonstrate that the high-order harmonics are predominantly generated from neutral atoms (with an ionization potential of 7.4 eV)). Our results open the possibility to advance the laser-ablation technique to study the dynamics of neutral atoms of low ionization potential. Moreover, as

manganese contains GAR, we demonstrate the intense and broadband RH from this resonance at energies from 49 to 53 eV. This opens the possibility to generate intense attosecond pulses directly from the giant resonances, as well as to study these resonances using high-harmonic spectroscopy. Our results also open the opportunity to generate harmonics from laser-ablated neutral particles and explore the dynamics of the GAR, such as photoionization, recombination on ultrafast timescales, and the role of multielectrons in HHG. Moreover, the intense harmonic emission from GAR will allow one to explore appropriate material for broadband XUV pulse generation. The previous knowledge tells us that the phase emission of high-order harmonics from atomic resonances is different from the normal high harmonics generated from the ground state electron. Further information about the phase emission will provide roots to use high harmonics from GAR directly for intense attosecond pulse production or by combining them with the normal harmonics.

5.7 References

1. R. A. Ganeev, M. Suzuki, M. Baba, and H. Kuroda, "Harmonic generation from chromium plasma," *Applied Physics Letters* **86**, 131116 (2005).
2. R. A. Ganeev, M. Suzuki, M. Baba, H. Kuroda, and T. Ozaki, "Strong resonance enhancement of a single harmonic generated in the extreme ultraviolet range," *Optics Letters* **31**, 1699 (2006).
3. R. A. Ganeev, L. B. E. Bom, J.-C. Kieffer, M. Suzuki, H. Kuroda, and T. Ozaki, "Demonstration of the 101st harmonic generated from a laser-produced manganese plasma," *Physical Review A* **76**, 023831 (2007).
4. F. L. & T. O. M.A. Fareed, V.V. Strelkov, N. Thire, S. Mondal, B.E. Schmidt, "High-order harmonic generation from the dressed autoionizing states," *Nature communications* **8**, 16061 (2017).
5. R. A. Ganeev, *High-Order Harmonic Generation in Laser Plasma Plumes* (World Scientific, 2013).
6. V. K. Dolmatov, A. S. Kheifets, P. C. Deshmukh, and S. T. Manson, "Attosecond time delay in the photoionization of Mn in the region of the , Physical Review A **91**, 053415 (2015).
7. S. Pabst and R. Santra, "Strong-field many-body physics and the giant enhancement in the high-harmonic spectrum of xenon," *Physical Review Letters* **111**, 233005 (2013).
8. M. V. Frolov, N. L. Manakov, and A. F. Starace, "Potential barrier effects in high-order harmonic generation by transition-metal ions," *Physical Review A* **82**, 023424 (2010).
9. M. V. Frolov, N. L. Manakov, T. S. Sarantseva, M. Y. Emelin, M. Y. Ryabikin, and A. F. Starace, "Analytic description of the high-energy plateau in harmonic generation by atoms: Can the harmonic power increase with increasing laser wavelengths?," *Physical Review Letters* **102**, 243901 (2009).
10. M. Martins, K. Godehusen, T. Richter, P. Wernet, and P. Zimmermann, "Open shells and multi-electron interactions: core level photoionization of the 3d metal atoms," *Journal of Physics B* **39**, R79–R125 (2006).
11. R. A. Ganeev, T. Witting, C. Hutchison, F. Frank, M. Tudorovskaya, M. Lein, W. A. Okell, A. Zaïr, J. P. Marangos, and J. W. G. Tisch, "Isolated sub-fs XUV pulse generation in Mn plasma ablation," *Optics Express* **20**, 25239 (2012).
12. F. L. & D. M. V. A. D. Shiner, B. E. Schmidt, C. Trallero-Herrero, H. J. Wörner, S. Patchkovskii, P. B. Corkum, J.-C. Kieffer, "Probing collective multi-electron dynamics in xenon with high-harmonic spectroscopy," (n.d.).
13. M. V. Frolov, N. L. Manakov, T. S. Sarantseva, M. Y. Emelin, M. Y. Ryabikin, and A. F. Starace, "Analytic description of the high-energy plateau in harmonic generation by atoms: Can the harmonic power increase with increasing laser wavelengths?," *Physical Review Letters* **102**, 243901 (2009).
14. D. Faccialà, S. Pabst, B. D. Bruner, a. G. Ciriolo, S. De Silvestri, M. Devetta, M. Negro, H. Soifer, S. Stagira, N. Dudovich, and C. Vozzi, "Probe of Multielectron Dynamics in Xenon by Caustics in High-Order Harmonic Generation," *Physical Review Letters* **117**, 093902 (2016).
15. J. Zhang and D.-S. Guo, "Spectral Minimum and Giant Enhancement in Photoelectron Spectra from Xenon Atoms Driven by Intense Midinfrared Laser Fields," *Physical Review Letters* **110**, 063002 (2013).
16. T. Brabec and F. Krausz, "Intense few-cycle laser fields: Frontiers of nonlinear optics," *Reviews of Modern Physics* **72**, 545–591 (2000).

17. M. V. Frolov, N. L. Manakov, and A. F. Starace, "Potential barrier effects in high-order harmonic generation by transition-metal ions," *Physical Review A* **82**, 023424 (2010).
18. R. A. Ganeev, "The second plateau in the distribution of high harmonics generated in plasma torches," *Optics and Spectroscopy* **105**, 930–935 (2008).
19. J. Costello, E. Kennedy, B. Sonntag, and C. Clark, "3p photoabsorption of free and bound Cr, Cr⁺, Mn, and Mn⁺," *Physical Review A* **43**, 1441–1450 (1991).
20. J. Costello, E. Kennedy, B. Sonntag, and C. Clark, "3p photoabsorption of free and bound Cr, Cr⁺, Mn, and Mn⁺," *Physical Review A* **43**, 1441–1450 (1991).
21. V. Strelkov, "Role of autoionizing state in resonant high-order harmonic generation and attosecond pulse production," *Physical Review Letters* **104**, (2010).
22. J. Rothhardt, S. Hädrich, S. Demmler, M. Krebs, S. Fritzsche, J. Limpert, and A. Tünnermann, "Enhancing the macroscopic yield of narrow-band high-order harmonic generation by fano resonances," *Physical Review Letters* **112**, (2014).
23. J. W. Cooper, C. W. Clark, C. R. Cromer, T. B. Lucatorto, B. F. Sonntag, E. T. Kennedy, and J. T. Costello, "Marked differences in the 3 p photoabsorption between the Cr and Mn + isoelectronic pair: Reasons for the unique structure observed in Cr," *Physical Review A* **39**, 6074–6077 (1989).
24. V. V. Strelkov, "Attosecond-pulse production using resonantly enhanced high-order harmonics," *Physical Review A* **94**, 063420 (2016).
25. V. V. Strelkov, A. F. Sterjantov, N. Y. Shubin, and V. T. Platonenko, "XUV generation with several-cycle laser pulse in barrier-suppression regime," *Journal of Physics B* **39**, 577 (2006).
26. V. v. Strelkov, "Attosecond-pulse production using resonantly enhanced high-order harmonics," *Physical Review A* **94**, 063420 (2016).

Chapter 6

Resonant High-order Harmonic Generation from Sn III States

6.1 Introduction

In the HHG mechanism as per the three-step model, the TI of the valence shell electron and its recombination back into the initial ground state is an important event [1], and both of these processes have proven to be a sensitive probe to the electronic and orbital structure of the atom, ion or molecule participating in the harmonic generation [2][3][4], and has shown their potential as a powerful spectroscopic tool [5][6][7][8][9][10]. The generation of coherent attosecond pulses from HHG combined with the pump-probe spectroscopic technique has enabled the time-resolved spectroscopic studies of the atomic and molecular system with femtosecond temporal resolution [4][11].

A popular nonlinear medium for HHG is noble gases, involving harmonic generation from neutral gas atoms [12]. However, HHG has also been demonstrated from LAP, which can contain both neutral and ionic species. Extensive experimental and theoretical studies on HHG from LAP has contributed to extending our understanding of the physics of its HHG mechanisms [13][14][15][16]. One phenomenon of significant importance is the RH intensity enhancement of a single harmonic order from the singly charged ions in a variety of LAPs, resulting in intense fs and attosecond XUV emission with the potential for microjoule level harmonic energies [13][14][17][18][19]. For example, the RH from tin LAP is observed when the driving laser photon is multiphoton resonant with the strong radiative transition $4d^{10}5s^25p\ ^2P_{3/2} \rightarrow 4d^95s^25p^2\ (^1D)\ ^2D_{5/2}$ at 26.27 eV with large oscillator strength [14]. Other examples include the RH generation from the LAP of indium [13], chromium [17] and manganese [20][21]. Such a resonant phenomenon cannot be explained by the three-step model, which has led to the introduction of the four-step model for the HHG mechanism [15][22]. The first two steps in the four-step model are the same as in the three-step model, *i.e.*, the TI of the valence electron and its acceleration in the continuum. However, the third step involves the trapping of the tunnel-ionized electron into an AIS located above the I_p corresponding to the presence of a strong electronic transition, followed by the radiative recombination of the electron from the AIS into the initial ground state emitting intense RH [15]. Such a resonant phenomenon in LAPs allows one to study

the dynamics of these AISs at fs timescale through the signatures seen in the corresponding harmonic spectrum, *i.e.* it provides a convenient method of performing high-harmonic spectroscopy of these electronic states [16]. Recently, the HHG technique from LAP has also demonstrated RH generation from neutral atoms [20], hence establishing the versatility of this technique.

In previous studies, attempts were made to study HHG from doubly charged ions. For example, HHG from Mn III resulted in XUV beyond 150 eV photon energies [21]. Another example is the experiments with tin LAP observing the response of Sn III in the harmonic enhancement [23][24]. However, in these past studies with tin LAP using 800 nm wavelength driving laser, the energy gap between consecutive harmonic orders were relatively large, which did not allow the simultaneous probing of multiple Sn III transitions. For example, previous studies reported the enhancement for only a single harmonic near the Sn III transition $4d^{10}5s^2\ ^1S_0 \rightarrow 4d^95s^25p\ ^1P_1$ at 27.6 eV [23][24]. However, in our experiments, at 800 nm driving laser wavelength, we observe the splitting of the 17th harmonic (17H) into multiple components indicating clearly the response of Sn III transitions located at 26.83 eV and 27.14 eV, which are close to the well-known 26.27 eV AIS transition of Sn II generating RH as per the four-step model [15]. This harmonic splitting was not observed in the previous studies [23][24]. To reduce the energy gap between the consecutive harmonic orders, and hence to allow to probe multiple transitions of Sn III simultaneously, we use longer 1750 nm and 1780 nm driving laser wavelengths and observe multiple harmonic enhancements in the photon energy range between 25 eV and 30 eV where many strong transitions of Sn III can be identified.

6.2 HHG from tin LAP using 800 nm Laser Wavelength

The HHG spectrum generated from the tin LAP with 800 nm driving laser wavelength is shown in Figure 6-1. Within the energy range between 16 eV and 25 eV, the harmonic spectrum shows that the intensity of the harmonics decreases monotonically as the photon energy increases. However, we observe an intensity enhancement of the 17H relative to the neighboring harmonic. At 800 nm laser wavelength, the AIS transition $4d^{10}5s^25p\ ^2P_{3/2} \rightarrow 4d^95s^25p^2\ (^1D)\ ^2D_{5/2}$ of Sn II at 26.27 eV, which has a large oscillator strength of 1.52, is 17-photon resonant with the driving laser photon [25]. As per the four-step model, the multiphoton resonance of this AIS with the driving laser results in the generation of RH at 17H with significant intensity enhancement relative to the neighboring harmonics [14][15].

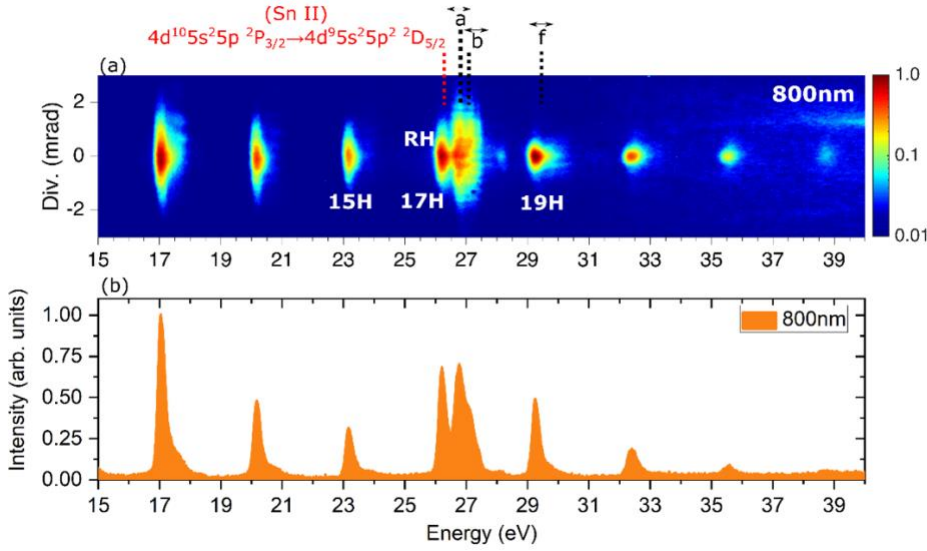


Figure 6-1 The HHG spectrum generated from tin LAP (a) with 800 nm driving laser wavelength at a laser intensity of 7×10^{14} W cm $^{-2}$. (b) The corresponding line plot obtained by vertically integrating the HHG spectrum. The 17H is generated as per the four-step model due to the involvement of AIS at 26.27 eV, labelled as RH in the figure. The 17H is close to the transitions of Sn III at 26.83 eV and 27.14 eV (labelled as \vec{a} and \vec{b} as shown in Figure 6-1(a) and Table 6-1). The splitting of the 17H into multiple components due to the close vicinity of the RH to the Sn III transitions is clear evidence of the involvement of the Sn III in the HHG process.

6.3 Various Sn III Transitions in the Range 26-30 eV

We show in Table 6-1 the various Sn III transitions corresponding to the different upper term eigenvector compositions in JJ coupling for the transition $4d^{10}5s5p \rightarrow 4d^95s5p^2$. These transitions are identified by Duffy *et al.* [25] by recording the 4d-5p photoabsorption spectra of Sn III using a 1 m normal incidence spectrograph and the dual laser plasma technique along with the identification of various recorded transitions using multiconfiguration HF calculations [25].

The transitions labelled \vec{a} and \vec{b} in Table 6-1 are in close vicinity of the 17H, and we clearly see in Figure 6-1 that the 17H order is split into multiple harmonic components. This harmonic splitting clearly indicates the involvement of Sn III in the HHG mechanism. The transition labelled \vec{f} is close to the 19H order, and we also see the intensity enhancement for the 19H relative to the neighboring harmonics.

Table 6-1 The various upper term eigenvector compositions in JJ coupling for the transition $4d^{10}5s5p \rightarrow 4d^95s5p^2$ of Sn III taken from the data published in the reference [25]. The ' refers to $(5/2, 1/2)$ core, '' to the $(3/2, 1/2)$ core and the subscript refers to the total J .

Label	Ion	Transition	E (eV)	gf-value
\vec{a}	Sn III	$(1/2, 3/2)_2 \rightarrow (2'',2)_3$	26.83	0.38
\vec{b}	Sn III	$(1/2, 3/2)_2 \rightarrow (2'',2)_1$	27.14	0.20
\vec{c}	Sn III	$(1/2, 3/2)_1 \rightarrow (3',2)_2$	28.33	0.51
\vec{d}	Sn III	$(1/2, 3/2)_2 \rightarrow (3',2)_3$	28.48	0.84
\vec{e}	Sn III	$(1/2, 3/2)_2 \rightarrow (3',2)_1$	28.80	0.33
\vec{f}	Sn III	$(1/2, 3/2)_2 \rightarrow (1'',2)_2$	29.47	0.20

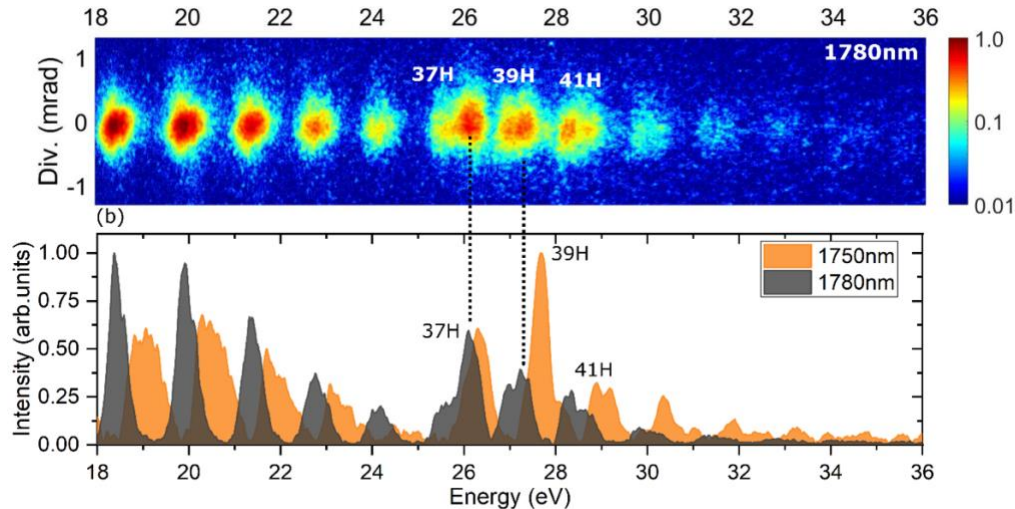


Figure 6-2 HHG spectrum generated from tin LAP **(a)** using 1780 nm driving laser wavelength and **(b)** the line plot of the HHG spectrum using 1780 nm and 1750 nm driving laser wavelength, both at a driving laser intensity of $5 \times 10^{14} \text{ W cm}^{-2}$. The line spectrum is obtained by vertically integrating the HHG spectrum. Multiple harmonic enhancements are observed in the energy region between 25 eV and 30 eV, and there exist numerous strong electronic transitions in this energy range, as shown in Table 6-1.

6.4 HHG from Tin LAP using Longer 1750 nm and 1780 nm Laser Wavelengths

As shown in Table 6-1, there are many other Sn III transitions in the energy range between 26 eV and 30 eV. At 800 nm driving laser wavelength, all these transitions were not probed due to the

relatively large energy difference between the two consecutive odd harmonic orders. This difference between the consecutive harmonics can be reduced by operating at longer driving laser wavelengths.

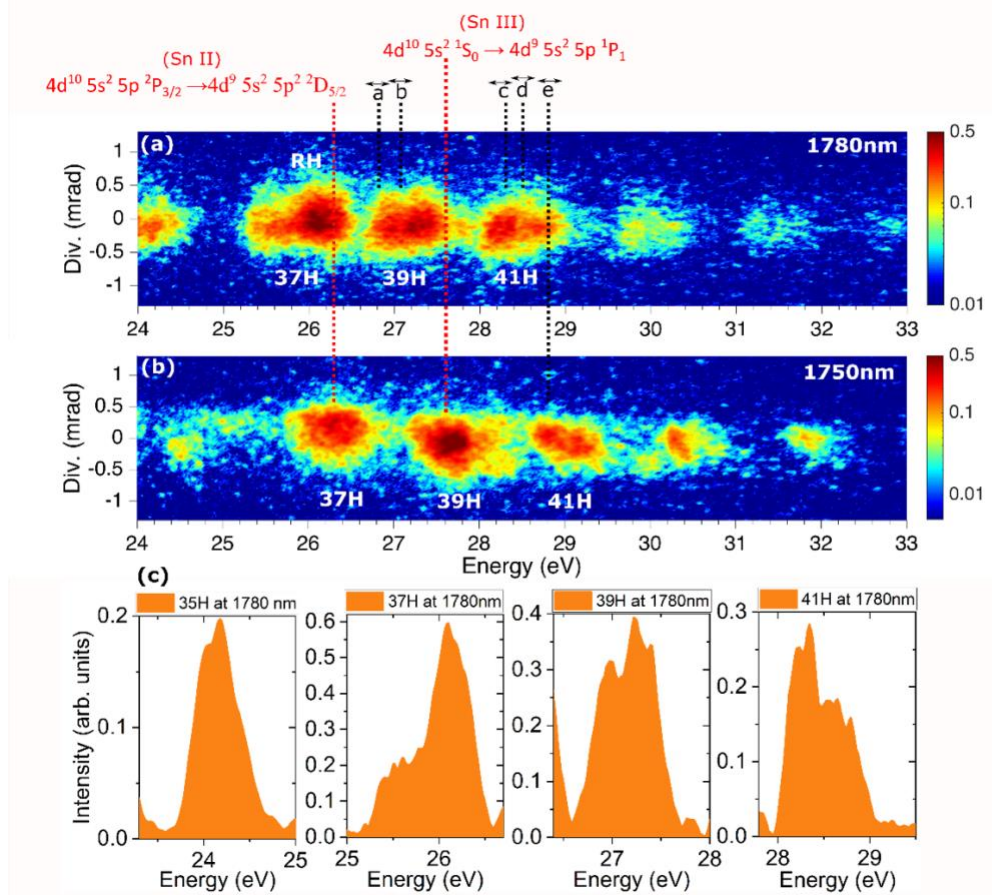


Figure 6-3 The expanded view of the HHG spectra generated from tin LAP in the energy range between 24 eV and 33 eV **(a)** using 1780 nm and **(b)** using 1750 nm driving laser wavelength. **(c)** The vertically integrated line profile of 35H-41H harmonic orders generated using 1780 nm driving laser wavelength. The multiple strong electronic transitions of Sn III are present in the range between 26 eV and 30 eV, as shown in Table 6-1, and the enhanced 39H and 41H have photon energies within this range.

Figure 6-2(a) and Figure 6-2(b) show the harmonic spectra generated from tin LAP using 1750 nm and 1780 nm driving laser wavelength, both at a laser intensity of $5 \times 10^{14} \text{ W cm}^{-2}$. As can be seen, in the energy range between 18 eV and 25 eV, the intensity of the harmonic orders decreases monotonically towards the higher photon energies. However, in the energy range between 26 eV and 30 eV, we see multiple harmonic intensity enhancements. At 1750 nm driving laser wavelength, the AIS transition $4d^{10}5s^25p\ ^2P_{3/2} \rightarrow 4d^95s^25p^2\ (^1D)\ ^2D_{5/2}$ of Sn II at 26.27 eV is 37-photon resonant with the driving laser photon. Therefore, as per the four-step model [15], the 37H

order is generated with intensity enhancement relative to the neighboring 35H. However, as shown in Figure 6-2, intensity enhancement is also observed for the 39H as well as the 41H.

To understand better the harmonic enhancements, we show in Figure 6-3(a) and Figure 6-3(b) the expanded view of the harmonic spectra. The various electronic transitions of Sn III are marked and labelled in the harmonic spectra. The enhanced harmonic orders are located within the range where the transitions of Sn III are located. For example, at 1780 nm driving laser wavelength, as shown in Figure 6-3(a), the 39H order is located in the close vicinity of the transition \vec{a} and \vec{b} of Sn III at an energy 26.83 eV and 27.14 eV, respectively (see Table 6-1). Similarly, at 1780 nm driving laser wavelength, the 41H order is located in the close vicinity of the transition \vec{c} , \vec{d} and \vec{e} at an energy 28.33 eV, 28.48 eV and 28.80 eV, respectively. The intense 39H at 1750 nm driving laser wavelength, as shown in Figure 6-3(b), is generated due to multiphoton resonance with the Sn III transition $4d^{10}5s^2\ ^1S_0 \rightarrow 4d^95s^25p\ ^1P_1$ located at an energy of 27.6 eV, which has a large oscillator strength of 0.87 [24]. Figure 6-3(c) shows the line plots obtained by vertically integrating the harmonic spectra for the 35H-41H order. The 35H generated without the involvement of any resonance has a symmetric Gaussian line profile. However, the line profile of the 37H, 39H as well as the 41H are asymmetric due to the perturbation of the multiple resonant transitions.

6.5 Energy Level Diagram of Sn II and Sn III

In Figure 6-4, we show the energy level diagram of Sn II and Sn III to explain the HHG process in tin LAP. Sn II has ground state configuration $4d^{10}5s^25p\ ^2P_{3/2}$ and has an AIS $4d^95s^25p^2\ ^2D_{5/2}$ located at 26.27 eV. This AIS can be coherently excited through resonant multiphoton excitation with the driving laser photon, *e.g.* 17-photon and 37-photon resonance with the 800 nm and 1750 nm driving laser wavelength, respectively. The strong radiative transition $4d^{10}5s^25p\ ^2P_{3/2} \rightarrow 4d^95s^25p^2\ (^1D)\ ^2D_{5/2}$ generates RH as per the four-step model [15]. Apart from the transition from the AIS into the initial ground state of the Sn II, another possibility is the photoionization of this AIS from 5s or 5p state producing the Sn III, landing the system into the state $4d^95s5p^2$ or $4d^95s^25p\ ^1P_1$, respectively. The transition $4d^{10}5s^2\ ^1S_0 \rightarrow 4d^95s^25p\ ^1P_1$ at 27.6 eV has a high oscillator strength of 0.87, and generates an intense harmonic as shown in Figure 6-3(b) [24]. For the transition $4d^{10}5s5p \rightarrow 4d^95s5p^2$, various eigenvector compositions in *JJ* coupling located in the energy range between 26 eV and 30 eV are shown in Table 6-1. As shown in Figure 6-3, multiple harmonic enhancements observed are within this range of Sn III transitions. For the Sn III transition $4d^{10}5s^2$

$^1S_0 \rightarrow 4d^95s^25p\ ^1P_1$ at 27.6 eV, the harmonic enhancement is seen highest among other harmonics, as shown in Figure 6-2 and Figure 6-3(b) showing intense 39H at 1750 nm driving laser wavelength. This could be due to the lower photoionization energy required for the photoionization from the initial AIS $4d^95s^25p^2\ ^2D_{5/2}$ of Sn II into the state $4d^95s^25p\ ^1P_1$ (15.9 eV) compared to the photoionization into the state $4d^95s^25p^2$ (24.1 eV), as shown in Figure 6-4.

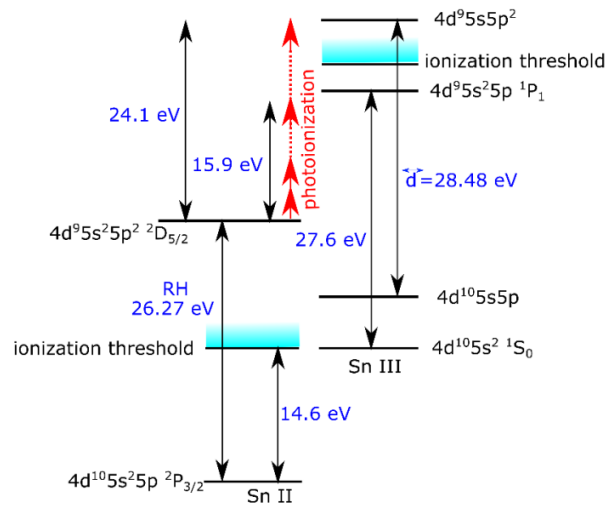


Figure 6-4 Energy level diagram of Sn II and Sn III

As per the three-step model, the harmonic cut-off energy, which is the maximum photon energy emitted in the harmonic generation, is the sum of the I_p of the parent atom/ion undergoing TI and the kinetic energy of the valence shell electron at the moment of recombination into the initial ground state of the parent ion [1]. Therefore, the harmonic cut-off observed when the electron undergoing TI belongs to the ground state of Sn III should be higher than the value observed for the case of the involvement of Sn II due to the higher value of I_p for Sn III compared to Sn II. However, the harmonic cut-off observed in the harmonic spectrum in Figure 6-1 is ~39 eV, similar to what was observed in the previous studies where Sn II was the species responsible for the harmonic generation [14]. To explain this, it is important to notice that in the energy level diagram shown in Figure 6-4, the Sn III participating in the HHG is generated by the photoionization of the AIS $4d^95s^25p^2\ ^2D_{5/2}$ of Sn II. Hence, in the harmonic generation mechanism, the TI occurs for the valence shell electron of Sn II, while the Sn III is generated due to the photoionization of the AIS $4d^95s^25p^2\ ^2D_{5/2}$ of Sn II.

To check with the coherence of RHs from Sn III, it is important to note that the HHG is a phase-matched process [26], *i.e.*, all the atoms/ions taking part in the HHG constructively add their harmonic signal coherently. Consequently, the harmonic signal builds up that co-propagates with the driving laser beam. This process is very distinct from the spontaneous incoherent emission of atoms/ions in all directions, *i.e.*, at a solid angle of 4π steradians [27]. The well-collimated nature of the harmonics from Sn III resonances confirms their coherent nature, which is very distinct from the incoherent spontaneous emission, which will span the entire width of the microchannel plate detector in the form of vertical lines [27].

6.6 Summary of the Chapter

To summarize, we studied HHG from laser-ablated tin using ultrashort driving lasers with 800 nm, 1750 nm and 1780 nm wavelengths. We report multiple harmonic enhancements in the XUV region due to the involvement of Sn III transitions. At 800 nm laser wavelength, we observe the splitting of 17H order into multiple components due to the presence of strong Sn III transitions at 26.83 eV and 27.14 eV, which are located in the close vicinity of the previously well-known strong autoionization transition of Sn II at 26.27 eV generating single harmonic enhancement as per the four-step model. At 1750 nm and 1780 nm, we observe multiple harmonic enhancements in the range between 26 eV and 30 eV, where several strong transitions of Sn III are identified. The harmonic cut-off observed is similar to the values observed in previous studies where Sn II was responsible for the harmonic generation. This observation suggests that Sn III does not participate in the harmonic generation process directly through the TI of its valence shell electron, but could appear in the harmonic generation mechanism through the photoionization of the AIS of Sn II. Our results demonstrate the potential of HHG as a convenient technique for the high harmonic spectroscopy of the Sn III.

6.7 References

1. P. B. Corkum, "Plasma perspective on strong field multiphoton ionization," *Physical Review Letters* **71**, 1994–1997 (1993).
2. H. J. Wörner, H. Niikura, J. B. Bertrand, P. B. Corkum, and D. M. Villeneuve, "Observation of electronic structure minima in high-harmonic generation," *Physical Review Letters* **102**, 103901 (2009).
3. S. Haessler, J. Caillat, and P. Salières, "Self-probing of molecules with high harmonic generation," *Journal of Physics B* **44**, 203001 (2011).
4. A. Trabattoni, M. Klinker, J. González-Vázquez, C. Liu, G. Sansone, R. Linguerri, M. Hochlaf, J. Klei, M. J. J. Vrakking, F. Martín, M. Nisoli, and F. Calegari, "o," *Physical Review X* **5**, 041053 (2015).
5. P. M. Kraus, O. I. Tolstikhin, D. Baykusheva, A. Rupenyan, J. Schneider, C. Z. Bisgaard, T. Morishita, F. Jensen, L. B. Madsen, and H. J. Wörner, "Observation of laser-induced electronic structure in oriented polyatomic molecules," *Nature Communications* **6**, 1–8 (2015).

6. N. L. Wagner, A. Wüest, I. P. Christov, T. Popmintchev, X. Zhou, M. M. Murnane, and H. C. Kapteyn, "Monitoring molecular dynamics using coherent electrons from high harmonic generation," *Proceedings of the National Academy of Sciences of the United States of America* **103**, 13279–13285 (2006).
7. A. D. Shiner, B. E. Schmidt, C. Trallero-Herrero, H. J. Wörner, S. Patchkovskii, P. B. Corkum, J.-C. Kieffer, F. Légaré, and D. M. Villeneuve, "Probing collective multi-electron dynamics in xenon with high-harmonic spectroscopy," *Nature Physics* **7**, 464–467 (2011).
8. M. C. H. Wong, A. T. Le, A. F. Alharbi, A. E. Boguslavskiy, R. R. Lucchese, J. P. Brichta, C. D. Lin, and V. R. Bhardwaj, "High harmonic spectroscopy of the cooper minimum in molecules," *Physical Review Letters* **110**, 033006 (2013).
9. C. T. Liao, X. Li, D. J. Haxton, T. N. Rescigno, R. R. Lucchese, C. W. McCurdy, and A. Sandhu, "Probing autoionizing states of molecular oxygen with XUV transient absorption: Electronic-symmetry-dependent line shapes and laser-induced modifications," *Physical Review A* **95**, 043427 (2017).
10. J. Itatani, J. Levesque, D. Zeidler, H. Niikura, H. Pépin, J. C. Kieffer, P. B. Corkum, and D. M. Villeneuve, "Tomographic imaging of molecular orbitals," *Nature* **432**, 867–871 (2004).
11. H. J. Wörner, J. B. Bertrand, D. v. Kartashov, P. B. Corkum, and D. M. Villeneuve, "Following a chemical reaction using high-harmonic interferometry," *Nature* **466**, 604–607 (2010).
12. C. Winterfeldt, C. Spielmann, and G. Gerber, "*Colloquium*: Optimal control of high-harmonic generation," *Reviews of Modern Physics* **80**, 117–140 (2008).
13. R. A. Ganeev, M. Suzuki, M. Baba, H. Kuroda, and T. Ozaki, "Strong resonance enhancement of a single harmonic generated in the extreme ultraviolet range," *Optics Letters* **31**, 1699 (2006).
14. M. Suzuki, M. Baba, R. Ganeev, H. Kuroda, and T. Ozaki, "Anomalous enhancement of a single high-order harmonic by using a laser-ablation tin plume at 47 nm," *Optics Letters* **31**, 3306 (2006).
15. V. Strelkov, "Role of autoionizing state in resonant high-order harmonic generation and attosecond pulse production," *Physical Review Letters* **104**, (2010).
16. M. A. Fareed, V. V. Strelkov, N. Thiré, S. Mondal, B. E. Schmidt, F. Légaré, and T. Ozaki, "High-order harmonic generation from the dressed autoionizing states," *Nature Communications* **8**, 16061 (2017).
17. R. A. Ganeev, P. A. Naik, H. Singhal, J. A. Chakera, and P. D. Gupta, "Strong enhancement and extinction of single harmonic intensity in the mid- and end-plateau regions of the high harmonics generated in weakly excited laser plasmas," *Optics Letters* **32**, 65 (2007).
18. M. A. Fareed, N. Thiré, S. Mondal, B. E. Schmidt, F. Légaré, and T. Ozaki, "Efficient generation of sub-100 eV high-order harmonics from carbon molecules using infrared laser pulses," *Applied Physics Letters* **108**, 124104 (2016).
19. M. Singh, M. A. Fareed, A. Laramée, E. Isgandarov, and T. Ozaki, "Intense vortex high-order harmonics generated from laser-ablated plume," *Applied Physics Letters* **115**, 231105 (2019).
20. M. A. Fareed, V. V. Strelkov, M. Singh, N. Thiré, S. Mondal, B. E. Schmidt, F. Légaré, and T. Ozaki, "Harmonic Generation from Neutral Manganese Atoms in the Vicinity of the Giant Autoionization Resonance," *Physical Review Letters* **121**, 023201 (2018).
21. R. A. Ganeev, L. B. E. Bom, J. C. Kieffer, M. Suzuki, H. Kuroda, and T. Ozaki, "Demonstration of the 101st harmonic generated from a laser-produced manganese plasma," *Physical Review A* **76**, (2007).
22. V. V. Strelkov, M. A. Khokhlova, and N. Y. Shubin, "High-order harmonic generation and Fano resonances," *Physical Review A* **89**, 053833 (2014).
23. R. A. Ganeev, J. A. Chakera, P. A. Naik, H. Singhal, R. A. Khan, and P. D. Gupta, "Resonance enhancement of single even harmonic of laser radiation in tin-containing plasma using intensity variation of two-color pump," *Journal of the Optical Society of America B* **28**, 1055 (2011).
24. R. A. Ganeev, V. V. Strelkov, C. Hutchison, A. Zaïr, D. Kilbane, M. A. Khokhlova, and J. P. Marangos, "Experimental and theoretical studies of two-color-pump resonance-induced enhancement of odd and even harmonics from a tin plasma," *Physical Review A* **85**, 023832 (2012).
25. G. Duffy, P. van Kampen, and P. Dunne, "4d→5p transitions in the extreme ultraviolet photoabsorption spectra of Sn II and Sn III," *Journal of Physics B* **34**, 3171–3178 (2001).
26. T. Popmintchev, M. C. Chen, A. Bahabad, M. Gerrity, P. Sidorenko, O. Cohen, I. P. Christov, M. M. Murnane, and H. C. Kapteyn, "Phase matching of high harmonic generation in the soft and hard X-ray regions of the spectrum," *Proceedings of the National Academy of Sciences of the United States of America* **106**, 10516–10521 (2009).
27. V. V. K. & A. S. A. Mazhar Iqbal, Rashid A. Ganeev, Ganjaboy S. Boltaev, "Incoherent and coherent extreme ultraviolet emission from boron plasma," *The European Physical Journal D* volume **74**, 28 (2020).

Chapter 7

Conclusions of the Thesis

In this thesis, we presented the results from our investigations on the RH generation from a range of LAPs using a range of driving laser wavelengths. From Ga^+ in the LAP from gallium, we demonstrated for the first time in the MPI regime a compact, intense QM-XUV source based on HHG using the LAP technique. The observation of an increase in the ER with an increased Keldysh parameter showed that the use of short wavelength lasers results in an intense RH with superior ER. This important observation will pave the ways to find further methods to completely suppress the non-resonant harmonics, generating only the single RH free of other non-resonant harmonics, which are typically observed as a long harmonic plateau in the TI regime. The gallium LAP driven by a 400 nm laser demonstrates an unprecedented ER of 714 delivered without any monochromator installation, hence preventing a substantial loss of XUV flux. Our demonstration of an intense, coherent table-top source of XUV based on RH from LAP is novel considering the many limitations imposed by the fundamental laser physics, which have restricted the development of compact and high-intensity short-wavelength fs laser systems in the XUV region of the electromagnetic spectrum. Our findings pave the way towards the route to employing intense QM-XUV sources based on LAP to the experimental end-station, delivering high flux XUV having an unprecedented monochromaticity achieved without any monochromator in the beamline. The new observation of RH in the MPI regime will also motivate further theoretical studies for a better understanding of the dynamics of AIS, and its role in the mechanism of RH generation in the previously unexplored MPI regime of laser-matter interaction.

Our investigations on the single-BTH demonstrated the new phenomenon of the generation of an intense resonant single-BTH with an intensity ER of more than an order of magnitude relative to the neighboring non-resonant harmonics. We used In^+ and Ga^+ for the HHG and compared their response with Sn^+ and Cr^+ . This comparison suggested that the harmonic enhancement for the single-BTH occurs only for elements with AIS present in the close vicinity of I_p , and if there is a multiphoton resonance between the I_p and the driving laser photon. We proposed a coupling scheme showing the possibility of single-BTH enhancement due to the overlap of a suitable dressed-AIS with the Rydberg cloud. The experimental results were qualitatively reproduced with the TDSE calculations with model potential for In^+ at 1780 nm driving laser wavelength. These

results will broaden the scope of the involvement of AISs in the RH phenomenon and provide a new method for intense XUV light generation. This will open new directions for future studies to explore further the details of the physics of the coupling of the dressed-AISs with the Rydberg cloud via high-order harmonic spectroscopy.

Our studies on the application of mid-IR driving fields for HHG from laser-ablated manganese showed that high-order harmonics are observed from neutral manganese. This observation will be useful to extend harmonic studies from ionic species to neutrals with a mid-IR driving field that will also reduce the laser intensity requirement of harmonic study from elements having low ionization energy. Moreover, it was observed that laser pulses with pulse durations of 30 fs or shorter are required to produce harmonics from the GAR of manganese. Intense RH from GAR has been demonstrated in the energy region from 49 eV to 53 eV with a few-cycle driving field. The RH emission in this energy region confirms the direct involvement of GAR in HHG. Further, numerical calculations performed to simulate the harmonic spectra were in good agreement with the experimental results. Our results open the possibility to generate harmonics from the laser-ablated neutral particles and explore the dynamics of the GAR such as photoionization, and recombination at ultrafast time scales. The intense harmonic emission from GAR will allow exploring appropriate material for broadband XUV pulse generation. It is observed that the phase emission of RH is different from the normal harmonics generated from the ground state electron with the normal three-step process. Further information about the phase emission will provide roots to use RH directly from GAR for intense attosecond pulse production or by combining them with the normal harmonics.

Finally, we demonstrated the resonant multiple harmonic enhancements in the harmonic spectrum of tin LAP due to the role of Sn III transitions in the harmonic generation from tin LAP. The harmonic splitting observed for the 17H at 800 nm driving laser field gave clear evidence of the involvement of Sn III. At a longer driving wavelength of 1750 nm and 1780 nm, we identified various electronic transitions of Sn III in resonance with the enhanced multiple harmonics. The harmonic cut-off observed was lower than what is expected for Sn III, and was explained by the formation of Sn III due to the photoionization of the AIS of the Sn II. The present results demonstrate the potential of HHG as a convenient technique for the high harmonic spectroscopy of the Sn III.

Chapter 8

Résumé en Français

Génération Résonnantes d'harmoniques d'ordre Supérieur à partir d'un Panache par Ablation Laser: Quelques Nouvelles Perspectives

8.1 Motivation

L'invention du laser est considérée comme l'une des plus grandes percées scientifiques du 20e siècle. Grâce aux progrès récents dans la conception de lasers pulsés ayant une durée d'impulsion de quelques femtosecondes (fs), les paquets d'ondes lumineuses ne contiennent que quelques oscillations du champ électromagnétique. [1]. En focalisant ces impulsions ultra-rapides, des champs lumineux confinés d'une durée aussi courte sont capables de créer des intensités extrêmement puissantes pouvant atteindre $10^{15} \text{ W cm}^{-2}$ pour une énergie d'impulsion de l'ordre de 1 mJ. De telles intensités élevées sont suffisamment fortes pour éliminer les forces de Coulomb qui lient ensemble les atomes et les molécules et permettent ainsi d'étudier les phénomènes physiques à l'origine des ionisations atomiques et moléculaires. Les impulsions laser de très courte durée ouvrent également une voie permettant de réaliser des études à résolution temporelle sur la dynamique ultra-rapide de nombreux phénomènes atomiques et moléculaires [2]. En raison des limitations imposées par la physique fondamentale, la plupart des lasers commerciaux ne fonctionnent que dans la région visible ou à plus grande longueur d'onde du spectre électromagnétique. De telles limitations comprennent la réduction de la section transversale d'émission stimulée, la diminution de la durée de vie du niveau d'énergie d'un milieu actif donné et l'augmentation des effets d'élargissement du niveau d'énergie à des longueurs d'onde plus courtes. En conséquence, l'inversion de population, qui est une condition essentielle pour que le laser fonctionne, diminue rapidement avec la diminution de la longueur d'onde laser λ , comprise entre λ^{-4} à λ^{-6} [3]. Ce dernier point rend les lasers extrêmement inefficaces à des longueurs d'onde plus courtes, ce qui a découragé les efforts de commercialisation de ces systèmes.

Au cours des années récentes, la génération d'harmoniques d'ordre élevé (ou HHG, pour "High-order harmonic generation") dans les gaz nobles a démontré être une excellente source de rayonnement cohérent dans les régions de l'ultraviolet extrême (XUV) et des rayons X.

HHG est un processus extrêmement non linéaire qui est entraîné par une interaction laser-matière de haute intensité entre un milieu non-linéaire et une impulsion laser ultra-rapide de haute intensité[4]. Cependant, étant donné que HHG est un processus non-linéaire et non perturbateur, son efficacité de conversion (CE) est extrêmement faible, allant de 10^{-8} à 10^{-6} pour divers gaz nobles ne générant que des valeurs de l'énergie nJ des impulsions XUV [5]. Ce faible rendement de l'énergie limite les applications potentielles de ces sources.

8.2 HHG du Panache créé par Ablation Laser

Le HHG du panache créé par ablation laser (LAP) est une source efficace de rayonnement XUV cohérent et de rayons. Dans de nombreux LAP, il a été noté que l'intensité d'un ordre harmonique est exceptionnellement élevée par rapport à celles des harmoniques voisines [6]. Ce phénomène est connu sous le nom de HHG résonant et l'harmonique correspondante est nommée harmonique de résonance (RH). Par exemple, comme le montre la Figure F-1, dans le cas de l'indium LAP, RH est observée à 61,2 nm (19,92 eV), ce qui correspond à 13H avec une longueur d'onde laser pilote de 800 nm, avec une intensité harmonique de deux ordres de grandeur supérieure à la harmoniques voisines. Une amélioration similaire a été observée dans l'étain LAP à 47 nm (26,3 eV), ce qui correspond à 17H avec une longueur d'onde laser de 800 nm (Figure F-1) [7].

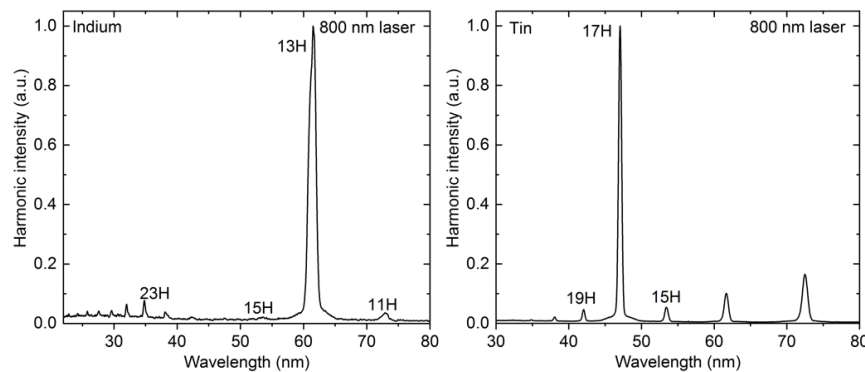


Figure F-1 Spectre HHG de l'indium et de l'étain LAP montrant RH.

Des études approfondies ont montré que les charges d'espace uniques de l'étain et de l'indium présentent une forte transition électronique avec une force d'oscillation élevée à proximité de la longueur d'onde RH. Par exemple, l'ion Sn^+ possède une transition $4d^{10} 5s^2 5p\ ^2P_{3/2} \rightarrow 4d^9 5s^2 5p^2\ (^1D)\ ^2D_{5/2}$ à 26,27 eV (47,2 nm) avec une force d'oscillation élevée de 1,52 [8]. Il a été également démontré que l'ion In^+ possède une transition de $4d^{10} 5s^2\ ^1S_0 \rightarrow 4d^9 5s^2 5p\ (^2D)\ ^1P_{1/2}$ à 19,92 eV (~ 62,24 nm) avec une force d'oscillateur élevée de 1,11 [9]. Les RH de l'étain et de l'indium sont

capables de générer des harmoniques brillantes ayant des valeurs μJ d'énergies harmoniques [7,10]. Outre l'indium et l'étain, le chrome, le manganèse et l'antimoine sont quelques-uns des autres matériaux qui montrent également le phénomène de RH.

8.3 Mécanisme de HHG

Le principe de la génération de HHG peut être expliqué par le modèle de trois étapes. Ce modèle consiste de mouvement semi-classique des électrons de la couche de valence d'un atome ou d'un ion sous l'influence du champ intense d'une impulsion laser ultracourte. [11]. Ces étapes constituent par l'ionisation des électrons par l'effet tunnel (TI) dans la couche de valence, ses accélérations continuent en suivant d'une transition radiative vers l'état fondamental initial émettant le XUV. Le diagramme schématique illustrant le modèle en trois-étapes est illustré à la Figure F-2.

L'énergie maximale des photons maximale $\hbar\Omega_{max}$ émise au cours de HHG, est également appelée la coupure harmonique (ou harmonic cut-off), qui est donnée par l'équation suivante.

$$\hbar\Omega_{max}[\text{eV}] = I_p[\text{eV}] + 29.61 \times I_L[10^{14} \text{ W/cm}^2] \times \lambda^2[\mu\text{m}]$$

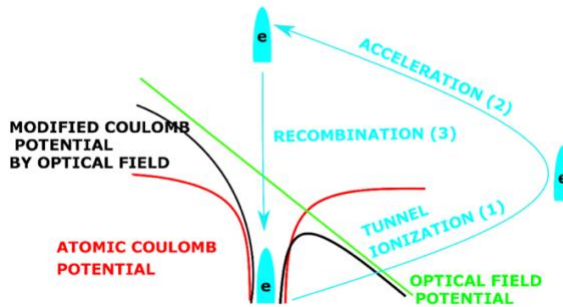


Figure F-2 Le diagramme schématique du modèle en trois-étapes pour le mécanisme de HHG.

Comme susmentionné dans les sections précédentes, dans de nombreux LAP, l'intensité de la première harmonique est d'un ordre supérieur de grandeur à celui de ses harmoniques voisines. Le modèle en trois-étapes ne peut pas expliquer ce phénomène car il ne considère pas l'influence des états électroniques qui pourraient perturber le mouvement de l'électron ionisé par effet tunnel lors de l'accélération sous l'influence du champ électrique. Lorsqu'une énergie de transition électronique à haute intensité d'oscillateur appropriée correspond à l'ordre des harmoniques à une longueur d'onde laser donnée, la génération RH a lieu avec une amélioration de l'intensité par rapport aux harmoniques voisines. Par exemple, les ions Sn^+ montrent une RH à 26,3 eV en raison de la transition de force d'oscillateur élevée $4\text{d}^{10} 5\text{s}^2 5\text{p } ^2\text{P}_{3/2} \rightarrow 4\text{d}^9 5\text{s}^2 5\text{p}^2 (^1\text{D}) ^2\text{D}_{5/2}$ [7]. De même,

les In^+ montrent également une génération de RH à 19,92 eV due à la transition $4\text{d}^{10} \ 5\text{s}^2 \ ^1\text{S}_0 \rightarrow 4\text{d}^9 \ 5\text{s}^2 \ ^2\text{D}$ ${}^1\text{P}_{1/2}$ [12]. Un modèle en quatre-étapes a été introduit pour expliquer le phénomène des RH dans les LAP. Dans ce modèle, les deux premières étapes sont les mêmes que dans le modèle en trois-étapes, c'est-à-dire TI de l'électron de valence et son accélération dans le continuum [13]. La troisième étape, cependant, implique la capture résonante de l'électron ionisé par effet tunnel dans l'état d'auto-ionisation (AIS). Autrement dire un état discret intégré au continuum, qui est suivi par la quatrième étape impliquant la transition radiative de l'AIS à l'état fondamental initial émettant des RH.

8.4 Configuration Expérimentale pour HHG

Le schéma de principe du montage expérimental pour le HHG de LAP est illustré à la Figure F-3. Un système laser Ti:saphir amplifié (210 picosecondes, 100 Hz, 800 nm) a été divisé en deux faisceaux en utilisant un séparateur de faisceau 30/70. Ainsi, 30 % du faisceau incident (pré-impulsion) s'est concentré sur une cible solide (montée sur une translation platine XYZ) avec une énergie ajustée entre 1,0-2,0 mJ, correspondante d'une intensité de $\sim 10^{10} \text{ W cm}^{-2}$ pour la formation LAP.

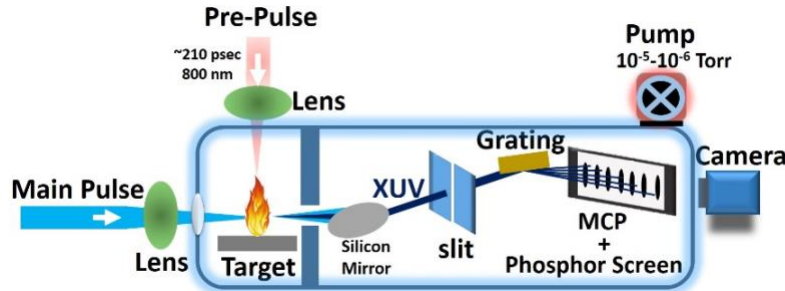


Figure F-3 Schéma de principe du montage expérimental pour le HHG du LAP.

Le délai optique entre la pré-impulsion et l'impulsion principale au niveau de la cible solide a été choisi pour maximiser le flux XUV, avec une valeur typique de 25-80 ns, la valeur exacte étant différente pour les différentes cibles solides utilisées. Le faisceau à 70 %, appelé impulsion principale, est l'impulsion fs comprimée. Cette impulsion principale pourrait être la sortie compressée amplifiée du système laser 10 Hz ou 100 Hz basé sur l'oscillateur laser Ti:saphir. L'impulsion principale pourrait également être la sortie amplifiée de notre système laser à amplificateur paramétrique optique (OPA) fonctionnant dans la longueur d'onde de l'infrarouge moyen. Pour une expérience utilisant des impulsions laser de 400 nm, la sortie compressée de 800 nm du laser Ti:saphir est doublée en fréquence à l'aide d'un cristal de Beta Barium Borate (BBO)

et séparée de la longueur d'onde laser colinéaire de 800 nm à l'aide d'un miroir dichroïque, générant des impulsions laser de 400 nm avec une durée d'impulsion de 57 fs. De même pour les expériences avec des longueurs d'onde dans le proche-infrarouge (860-940 nm), la sortie infrarouge est amplifiée par l'OPA accordable qui est à son tour doublée en fréquence par un cristal BBO en filtrant avec un miroir dichroïque. L'impulsion XUV générée et l'impulsion laser co-propageante sont divisées à l'aide d'un miroir en silicium placé à un angle de Brewster de l'impulsion principale, reflétant ainsi uniquement l'impulsion XUV dans le spectromètre XUV. Les rayons X sont dispersées selon les fréquences par un spectromètre qui comprend une fente verticale fixe et un réseau XUV cylindrique à champ plat (Hitachi, 1200 lignes/mm), une micro-canaux plate (MCP) et un écran phosphorescent. Les harmoniques sont capturées à l'aide d'une caméra CMOS 16 bits (modèle PCO-edge, PCO AG, Allemagne). La cible solide, le miroir de silicium et le spectromètre XUV sont maintenus à l'intérieur d'un vide de 10^{-5} - 10^{-6} torr.

8.5 Génération de RH dans le Régime d'ionisation Multiphotonique

Dans ce section, nous démontrons le nouveau phénomène de génération de RH dans le régime d'ionisation multiphotonique (MPI) jusqu'alors inexploré. À ce jour, toutes les expériences sur la génération de RH intense ont été réalisées dans le régime d'ionisation tunnel (TI), où le mécanisme d'ionisation électronique se déroule selon le phénomène du TI, où l'électron de la couche de valence d'un atome ou d'un ion s'échappe en raison de la suppression du potentiel de Coulomb retenant l'électron. Cependant, dans certaines conditions, le champ laser n'est pas capable de supprimer le champ de Coulomb de l'atome/ion, et l'ionisation électronique a lieu en raison de l'absorption multiphotonique par l'atome, phénomène connu sous le nom d'ionisation multiphotonique. Dans ce contexte, un paramètre important est le paramètre de Keldysh, défini comme $\gamma = \sqrt{I_p/2U_p} = 0.231\sqrt{I_p/I\lambda^2}$ (où I_p est l'énergie d'ionisation en eV, I est l'intensité laser en unités de 10^{14} W cm $^{-2}$, λ est la longueur d'onde du laser en μm , et U_p est l'énergie pondéromotrice en eV, et est donnée par équation $U_p = 9.34 I\lambda^2$). Le paramètre de Keldysh détermine globalement deux régimes d'interaction laser-matière. Le régime MPI pour les valeurs de $\gamma > 1$ et le régime TI pour les valeurs de $\gamma < 1$. Par conséquent, le régime de TI implique une grande U_p par rapport à I_p et vice versa pour MPI.

8.5.a Génération de RH avec des Longueurs d'onde Laser dans le Proche Infrarouge à Partir de Ga⁺

Nous utilisons les impulsions laser ayant différentes longueurs d'onde dans le proche infrarouge entraînant le gallium LAP pour HHG, et les spectres HHG générés sont illustrés à la Figure F-4. Les impulsions laser générées dans le proche infrarouge avec une durée d'impulsion de 40 fs et une énergie d'impulsion de 1,5 mJ sont focalisées sur le LAP à une intensité de $1,7 \times 10^{14} \text{ W cm}^{-2}$. Le Ga⁺ ($I_p=20,52 \text{ eV}$) présente une forte résonance dans la section efficace de photoionisation (PICS) avec une magnitude de 300 Mbar centrée à 21,9 eV, correspondant à la forte transition radiative $3d^{10}4s^2 \text{ }^1S_0 \rightarrow 3d^94s^24p \text{ }^3P_1$ [14]. Le paramètre Keldysh γ à 860 nm est de 0,935. L'état $3d^94s^24p \text{ }^3P_1$ correspond à l'AIS de Ga⁺ et la transition électronique de l'AIS à l'état fondamental $3d^{10}4s^2 \text{ }^1S_0$ est résonante avec 15 photons de champ laser de 860 nm. On s'attend à ce qu'une amélioration ou une résonance dans le PICS puisse entraîner une augmentation de l'intensité harmonique à l'énergie du photon résonant [15], et nous voyons une RH intense à la 15e harmonique (15H).

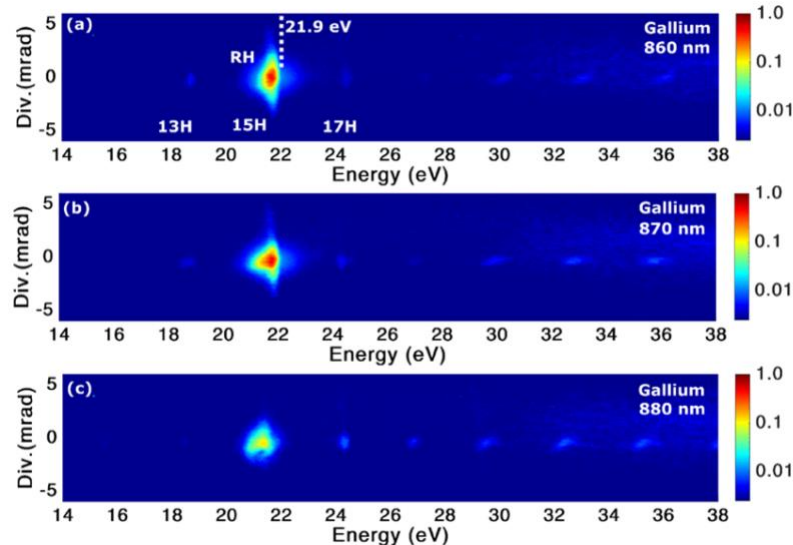


Figure F-4 Les spectres de HHG générés à partir de Ga+, éclairé par les laser de longueurs d'onde de (a) 860 nm, (b) 870 nm et (c) 880 nm. La résonance $3d^{10}4s^2 \text{ }^1S_0 \rightarrow 3d^94s^24p \text{ }^3P_1$ de Ga⁺ à une énergie de 21,9 eV est de 15 photons résonnant avec la longueur d'onde de 860 nm, résultant en une émission RH intense à 15H. L'intensité RH diminue lorsque la longueur d'onde du laser est éloignée de la résonance, comme indiqué en (b) et (c). L'intensité laser utilisée pour générer chaque spectre harmonique est de $1,7 \times 10^{14} \text{ W cm}^{-2}$.

Nous définissons le taux d'augmentation (ou ER, pour "Enhancement ratio") observé expérimentalement pour RH avec l'équation $ER = 2I_q/(I_{q-2} + I_{q+2})$, où I_q est l'intensité intégrée de RH avec un ordre de q. A une longueur d'onde laser de 860 nm, le ER observé est de 136.

8.5.b Génération de RH à Partir de Ga^+ avec une Longueur d'onde Laser de 400 nm

Pour étudier la réponse de RH de Ga^+ à des paramètres Keldysh plus élevés, nous avons utilisé une longueur d'onde laser de commande plus courte de 400 nm. La Figure F-5 montre RH intense observée à une intensité laser de $1,6 \times 10^{14} \text{ W cm}^{-2}$. La résonance de 21,9 eV résonne à 7 photons avec le photon laser de commande de 400 nm, générant un 7H intense. Les valeurs de Up et I_p sont respectivement de 2,39 eV et 20,52 eV, ce qui donne un paramètre Keldysh de 2,07. La génération HHG a lieu dans le régime MPI.

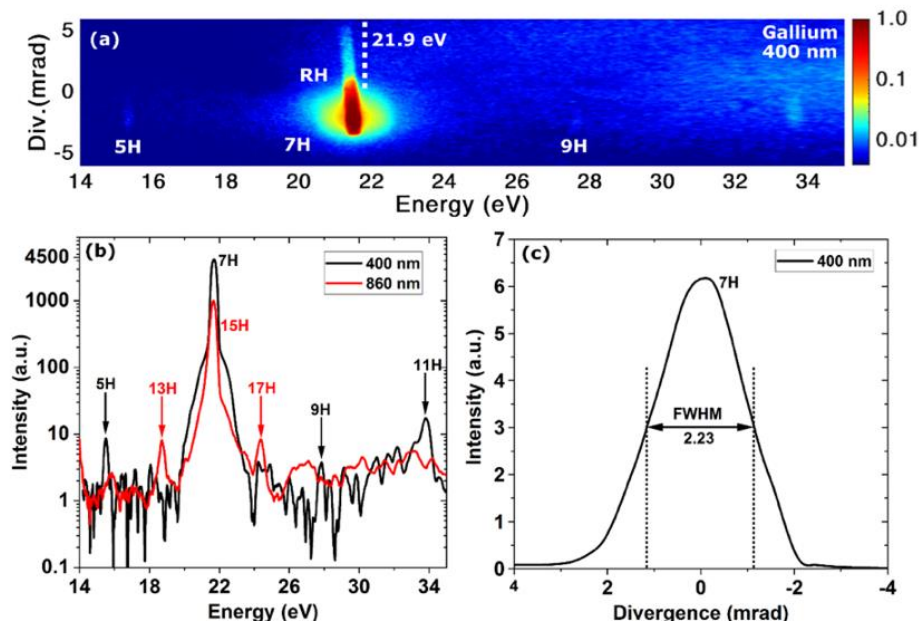


Figure F-5 Les spectres HHG générés à partir de Ga^+ , utilisant (a) une longueur d'onde laser de 400 nm, montrant une RH intense proche de 21,9 eV, et d'autres harmoniques non résonantes très faibles par rapport à la RH. (b) Le profil de ligne verticalement intégré de RH de Ga^+ en utilisant une longueur d'onde laser de 400 nm et 860 nm. L'intensité maximale de RH de Ga^+ avec une longueur d'onde laser de 400 nm est observée comme étant 4,5 fois plus forte que la RH avec une longueur d'onde laser de 860 nm, plus forte en raison du faible nombre de photons laser requis pour la résonance avec l'AIS utilisant l'ancienne longueur d'onde. (c) La divergence FWHM de RH est de 2,23 mrad, indiquant la nature cohérente de l'émission RH. L'intensité laser utilisée pour générer un spectre harmonique à 400 nm et 860 nm de longueur d'onde est respectivement de $1,6 \times 10^{14} \text{ W cm}^{-2}$ et $1,7 \times 10^{14} \text{ W cm}^{-2}$.

L'ER observé en utilisant une longueur d'onde laser de 400 nm est de 714. La valeur ER la plus élevée signalée jusqu'à présent provient du LAP d'indium générant une RH intense avec un ER d'environ 100 [16]. Par conséquent, dans notre expérience l'ER de 714 observé sous régime MPI est la valeur la plus élevée signalée jusqu'à présent en utilisant la technique LAP, faisant du gallium LAP une source de RH intense avec une monochromatique sans précédent à partir d'une source harmonique d'ordre élevé.

8.5.c Comparaison de l'intensité RH de Ga^+ avec D'autres LAP

La comparaison de l'intensité d'harmonique du gallium, du graphite et de l'étain LAP est illustrée à la Figure F-6 avec les paramètres laser correspondants répertoriés dans le Tableau F.1. Le délai optique entre la pré-impulsion et l'impulsion principale a été maintenu à 35 ns, 55 ns et 70 ns pour le graphite, le gallium et l'étain LAP fournissant respectivement le flux harmonique maximal. L'intensité laser à chaque LAP est d'environ $1,6 \times 10^{14} \text{ W cm}^{-2}$.

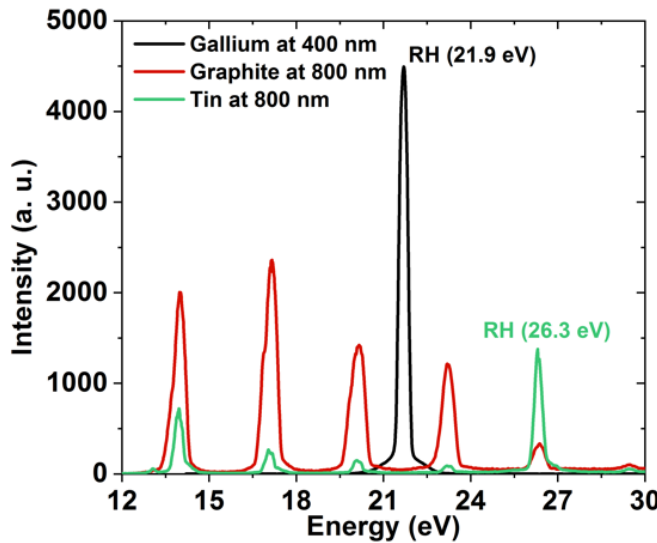


Figure F-6 La comparaison de l'intensité RH de Ga^+ avec d'autres LAP connus pour générer des harmoniques intenses.

RH de Ga^+ à 21,9 eV représente une intensité de crête 3,3 fois supérieure à celle de RH de l'étain, en démontrant RH de Ga^+ comme source potentielle d'énergie harmonique multi- μJ . Étant donné que LAP de graphite LAP et RH de l'étain LAP à 26,3 eV ont démontré des énergies harmoniques de niveau μJ au niveau 10^{-4} CE [17], la comparaison relative de l'intensité RH de Ga^+ l'établit comme une source potentielle de quasi-monochromatique (QM)-XUV avec une énergie d'impulsion multi- μJ .

Tableau F-1 Les paramètres laser utilisés pour HHG de différents LAP

Cible	d'impulsion laser (mJ)	durée d'impulsion (fs)	diamètre focal (μm)	emplacement du point focal derrière la surface cible (cm)	intensité laser au LAP (W cm^{-2})
Gallium	1.3	57	40	1.0	1.60×10^{14}
Graphite	1.2	40	90	1.1	1.62×10^{14}
Tin	1.4	40	90	1.2	1.68×10^{14}

8.5.d Mécanisme de Génération de RH dans le Régime MPI

Le mécanisme de génération de RH dans le régime MPI peut être similaire au modèle en quatre-étapes applicable pour la génération de RH dans le régime TI, incorporant la transition ascendante de résonance multiphotonique de l'état fondamental à l'AIS, au lieu de capturer l'électron ionisé tunnel par l'AIS dans le continuum. La transition descendante radiative à un photon de l'AIS vers l'état fondamental émettra des rayons XUV avec une intensité proportionnelle à l'amplitude de la transition descendante. Cela formera essentiellement un modèle en deux étapes avec l'inclusion de l'AIS [18] [19] [20]. L'intensité RH et l'ER plus élevés en régime MPI par rapport au régime TI pourraient être attribués à l'étalement du paquet d'ondes électronique après photoionisation en régime TI : le paquet d'ondes s'étend à la deuxième étape du modèle à quatre-étapes, qui remplit l'AIS avec une probabilité relativement faible. ; cet étalement est absent dans le régime MPI où l'AIS est alimenté directement à partir de l'état fondamental.

8.6 Génération d'harmoniques Résonantes juste en Dessous du Seuil d'ionisation

Ici, nous démontrons le nouveau phénomène d'amélioration harmonique de résonance pour un seul ordre harmonique juste en dessous du seuil d'ionisation (I_p). Il est révélé que ce type d'harmonique de résonance est observé en raison du chevauchement de l'AIS habillé avec le nuage de Rydberg. Cette nouvelle méthode est utile pour générer une lumière XUV cohérente et brillante à partir d'états atomiques et moléculaires qui ne participent généralement pas à une émission harmonique intense, comme les états de Rydberg.

8.6.a HHG de In^+ avec Longueur d'onde Laser Bicolore 800+400 nm

La Figure F-7 montre le spectre harmonique enregistré à partir de In^+ en utilisant une configuration HHG bicolore à un champ de conduite de 800 nm.

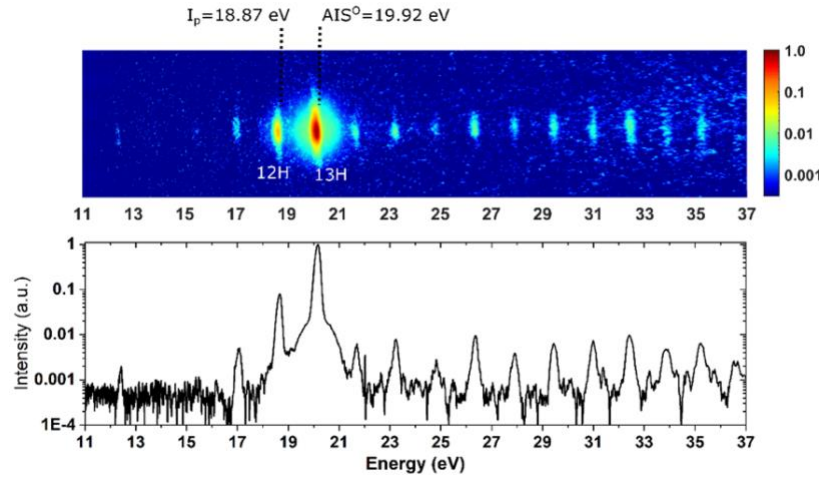


Figure F-7 Spectre HHG généré à partir d' In^+ avec un laser bicolore 800+400 nm.

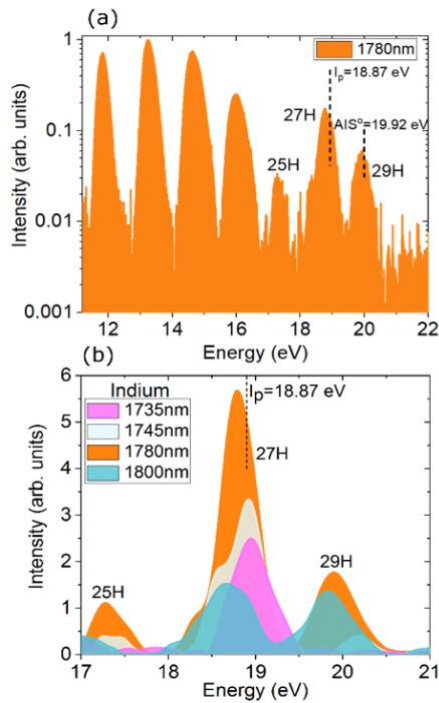


Figure F-8 **(a)** Spectre harmonique d'ordre élevé généré à partir d' In^+ à l'aide d'impulsions laser d'entraînement centrées à 1780 nm et d'une intensité laser d'environ $4,3 \times 10^{14} \text{ W cm}^{-2}$. L' I_p de In^+ est de 18,87 eV, ce qui correspond à 27 photons de résonance avec le photon laser de pilotage de 1780 nm, et le $4d^9 5s^2 5p\ (^2D)\ ^1P_1$ AIS° de In^+ est situé à 19,92 eV. **(b)** Le changement de l'intensité 27H lorsque la longueur d'onde du laser d'entraînement est éloignée de la longueur d'onde du laser résonnant à 1780 nm.

Ce spectre contient des harmoniques paires et impaires. Dans l'indium LAP, In^+ est l'espèce active responsable de HHG. I_p de In^+ est de 18,87 eV, ce qui correspond à 12 photons de résonance avec la longueur d'onde du laser de 800 nm. Comme on peut le voir clairement sur la Figure F-7, il y a une amélioration de l'intensité à 13H selon le modèle en quatre-étapes bien connu, en raison de $4d^9\ 5s^2\ 5p\ (^2D)\ ^1P_1\ \text{AIS}^o$ existe à 19,92 eV au-dessus de l'état fondamental $4d^{10}5s^2$ de In^+ . Cependant, il est surprenant de constater que, le 12H, qui est l'ordre harmonique unique des harmoniques inférieurs au seuil (BTH), présente également une amélioration de l'intensité par rapport aux harmoniques voisines.

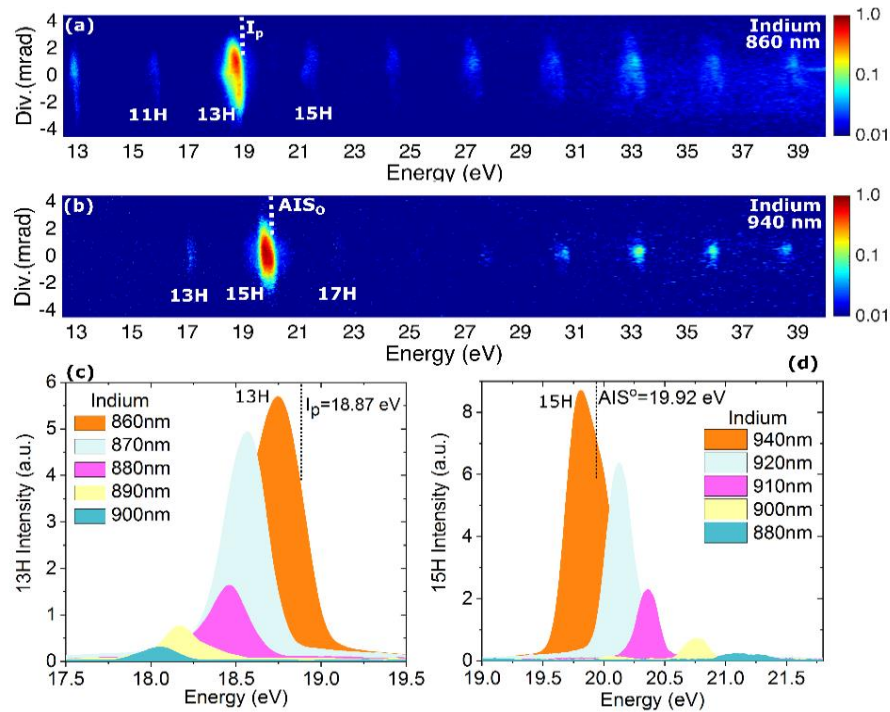


Figure F-9 Spectre harmonique d'ordre élevé généré à partir de In^+ **(a)** à l'aide d'impulsions laser de commande avec une longueur d'onde centrale de 860 nm et **(b)** à l'aide d'impulsions laser de commande avec une longueur d'onde centrale de 940 nm, les deux à une intensité de crête de $\sim 1,5 \times 10^{14} \text{ W cm}^{-2}$. L'IP de In^+ est de 18,87 eV, ce qui correspond à 13 photons de résonance avec le photon laser de commande de 860 nm, et le $4d^9\ 5s^2\ 5p\ (^2D)\ ^1P_1\ \text{AIS}^o$ de In^+ à 19,92 eV est de 15 photons de résonance avec le photon laser de commande de 940 nm. **(c)** Le changement de l'intensité 13H lorsque la longueur d'onde du laser d'entraînement est éloignée de la longueur d'onde du laser de résonance de 860 nm. L'intensité de crête ER observée pour le 13H est de 18. **(d)** Le changement de l'intensité du 15H lorsque la longueur d'onde du laser d'entraînement est éloignée de la longueur d'onde du laser de résonance de 940 nm. Le pic d'intensité RE observé pour le 15H est de 38.

8.6.b HHG de In⁺ avec Longueurs d'onde Laser Accordables dans le moyen et le Proche Infrarouge

Dans la Figure F-8(a), nous représentons les spectres HHG de In⁺ en utilisant des impulsions motrices avec une longueur d'onde centrale à 1780 nm. L'I_p de In⁺ est de 18,87 eV, ce qui correspond à 27 photons de résonance avec une longueur d'onde à 1780 nm. Comme on peut le voir, la 27e harmonique (27H), qui est l'ordre BTH simple, est générée avec une amélioration de l'intensité par rapport aux harmoniques voisines.

Nous avons réduit l'ordre de résonance multiphotonique pour Ip à 13 photons en utilisant une longueur d'onde laser de 860 nm, augmentant encore l'intensité du BTH unique. Le spectre HHG correspondant est représenté sur la Figure F-9(a). Le 13H de In+ est à nouveau généré avec une croissance de l'intensité par rapport aux harmoniques voisines. Sur la Figure F-9(b), nous montrons le spectre HHG généré à partir de In+ en utilisant des impulsions avec une longueur d'onde centrale de 940 nm. L'AIS^o 4d⁹ 5s² 5p (²D) ¹P₁ de In⁺ à 19,92 eV résonne à 15 photons avec la longueur d'onde du laser de commande de 940 nm [7]. Cet AIS^o a une partie impaire, qui est opposée à la parité de l'état fondamental 4d¹⁰ 5s² ¹S₀ de In⁺, et permet donc une transition radiative à un photon de force d'oscillateur élevée de l'AIS^o à l'état fondamental [9]. La résonante 15H est générée selon le modèle en quatre-étapes bien connu [21] [22].

8.6.c HHG de Ga⁺, Sn⁺ et Cr⁺ avec des Longueurs d'onde Laser Accordables dans le Proche Infrarouge

En dehors de In+, une autre espèce avec l'I_p et une AIS située à proximité immédiate est Ga⁺. L'I_p de Ga⁺ à 20,52 eV est situé à proximité immédiate de l'AIS^e 3d¹⁰4p5p (¹S) à 21,88 eV. Avec le photon laser d'entraînement de 800 nm, l'AIS^e I_p et 3d¹⁰4p5p (¹S) de Ga⁺ est à 13 photons et 14 photons résonnant, respectivement, réalisant une résonance multiphotonique avec le photon laser d'entraînement simultanément. Comme le montre la Figure F-10(a), nous observons une amélioration de l'intensité de résonance pour 13H, qui est le seul BTH dans Ga⁺. Ceci est similaire à l'amélioration harmonique à un seul BTH observée dans In+, ce qui confirme l'importance de la présence d'AIS et d'I_p à proximité l'un de l'autre pour générer un seul BTH intense.

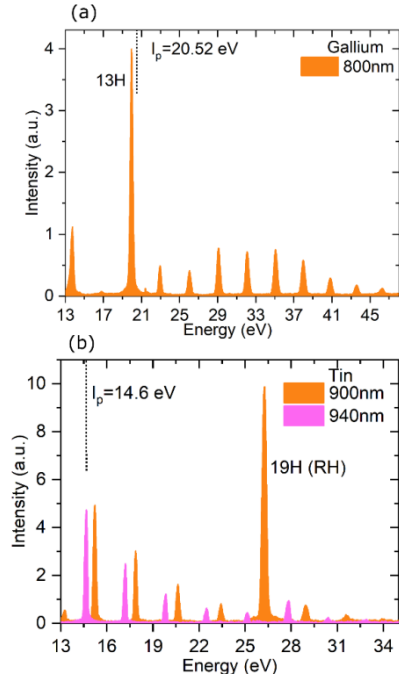


Figure F-10 **(a)** Le spectre harmonique d'ordre élevé généré à partir de Ga^+ à 800 nm de longueur d'onde laser. L' I_p de Ga^+ à 20,52 eV est à 13 photons de résonance avec une longueur d'onde du laser de 800 nm. La croissance de résonance de 13H, qui est le seul BTH, est observée. **(b)** Le spectre harmonique d'ordre élevé généré à partir de Sn^+ à 900 nm et 940 nm de longueur d'onde laser. L' I_p de Sn^+ à 14,6 eV est à 11 photons de résonance avec la longueur d'onde du laser de commande de 940 nm. Aucune amélioration résonnante du single-BTH n'est observée dans Sn^+ . Le renforcement de la résonance 19H du Sn^+ à la longueur d'onde de 900 nm résulte de la transition résonante d'une force d'oscillation élevée de l'état fondamental de $4d^9\ 5s^2\ 5p^2\ (^1\text{D})\ ^2\text{D}_{5/2}\ \text{AIS}^e$ à 26,27 eV dans l'état fondamental $4d^{10}5s^25p\ ^2\text{P}_{3/2}$, avec le mécanisme de génération comme selon le modèle en quatre-étapes.

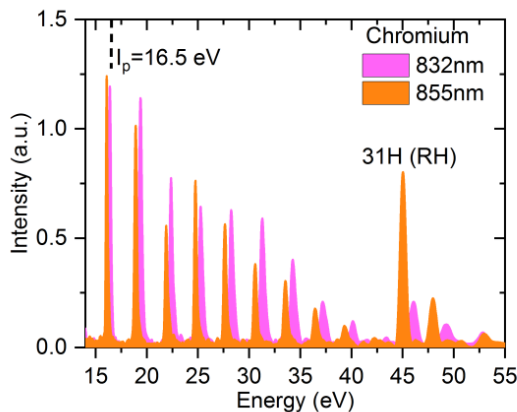


Figure F-11 Le spectre harmonique d'ordre élevé généré à partir de Cr^+ à 855 nm et 832 nm de longueur d'onde laser. L' I_p de Cr^+ à 16,5 eV est de résonance de 11 photons avec la longueur d'onde du laser de commande de 855 nm, mais aucune amélioration d'intensité pour le BTH simple n'est observée.

Pour vérifier si l'amélioration de RH pour le BTH unique existe pour chaque LAP lorsque la résonance multiphotonique avec le I_p est atteinte, nous avons utilisé l'étain LAP comme support non linéaire pour le HHG car il n'existe pas d'AIS approprié à proximité immédiate d' I_p . Dans l'étain LAP, Sn^+ répond en tant qu'espèce active pour HHG et a un I_p à 14,6 eV, qui résonne à 11 photons avec le photon laser à 940 nm [23]. La Figure F-10(b) montre le spectre harmonique de Sn^+ qui ne montre aucune amélioration harmonique près de I_p .

8.7 Génération d'harmoniques Résonantes à partir d'atomes Neutres de Manganèse

Ici, nous démontrons le HHG du LAP produite à partir de manganèse, un métal de transition, en utilisant une impulsion laser ultracourte à cycles multiples et à quelques cycles (~ 2 cycles) avec une longueur d'onde de 1,82 m. Dans toutes les expériences HHG précédentes utilisant LAP comme support non linéaire, les harmoniques d'ordre élevé sont générées à partir des espèces ioniques. Cependant, dans nos expériences avec le manganèse LAP, nous démontrons que les harmoniques d'ordre élevé sont principalement générés à partir d'atomes neutres (avec un potentiel d'ionisation de 7,4 eV)). Nos résultats ouvrent la possibilité de faire progresser la technique d'ablation laser pour étudier la dynamique des atomes neutres à faible potentiel d'ionisation.

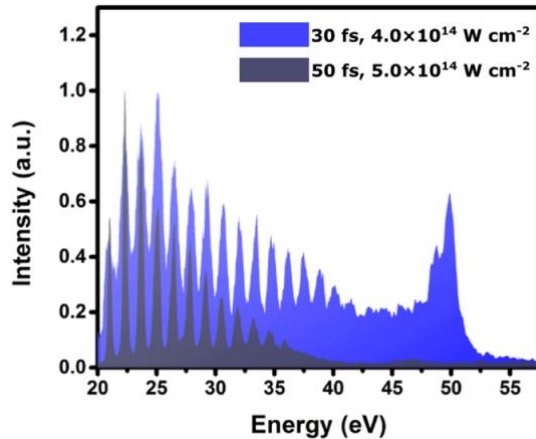


Figure F-12 Les spectres harmoniques observés à partir d'un LAP de manganèse ayant subi par un laser ablation avec une durée de 30 fs (spectre bleu) et 50 fs (spectre noir), une longueur d'onde de 1,82 μm et des intensités laser d'environ $4,0 \times 10^{14} \text{ W cm}^{-2}$ et $\sim 5 \times 10^{14} \text{ W cm}^{-2}$, respectivement. Il a été révélé qu'avec le champ d'attaque de 50 fs, des harmoniques d'ordre élevé sont générés à partir de manganèse neutre. Cependant, les harmoniques de GAR du manganèse neutre ne sont pas observées avec le champ d'entraînement de 50 fs. Les harmoniques de GAR apparaissent pour le champ moteur avec une durée d'impulsion de 30 fs.

Le Mn neutre et le Mn⁺ contiennent tous deux une résonance autoionisante géante (GAR) autour de 50 eV, qui est principalement due aux transitions dipolaires 3p-3d [24]. Le rôle de ce GAR dans HHG est étudié en faisant varier la durée d'impulsion du champ moteur, de 50 fs à 12 fs. La Figure F-12 montre les spectres harmoniques enregistrés à l'aide de champs de commande avec des durées d'impulsion de 50 fs (spectre noir, intensité laser de commande $\sim 5 \times 10^{14} \text{ W cm}^{-2}$) et 30 fs (spectre bleu, intensité laser de commande $\sim 4,0 \times 10^{14} \text{ W cm}^{-2}$). Dans ce spectre, malgré l'intensité laser d'entraînement relativement plus élevée, des harmoniques d'ordre élevé allant jusqu'à 36 eV seulement sont observées pour le champ d'entraînement de 50 fs. Cela contraste fortement avec les spectres harmoniques enregistrés avec des champs de commande de 30 fs et 12 fs. À partir de la coupure harmonique d'ordre élevé, nous pouvons trouver les espèces soumises à une ablation laser responsables de HHG. La coupure harmonique d'ordre élevé peut être estimée avec le modèle semi-classique en trois-étapes $E_{\text{cut-off}} = I_p + 3.17U_p = I_p[eV] + 29.61 \times I_L[10^{14} \text{ W/cm}^2] \times \lambda^2[\mu\text{m}]$. (où I_p , U_p , I et λ sont le potentiel d'ionisation, l'énergie pondéromotrice, entraînant l'intensité du laser et la longueur d'onde, respectivement). Les calculs pour $=1,8 \mu\text{m}$ montrent que des harmoniques d'ordre élevé avec un champ de commande de 50 fs sont générées à partir de manganèse neutre. Cependant, les harmoniques de GAR ne sont pas générées avec le champ de conduite multicycle IR moyen.

Pour les harmoniques d'ordre élevé du LAP de manganèse par ablation laser, nous trouvons une différence dans la coupure lorsque le proche IR multicycle ($0,8 \mu\text{m}$; énergie ~ 8 à 25 mJ) [25] et l'IR moyen ($1,8 \mu\text{m}$; énergie ~ 1 à 5 mJ) des champs d'entraînement sont utilisés. Avec le champ de commande proche IR, des harmoniques d'ordre élevé jusqu'à 156 eV ont été observés [25,26], alors qu'avec le laser IR moyen, même à des intensités de champ de commande similaires, la coupure harmonique a été observée comme étant faible (36 eV). Cette différence peut s'expliquer par le fait qu'avec les champs proches de l'IR, les harmoniques d'ordre élevé sont principalement générées à partir d'espèces ioniques [25].

Étant donné que le GAR du manganèse possède d'une large bande [27], le spectre harmonique a été enregistré avec peu de champ de conduite cyclique pour voir l'effet de RH sur une large gamme d'énergie, et le spectre correspondant est illustré à la Figure F-14. Dans ce spectre, un spectre à large bande continue est observé avec une augmentation significative de l'intensité dans la zone énergétique de 49 eV à 53 eV, ce qui correspond au GAR du manganèse neutre [24].

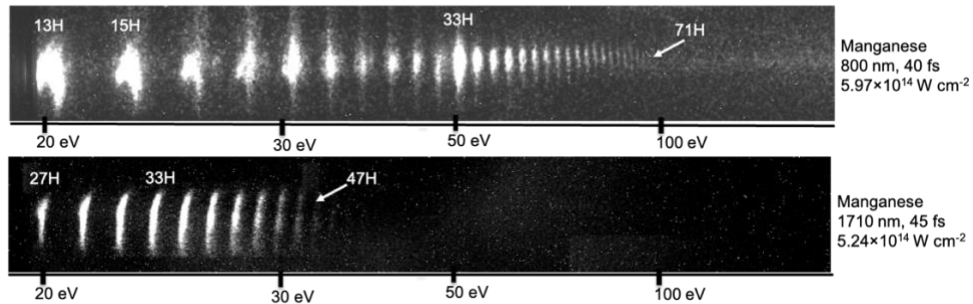


Figure F-13 Spectre d'harmoniques d'ordre élevé avec longueurs d'onde ; (a) 0,8 µm (énergie d'impulsion principale = 2,5 mJ, durée d'impulsion = ~40 fs, intensité de crête = $5,97 \times 10^{14} \text{ W cm}^{-2}$) et (b) 1,71 µm (énergie MP = 6 mJ, durée d'impulsion = 45 fs, intensité de crête = $5,24 \times 10^{14} \text{ W cm}^{-2}$).

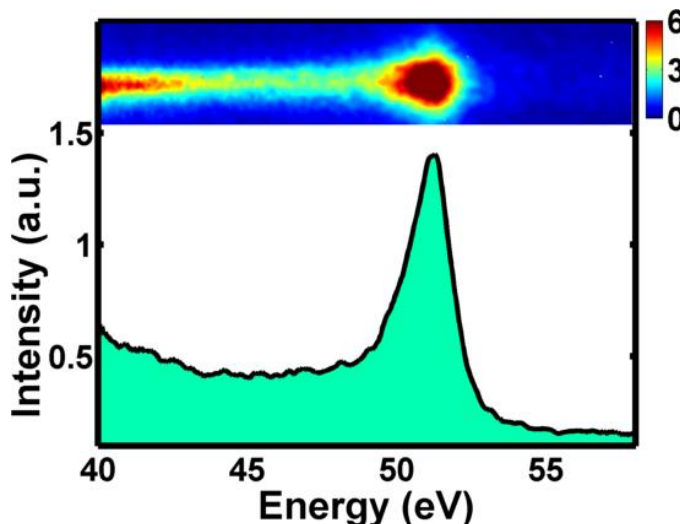


Figure F-14 Le spectre HHG enregistré avec un champ laser à quelques cycles à une intensité laser d'environ $4,0 \times 10^{14} \text{ W cm}^{-2}$. Dans ce spectre, un continuum à large bande est observé. L'intensité harmonique est élevée aux énergies de 49 eV à 53 eV. L'augmentation de l'intensité dans cette région d'énergie indique que ces harmoniques sont générées à partir du GAR du manganèse neutre.

8.8 Génération d'harmoniques Résonantes élevé par D'états Sn III

Pour résumer, nous avons étudié le HHG à partir d'étain par ablation laser à l'aide de lasers ultracourts avec des longueurs d'onde de 800 nm, 1750 nm et 1780 nm. Nous rapportons de multiples améliorations harmoniques dans la région XUV en raison de l'implication des transitions Sn III.

8.8.a HHG D'étain LAP Utilisant une Longueur d'onde Laser de 800 nm

Le spectre HHG généré à partir du LAP d'étain avec une longueur d'onde laser de 800 nm est illustré à la Figure F-15. À une longueur d'onde laser de 800 nm, la transition AIS $4d^{10}5s^25p\ ^2P_{3/2} \rightarrow 4d^95s^25p^2\ (^1D)\ ^2D_{5/2}$ de Sn II à 26,27 eV, qui a une grande force d'oscillateur de 1,52, est de 17

photons résonnants avec le photon laser d'entraînement [6]. Selon le modèle en quatre-étapes, 17H avec une augmentation significative de l'intensité par rapport aux harmoniques voisines est générée [23] [13].

Tableau F-2 Les différentes compositions de vecteurs propres à terme supérieur dans le couplage JJ pour la transition $4d^{10}5s^25p \rightarrow 4d^95s^25p^2$ de Sn III tirées des données publiées dans la référence [6]. Le ‘ fait référence au noyau (5/2, 1/2), ” au noyau (3/2, 1/2) et l'indice fait référence au total J.

Label	Ion	Transition	E (eV)	gf-value
\vec{a}	Sn III	$(1/2, 3/2)_2 \rightarrow (2'', 2)_3$	26.83	0.38
\vec{b}	Sn III	$(1/2, 3/2)_2 \rightarrow (2'', 2)_1$	27.14	0.20
\vec{c}	Sn III	$(1/2, 3/2)_1 \rightarrow (3', 2)_2$	28.33	0.51
\vec{d}	Sn III	$(1/2, 3/2)_2 \rightarrow (3', 2)_3$	28.48	0.84
\vec{e}	Sn III	$(1/2, 3/2)_2 \rightarrow (3', 2)_1$	28.80	0.33
\vec{f}	Sn III	$(1/2, 3/2)_2 \rightarrow (1'', 2)_2$	29.47	0.20

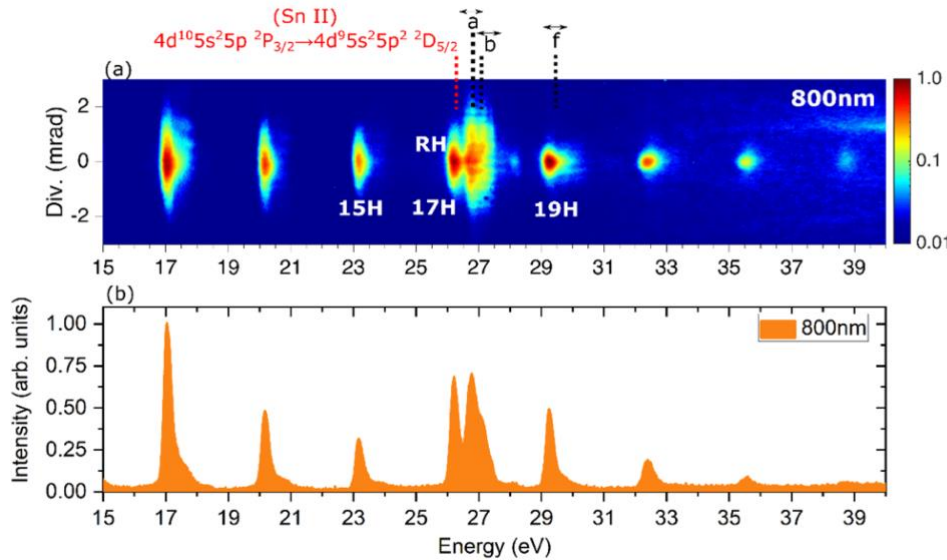


Figure F-15 Le spectre HHG généré à partir d'étain LAP (a) avec une longueur d'onde laser de 800 nm à une intensité laser de $7 \times 10^{14} \text{ W cm}^{-2}$. (b) Le tracé linéaire correspondant obtenu par intégration verticale du spectre HHG. Le 17H est généré selon le modèle à quatre-étapes en raison de la présence de l'AIS à 26,27 eV, identifié RH sur la figure. Le 17H est proche des transitions du Sn III à 26,83 eV et 27,14 eV (appelé \vec{a} et \vec{b} comme indiqué dans la Figure F-15(a) et dans le Tableau F-2). La division du 17H en plusieurs composants en raison de la proximité immédiate des transitions RH vers Sn III est une preuve claire de l'implication du Sn III dans le processus HHG.

Les transitions présentées \vec{a} et \vec{b} dans le Tableau F-2 sont à proximité immédiate du 17H, et sur la Figure F-15 pouvons donc également observer que l'ordre 17H est divisé en plusieurs composantes harmoniques. Ce dédoublement harmonique indique clairement l'implication de Sn III dans le mécanisme HHG. La transition étiquetée \vec{f} est proche de l'ordre 19H, et nous observons également que le rehaussement d'intensité pour le 19H est supérieur par rapport aux harmoniques voisines.

8.8.b HHG de l'étain LAP Utilisant des Longueurs d'onde de 1750 nm et 1780 nm

La Figure F-16(a) et (b) montrent respectivement les spectres harmoniques générés à partir du LAP par l'étain en utilisant une longueur d'onde laser de 1750 nm et 1780 nm, avec la même intensité de $5 \times 10^{14} \text{ W cm}^{-2}$. Nous observons de multiples améliorations d'intensité harmonique dans la gamme d'énergie entre 26 eV et 30 eV. À 1750 nm de longueur d'onde du laser de pilotage, la transition AIS $4d^{10}5s^25p\ 2P_{3/2} \rightarrow 4d^95s^25p^2\ (^1D)\ 2D_{5/2}$ de Sn II à 26,27 eV est de 37 photons en résonance avec le photon du laser de pilotage. Par conséquent, selon le modèle à quatre-étapes [13], l'ordre 37H est généré avec un rehaussement d'intensité par rapport au 35H voisin. Cependant, comme le montre la Figure F-16, une augmentation de l'intensité est également observée pour le 39H ainsi que le 41H.

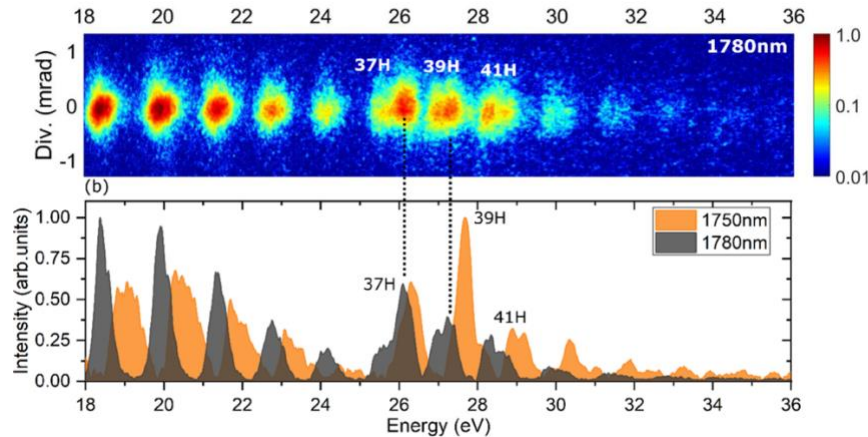


Figure F-16 Spectre de HHG généré à partir du LAP d'étain (a) en utilisant une longueur d'onde laser de pilotage de 1780 nm et (b) le tracé linéaire du spectre HHG en utilisant une longueur d'onde de laser de pilotage de 1780 nm et 1750 nm, tous deux à une intensité laser de pilotage de $5 \times 10^{14} \text{ W cm}^{-2}$. Le spectre de raies est obtenu en intégrant verticalement le spectre HHG. Des améliorations harmoniques multiples sont observées dans la région d'énergie entre 25 eV et 30 eV, et il existe de nombreuses transitions électroniques fortes dans cette gamme d'énergie, comme le montre le Tableau F-2.

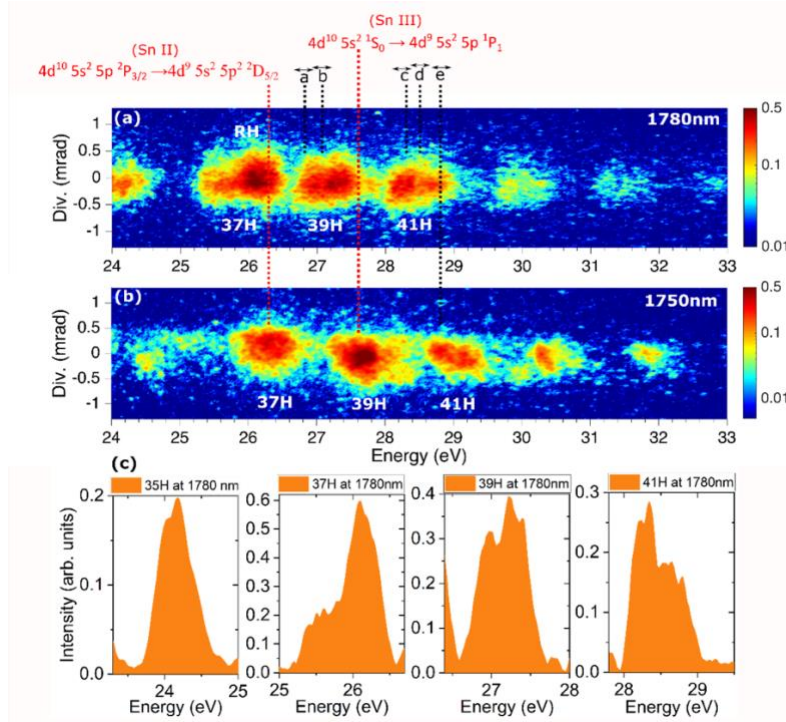


Figure F-17 La vue agrandie des spectres HHG générés à partir d'étain LAP dans la plage d'énergie entre 24 eV et 33 eV **(a)** en utilisant la longueur d'onde à 1780 nm et **(b)** à 1750 nm, respectivement. **(c)** Le profil de ligne verticalement intégré des ordres harmoniques 35H-41H générés à l'aide d'une longueur d'onde laser de pilotage de 1780 nm. Les multiples transitions électroniques fortes de Sn III sont présentes dans la plage entre 26 eV et 30 eV, comme indiqué dans le Tableau F-2, et les 39H et 41H améliorés ont des énergies de photons dans cette plage.

Les Figures F-17 (a) et (b) représentent la vue agrandie des spectres harmoniques afin de mieux comprendre les améliorations harmoniques. Les transitions électroniques diverses du Sn III sont marquées et identifiées dans les spectres harmoniques. Les ordres harmoniques améliorés sont situés dans la plage où se trouvent les transitions de Sn III.

8.8.c Diagramme des Niveaux d'énergie de Sn II et Sn III

Sur la Figure F-18, présente le diagramme des niveaux d'énergie de Sn II et Sn III pour expliquer le processus HHG dans l'étain LAP.

Sn II a une configuration à l'état fondamental $4d^{10}5s^25p\ ^2P_{3/2}$ et possède un AIS $4d^95s^25p^2\ ^2D_{5/2}$ situé à 26,27 eV. Cet AIS peut être excité de manière cohérente par une excitation multiphotonique résonnante avec le photon de laser. Résonance à 17 photons et 37 photons avec les longueurs d'onde laser de 800 nm et 1750 nm, respectivement. La transition radiative forte $4d^{10}5s^25p\ ^2P_{3/2} \rightarrow 4d^95s^25p^2\ (^1D)\ ^2D_{5/2}$ génère une RH selon le modèle à quatre-étapes [13]. Outre la transition de l'AIS à l'état fondamental initial du Sn II, une autre possibilité est la photoionisation de cet AIS à

partir de l'état 5s ou 5p produisant le Sn III, faisant atterrir le système dans l'état $4d^95s5p^2$ ou $4d^95s^25p\ ^1P_1$, respectivement. La transition $4d^{10}5s^2\ ^1S_0 \rightarrow 4d^95s^25p\ ^1P_1$ à 27,6 eV a une force d'oscillateur élevée de 0,87 et génère une harmonique intense comme le montre la Figure F-17(b) [28].

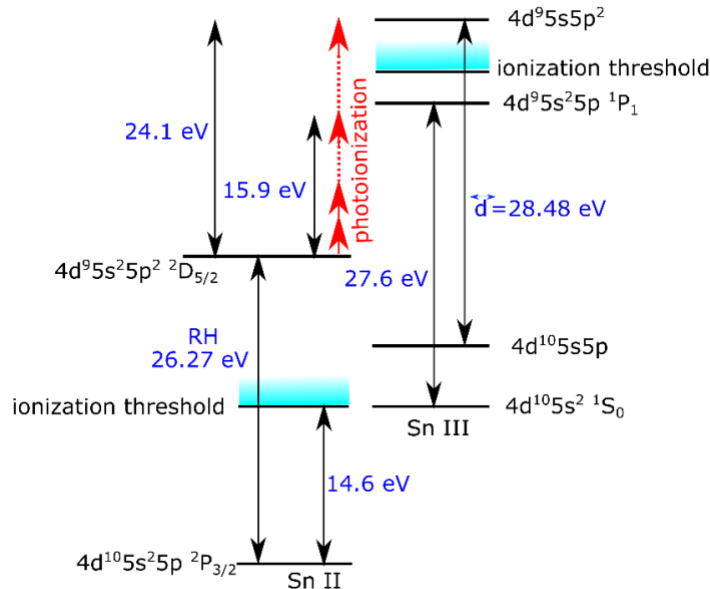


Figure F-18 Diagramme des niveaux d'énergie de Sn II et Sn III

Pour la transition $4d^{10}5s5p \rightarrow 4d^95s5p^2$, diverses compositions de vecteurs propres dans le couplage JJ situées dans la plage d'énergie entre 26 eV et 30 eV sont présentées dans le Tableau F-2. Comme le montre la Figure F-17, les multiples améliorations harmoniques observées se situent dans cette plage de transitions Sn III. Pour la transition Sn III $4d^{10}5s^2\ ^1S_0 \rightarrow 4d^95s^25p\ ^1P_1$ à 27,6 eV, l'amélioration harmonique est la plus élevée parmi les autres harmoniques, comme le montrent la Figure F-16 et la Figure F-17 (b) montrant un 39H intense à 1750 nm de longueur d'onde laser. Cela pourrait être dû à l'énergie de photoionisation plus faible requise pour la photoionisation de l'AIS initial $4d^95s^25p^2\ ^2D_{5/2}$ de Sn II dans l'état $4d^95s^25p\ ^1P_1$ (15,9 eV) par rapport à la photoionisation dans l'état $4d^95s5p^2$ (24,1 eV), comme le montre la Figure F-18.

8.9 Références

1. T. Brabec and F. Krausz, "Intense few-cycle laser fields: Frontiers of nonlinear optics," *Reviews of Modern Physics* **72**, 545–591 (2000).
2. H. Ibrahim, B. Wales, S. Beaulieu, B. E. Schmidt, N. Thiré, E. P. Fowe, É. Bisson, C. T. Hebeisen, V. Waner, M. Giguère, J.-C. Kieffer, M. Spanner, A. D. Bandrauk, J. Sanderson, M. S. Schuurman, and F. Légaré,

- "Tabletop imaging of structural evolutions in chemical reactions demonstrated for the acetylene cation," *Nature Communications* **5**, 4422 (2014).
3. H. C. Kapteyn, L. B. Da Silva, and R. W. Falcone, "Short-wavelength lasers," *Proceedings of the IEEE* **80**, 342–347 (1992).
 4. C. Winterfeldt, C. Spielmann, and G. Gerber, "Colloquium : Optimal control of high-harmonic generation," *Reviews of Modern Physics* **80**, 117–140 (2008).
 5. M. Schnürer, Z. Cheng, M. Hentschel, G. Tempea, P. Kálmán, T. Brabec, and F. Krausz, "Absorption-Limited Generation of Coherent Ultrashort Soft-X-Ray Pulses," *Physical Review Letters* **83**, 722–725 (1999).
 6. R. A. Ganeev, "High-order harmonic generation in a laser plasma: a review of recent achievements," *Journal of Physics B* **40**, R213 (2007).
 7. M. Suzuki, M. Baba, R. Ganeev, H. Kuroda, and T. Ozaki, "Anomalous enhancement of a single high-order harmonic by using a laser-ablation tin plume at 47 nm," *Optics Letters* **31**, 3306 (2006).
 8. G. Duffy, P. van Kampen, and P. Dunne, "4d→5p transitions in the extreme ultraviolet photoabsorption spectra of Sn II and Sn III," *Journal of Physics B* **34**, 3171–3178 (2001).
 9. G. Duffy and P. Dunne, "The photoabsorption spectrum of an indium laser produced plasma," *Journal of Physics B* **34**, L173–L178 (2001).
 10. R. A. Ganeev, M. Suzuki, M. Baba, H. Kuroda, and T. Ozaki, "Strong resonance enhancement of a single harmonic generated in the extreme ultraviolet range," *Optics Letters* **31**, 1699 (2006).
 11. R. A. Ganeev, M. Suzuki, M. Baba, H. Kuroda, and T. Ozaki, "Strong resonance enhancement of a single harmonic generated in the extreme ultraviolet range," *Optics Letters* **31**, 1699 (2006).
 12. V. Strelkov, "Role of autoionizing state in resonant high-order harmonic generation and attosecond pulse production," *Physical Review Letters* **104**, (2010).
 13. B. Peart, I. C. Lyon, and K. Dolder, "Measurements of absolute photoionisation cross sections of Ga⁺ and Zn⁺ ions," *Journal of Physics B* **20**, 5403–5410 (1987).
 14. M. A. Fareed, V. V. Strelkov, M. Singh, N. Thiré, S. Mondal, B. E. Schmidt, F. Légaré, and T. Ozaki, "Harmonic Generation from Neutral Manganese Atoms in the Vicinity of the Giant Autoionization Resonance," *Physical Review Letters* **121**, 023201 (2018).
 15. R. A. Ganeev, M. Suzuki, M. Baba, H. Kuroda, and T. Ozaki, "Strong resonance enhancement of a single harmonic generated in the extreme ultraviolet range," *Optics Letters* **31**, 1699 (2006).
 16. L. B. E. Bom, Y. Pertot, V. R. Bhardwaj, and T. Ozaki, "Multi-μJ coherent extreme ultraviolet source generated from carbon using the plasma harmonic method," *Optics Express* **19**, 3077 (2011).
 17. J. M. Ngoko Djokap and A. F. Starace, "Resonant enhancement of the harmonic-generation spectrum of beryllium," *Physical Review A* **88**, 053412 (2013).
 18. J. M. Ngoko Djokap and A. F. Starace, "Origin of the multiphoton-regime harmonic-generation plateau structure," *Physical Review A* **102**, 013103 (2020).
 19. A. I. Magunov and V. V. Strelkov, "Intensity of Resonant Harmonic Generated in the Multiphoton Ionization Regime," *Physics of Wave Phenomena* **28**, 369–374 (2020).
 20. V. Strelkov, "Role of autoionizing state in resonant high-order harmonic generation and attosecond pulse production.,," *Physical review letters* **104**, 123901 (2010).
 21. V. V. Strelkov, M. A. Khokhlova, and N. Y. Shubin, "High-order harmonic generation and Fano resonances," *Physical Review A* **89**, (2014).
 22. M. Suzuki, M. Baba, R. Ganeev, H. Kuroda, and T. Ozaki, "Anomalous enhancement of a single high-order harmonic by using a laser-ablation tin plume at 47 nm," *Optics Letters* **31**, 3306 (2006).
 23. M. Martins, K. Godehusen, T. Richter, P. Wernet, and P. Zimmermann, "Open shells and multi-electron interactions: core level photoionization of the 3d metal atoms," *Journal of Physics B* **39**, R79–R125 (2006).
 24. R. A. Ganeev, L. B. E. Bom, J.-C. Kieffer, M. Suzuki, H. Kuroda, and T. Ozaki, "Demonstration of the 101st harmonic generated from a laser-produced manganese plasma," *Physical Review A* **76**, 023831 (2007).
 25. M. V. Frolov, N. L. Manakov, and A. F. Starace, "Potential barrier effects in high-order harmonic generation by transition-metal ions," *Physical Review A* **82**, 023424 (2010).
 26. J. Costello, E. Kennedy, B. Sonntag, and C. Clark, "3p photoabsorption of free and bound Cr, Cr⁺, Mn, and Mn⁺," *Physical Review A* **43**, 1441–1450 (1991).
 27. R. A. Ganeev, V. V. Strelkov, C. Hutchison, A. Zaïr, D. Kilbane, M. A. Khokhlova, and J. P. Marangos, "Experimental and theoretical studies of two-color-pump resonance-induced enhancement of odd and even harmonics from a tin plasma," *Physical Review A* **85**, 023832 (2012).

Publications

1. **M. Singh**, M. A. Fareed, V. Strelkov, A. N. Grum-Grzhimailo, A. Magunov, A. Laramée, F. Légaré, and T. Ozaki, "Intense quasi-monochromatic resonant harmonic generation in the multiphoton ionization regime," *Optica* **8**, 1122–1125 (2021).
 - The results published in this article were presented in **Chapter 3** of the thesis.
 - **Contributions:** M.S. along with M.A.F and T.O. designed the experiments. M.S. performed the experiments and analyzed the data. A.L and F.L provided the laser source. M.S., M.A.F., V.S. and T.O. discussed the underlying physics. V.S., A.N.G. and A.M. carried out the simulations. M.S. wrote the manuscript, and all authors contributed to the discussions to improve the manuscript writing.
2. **M Singh** and T Ozaki, "Method and system for generating intense, ultrashort pulses of XUV and soft X ray radiation via HHG" - US Patent App. US20210173283A1, 2021
 - The results published in this article were presented in **Chapter 3** of the thesis.
 - **Contributions:** T.O. proposed to write the patent application. M.S. wrote the patent application and T.O. contributed to the discussions to improve the patent writing.
3. **M. Singh**, M. A. Fareed, A. Laramée, E. Isgandarov, and T. Ozaki, "Intense vortex high-order harmonics generated from laser-ablated plume," *Applied Physics Letters* **115**, 231105 (2019).
 - The results published in this article related to the HHG phenomenon from LAPs were obtained during the doctoral studies in ALLS laboratory, but were not presented in the thesis.
 - **Contributions:** M.S. and T.O. designed the experiments. M.S. performed the experiments with E.I., and M.S. analyzed the data. A.L provided the laser source. M.S. and M.A.F. and T.O. discussed the underlying physics. M.S. wrote the manuscript, and all authors contributed to the discussions to improve the manuscript writing.
4. M. A. Fareed, V. V. Strelkov, **M. Singh**, N. Thiré, S. Mondal, B. E. Schmidt, F. Légaré, and T. Ozaki, "Harmonic Generation from Neutral Manganese Atoms in the Vicinity of the Giant Autoionization Resonance," *Physical Review Letters* **121**, 023201 (2018).
 - The results published in this article were presented in **Chapter 5** of the thesis.
 - **Contributions:** M.A.F. designed the experiments with T.O. Experiments were performed by M.A.F. with S.M. and N.T. Moreover, B.E.S. and F.L. provided the laser source. Further,

V.V.S. carried out the simulations. M.A.F. and M.S. wrote the manuscript, and all authors contributed to the discussions to improve the manuscript writing.

5. **M. Singh**, M.A. Fareed, V. Birulia, A. Magunov, A. N. Grum-Grzhimailo, P. Lassonde, A. Laramée, R. Marcelino, R. Ghahri Shirinabadi, F. Légaré, T. Ozaki and V. Strelkov, “Bright extreme ultraviolet light generation due to double resonance with Rydberg and dark autoionizing states.” In preparation

Target journal: Nature Photonics or Physical Review Letters

- The results to be published in the target journal correspond to **Chapter 4** of the thesis.
- **Contributions:** M.S. along with M.A.F and T.O. designed the experiments. M.S. performed the experiments with M.A.F. Moreover, M.S. and M.A.F analyzed the data. A.L., P.L., and F.L. provided the laser source. V.B., A.M., A.N.G. and V.S. carried out the simulations. M.S. and M.A.F. and T.O. discussed the underlying physics. M.S. wrote the manuscript, and all authors contributed to the discussions to improve the manuscript writing.

6. **M. Singh**, M.A. Fareed, V. Strelkov, A. Mohamed, E. Isgandarov, A. Laramée, F. Légaré and T. Ozaki, “Resonant high-order harmonic generation from Sn III states.” In preparation

Target journal: Optics Letters

- The results to be published in the target journal correspond to **Chapter 6** of the thesis.
- **Contributions:** M.S. and T.O. designed the experiments. M.S. performed the experiments with M.A.F., A.M. and E.I. Moreover, M.S. analyzed the data. A.L. and F.L. provided the laser source. V.S. carried out the simulations. M.S. and M.A.F. and T.O. discussed the underlying physics. M.S. wrote the manuscript, and all authors contributed to the discussions to improve the manuscript writing.